DROUGHT MONITORING IN A DATA-SPARSE REGION BASED ON IN-SITU AND SATELLITE IMAGERY WITHIN GOOGLE EARTH ENGINE: A CASE STUDY OF AWASH RIVER BASIN, ETHIOPIA

FIREAB TENAYE ABO

A THESIS SUBMITTED TO THE DEPARTMENT OF WATER RESOURCES ENGINEERING, SCHOOL OF CIVIL ENGINEERING AND ARCHITECTURE

PRESENTED IN PARTIAL FULFILLMENT OF THE REQUIREMENT FOR THE DEGREE OF MASTER’S IN WATER RESOURCES ENGINEERING (SPECIALIZATION IN HYDRAULIC ENGINEERING)

OFFICE OF GRADUATE STUDIES
ADAMA SCIENCE AND TECHNOLOGY UNIVERSITY

NOVEMBER, 2024
ADAMA, ETHIOPIA

DROUGHT MONITORING IN A DATA-SPARSE REGION BASED ON IN-SITU AND SATELLITE IMAGERY WITHIN GOOGLE EARTH ENGINE: A CASE STUDY OF AWASH RIVER BASIN, ETHIOPIA

FIREAB TENAYE ABO

ADVISOR: - DEREJE BIRHANU (Ph.D.)

A THESIS SUBMITTED TO THE DEPARTMENT OF WATER RESOURCES ENGINEERING, SCHOOL OF CIVIL ENGINEERING AND ARCHITECTURE

PRESENTED IN PARTIAL FULFILLMENT OF THE REQUIREMENT FOR THE DEGREE OF MASTER'S IN WATER RESOURCES ENGINEERING (SPECIALIZATION IN HYDRAULIC ENGINEERING)

OFFICE OF GRADUATE STUDIES
ADAMA SCIENCE AND TECHNOLOGY UNIVERSITY

NOVEMBER 2024

ADAMA, ETHIOPIA

DECLARATION

I hereby declare that this Master Thesis entitled "**Drought Monitoring in a Data-Sparse Region Based on In-situ and Satellite Imagery within Google Earth Engine: A Case Study of Awash River Basin, Ethiopia**" is my original work. That is, it has not been submitted for the award of any academic degree, diploma or certificate in any other university. All sources of materials that are used for this thesis have been duly acknowledged through citation.

Fireab Tenaye Abo	______________________	________________
Name of the student	Signature	Date

RECOMMENDATION

I, the advisor(s) of this thesis, hereby certify that I have read the revised version of the thesis entitled "**Drought Monitoring in a Data-Sparse Region Based on In-situ and Satellite Imagery within Google Earth Engine: A Case Study of Awash River Basin, Ethiopia**" prepared under my/our guidance by **Fireab Tenaye Abo** submitted in partial fulfillment of the requirements for the degree of Mater's of Science in Water Resources Engineering (Specialization in Hydraulic Engineering). Therefore, I/we recommend the submission of revised version of the thesis to the department following the applicable procedures.

Dereje Birhanu (Ph.D.)	______________________	________________
Major Advisor	Signature	Date

APPROVAL PAGE

I, the advisor of the thesis entitled "**Drought Monitoring in a Data-Sparse Region Based on In-situ and Satellite Imagery within Google Earth Engine: A Case Study of Awash River Basin, Ethiopia**" and developed by **Fireab Tenaye**, hereby certify that the recommendation and suggestions made by the board of examiners are appropriately incorporated into the final version of the thesis.

Dereje Birhanu (PhD)	__________________	______________
Major Advisor	Signature	Date

We, the undersigned, members of the Board of Examiners of the thesis by **Fireab Tenaye** have read and evaluated the thesis entitled "**Drought Monitoring in a Data-Sparse Region Based on In-situ and Satellite Imagery within Google Earth Engine: A Case Study of Awash River Basin, Ethiopia**" and examined the candidate during open defense. This is, therefore, to certify that the thesis is accepted for partial fulfillment of the requirement of the degree of Master of Science in Water Resources Engineering (Specialization in Hydraulic Engineering).

______________	______________	______________
Chairperson	Signature	Date
______________	______________	______________
Internal Examiner	Signature	Date
______________	______________	______________
External Examiner	Signature	Date

Signature Date Final approval and acceptance of the thesis is contingent upon submission of its final copy to the Office of Postgraduate Studies (OPGS) through the Department Graduate Council (DGC) and School Graduate Committee (SGC).

______________	______________	______________
Department Head	Signature	Date
______________	______________	______________
School Dean	Signature	Date
______________	______________	______________
Office of Postgraduate Studies	Signature	Date

ACKNOWLEDGMENTS

To begin, I would like to express my deepest gratitude to the Almighty God, whose kindness and blessings provided me with the strength, determination, and opportunity to pursue my education and achieve this academic milestone. Without His divine guidance, none of this would have been possible.

Moreover, I am profoundly thankful to my advisor, Dereje Birhanu (Ph.D.), for his unwavering support, patience, and invaluable guidance throughout my academic journey. His extensive knowledge and constant encouragement played a crucial role in helping me complete my research and successfully write this thesis.

In addition, I wish to extend my heartfelt thanks to my research companions and friends for their teamwork, insightful discussions, and unwavering friendship during our collaborative efforts. Furthermore, my gratitude goes to the Ethiopian Meteorological Institute (EMI) for providing the essential data necessary for my research, which significantly contributed to the outcomes of this study.

I am also especially grateful to the Water Resources Engineering Department for their consistent support and encouragement. In particular, I would like to acknowledge Mr. Million Teshome for his thoughtful feedback and thought-provoking questions, which greatly enriched my work and improved its quality.

Similarly, I am thankful to Adama Science and Technology University (ASTU) for supporting my education through financial and technical assistance, which were vital in enabling me to achieve my goals. Their support laid a strong foundation for the success of this journey.

Finally, I express my deepest appreciation to my beloved family for their unconditional love, encouragement, and faith in my abilities. In particular, I am eternally grateful to my father, Tenaye Abo; my mother, Adanech Saworo; my brother, Dereje Tenaye and my uncle Tamirat Bilate, whose sacrifices, unwavering support, and endless motivation gave me the strength and determination to persevere and complete this thesis.

This work would not have been possible without the combined contributions of all the individuals and institutions mentioned above. For their invaluable roles in my success, I am forever grateful.

TABLE OF CONTENTS

DECLARATION .... **ii**

RECOMMENDATION .... **iii**

APPROVAL PAGE .... **iv**

ACKNOWLEDGMENTS .... **v**

TABLE OF CONTENTS .... **vi**

LIST OF TABLES .... **ix**

LIST OF FIGURES .... **x**

LIST OF ABBREVIATION AND ACRONYMS .... **xii**

ABSTRACT .... **xiv**

1. INTRODUCTION **1**

1.1. Background of the Study 1
1.2. Problem Statement 3
1.3. General Objective: 4
1.3.1. Specific Objectives: 4
1.4. Research Questions 4
1.5. Significance of the Study 4
1.6. Scope and Limitation of the Study 5
1.7. Organization of the Thesis 6

2. LITERATURE REVIEW **7**

2.1. Drought Monitoring Overview 7
2.1.1. General Concepts of Drought 7
2.1.2. Types of Droughts 7
2.1.3. Causes of Drought 8
2.1.4. Impacts of Drought in Ethiopia 9
2.2. Drought Monitoring Approaches 10
2.2.1. In-situ Based Approach of Drought Monitoring 10
2.2.2. Remote Sensing Based Approach of Drought Monitoring 13
2.3. Drought Monitoring Studies in Ethiopia 15
2.4. Google Earth Engine for Environmental Monitoring 16

2.4.1. Explanation and Development of GEE 16
2.4.2. Key Features and Capabilities 18
2.4.2.1. Computational Resources 18
2.4.2.2. High-Speed Computation 18
2.4.2.3. Application Programming Interfaces (APIs) 18
2.4.2.4. Innovative Applications and Future Directions 19
2.4.3. Application of Google Earth Engine Cloud Computing Platform 19
2.5. Google Earth Engine for Environmental Monitoring 20
2.5.1. Satellite Data and Imagery for Drought Monitoring 22
2.5.2. Vegetation Indices 23
2.5.2.1. Selecting Appropriate Drought Monitoring Indices 24
2.6. Integration of In-Situ and Remote Sensing Data for Enhanced Drought Monitoring 25
3. MATERIALS AND METHODS 26
3.1. Description of the Study Area 26
3.1.1. Rainfall 26
3.2. Data and Tools Used 28
3.2.1. The Google Earth Engine Platform 28
3.2.2. Satellite Data 28
3.2.3. Meteorological Data 29
3.3. Drought Monitoring Based on Google Earth Engine Platform 30
3.3.1. Importing and Filter MODIS Satellite Images 30
3.3.2. Add a Day Number (dn) Property to Images 32
3.3.3. Wrapper Day Number Property to Images 33
3.3.4. Validate Lists for Aggregation Operations 34
3.3.5. Image Collection Aggregation 35
3.3.6. Applying Day Number (dn) Property to the LST Images 38
3.3.7. Scaling NDVI and LST Values 38
3.3.8. Calculating Vegetation Condition Index (VCI) 39
3.3.9. Calculating Temperature Condition Index (TCI) 41
3.3.10. Calculating the Vegetation Health Index (VHI) 42
3.3.11. Calculating Area under Different Drought Categories 45
3.3.12. Generating Time Series Charts 48
3.4. Drought Monitoring Based on In-Situ Data 50
3.4.1. Data Quality Analysis 50

3.4.2. Standardized Precipitation Index (SPI) 54
3.5. Methodology Flow Chart 57
3.6. Integration of In-Situ and Remote Sensing Data for Enhanced Drought Monitoring 58
4. RESULT AND DISCUSSIONS 59
4.1. Drought Analysis Using Vegetation Condition Index (VCI) 59
4.1.1. Drought areas across various severity levels of VCI 62
4.1.2. Trend of Mean Annual VCI from 2000 to 2021 63
4.1.3. Drought Frequency Using VCI 64
4.2. Drought Analysis Using Temperature Condition Index (TCI) 65
4.2.1. Drought areas across various severity levels of TCI 68
4.2.2. Trend of Mean Annual TCI from 2000 to 2021 69
4.2.3. Frequency of Drought Based on TCI 70
4.3. Drought Analysis Using Vegetation Health Index (VHI) 71
4.3.1. Drought areas across various severity levels of VHI 73
4.3.2. Trend of Mean Annual VHI from 2000 to 2021 74
4.3.3. Frequency of Drought Based on VHI 75
4.4. In-situ Based Drought Monitoring 76
4.4.1. Drought Analysis Using the Standardized Precipitation Index (SPI) 76
4.5. Pearson Correlation Test 79
4.5.1. Correlation Matrix of VCI, TCI, and VHI 79
4.5.2. Correlation Analysis Between the VCI, TCI, and VHI With SPI3 80
4.6. Discussion 83
5. CONCLUSION AND RECOMMENDATIONS 86
5.1. Conclusion 86
5.2. Recommendations 87
REFERENCES 89
APPENDICES 104

LIST OF TABLES

Table 2-1 Most commonly used in-situ-based drought monitoring indices. 12

Table 2-2 Most commonly used remote sensing-based drought monitoring indices 14

Table 3-1 Selected satellite products used for the study 29

Table 3-2 Classification of drought severity based on SPI3 values 55

LIST OF FIGURES

Figure 2-1 Relationship between meteorological, agricultural, hydrological, and socio-economic drought ... 8
Figure 2-2 Applications of Google earth engine ... 20
Figure 3-1 Location map of the study area ... 27
Figure 3-2 Code used to import MODIS satellite images and study area map ... 32
Figure 3-3 Code used to add a day number (*dn*) property to images ... 33
Figure 3-4 Code used wrapper day number property to images ... 33
Figure 3-5 Code used to validate lists for aggregation operations ... 35
Figure 3-6 Code used to aggregate image collection ... 38
Figure 3-7 Code used to apply dn property to the LST images ... 38
Figure 3-8 Code used to scale NDVI and LST values ... 39
Figure 3-9 Code used to calculate vegetation condition index ... 41
Figure 3-10 Code used to calculate temperature condition index ... 42
Figure 3-11 Code used to calculate vegetation health index ... 44
Figure 3-12 Code used to calculate area under different drought categories ... 48
Figure 3-13 Code used to generate time series charts ... 49
Figure 3-14 Code used to fill missed rainfall data ... 51
Figure 3-15 Data consistency analysis using double mass curve for Awash River Basin .. 52
Figure 3-16 Homogeneity test using rainbow software for Adama station ... 53
Figure 3-17 Code used to calculate SPI3 in R Studio ... 57
Figure 3-18 Methodology flow chart ... 57
Figure 4-1 Spatio-temporal patterns of mean VCI of the main growing seasons over the study area from 2000 to 2010. ... 60
Figure 4-2 Spatio-temporal patterns of mean VCI of the main growing seasons over the study area from 2011 to 2021. ... 61
Figure 4-3 Drought areas across various severity levels of VCI from 2000 to 2021 ... 62
Figure 4-4 Trend of mean annual VCI in the study area from 2000 to 2021. ... 64
Figure 4-5 Frequency of drought based on VCI ... 65
Figure 4-6 Spatio-temporal patterns of mean TCI of the main growing seasons over the study area from 2000 to 2010. ... 66
Figure 4-7 Spatio-temporal patterns of mean TCI of the main growing seasons over the study area from 2011 to 2021. ... 67

Figure 4-8 Drought areas across various severity levels of TCI from 2000 to 2021 68
Figure 4-9 Trend of mean annual TCI from 2000 to 2021 69
Figure 4-10 Frequency of drought based on TCI 70
Figure 4-11 Spatio-temporal patterns of mean VHI of the main growing seasons over the study area from 2000 to 2010 71
Figure 4-12 Spatio-temporal patterns of mean VHI of the main growing seasons over the study area from 2011 to 2021 72
Figure 4-13 Drought areas across various severity levels of VHI from 2000 to 2021........ 74
Figure 4-14 Trend of Mean Annual VHI from 2000 to 2021.. 75
Figure 4-15 Frequency of drought based on VHI 76
Figure 4-16 SPI-3 Time series for July to September from 2000 to 2021 in the Upper Awash River Basin 77
Figure 4-17 SPI-3 Time series for July to September from 2000 to 2021 in the Middle Awash River Basin 77
Figure 4-18 SPI-3 Time series for July to September from 2000 to 2021 in the Lower Awash River Basin 78
Figure 4-19 Correlation Matrix of VCI, TCI, and VHI... 80
Figure 4-20 Correlation Matrix of VCI with SPI3 81
Figure 4-21 Correlation Matrix of TCI with SPI3.. 81
Figure 4-22 Correlation Matrix of VHI with SPI3 82

LIST OF ABBREVIATION AND ACRONYMS

AA	Addis Ababa
ALOS	Advanced Land Observing Satellite
API	Application Programming Interface
AVHRR	Advanced Very High Resolution Radiometer
AWS	Amazon Web Services
BRT	Buishand Range Test
CHIRPS	Climate Hazards Group InfraRed Precipitation with Station data
CMI	Crop Moisture Index
EMI	Ethiopian Meteorological Institute
ETDI	Evapotranspiration Deficit Index
EVI	Enhanced Vegetation Index
GEE	Google Earth Engine
IDE	Integrated Development Environment
LST	Land Surface Temperature
MICE	Multiple Imputation by Chained Equations
MODIS	Moderate Resolution Imaging Spectroradiometer
MSI	Moisture Stress Index
NASA	National Aeronautics and Space Administration
NDVI	Normalized Difference Vegetation Index
NDWI	Normalized Difference Water Index
NOAA	National Oceanic and Atmospheric Administration
PCI	Precipitation Condition Index
PMM	Predictive Mean Matching
PSDI	Palmer Drought Severity Index
QA	Quality Assessment
RDI	Reconnaissance Drought Index
ROI	Region of Interest
SDG	Sustainable Development Goals
SNHT	Standard Normal Homogeneity Test

SMDI	Soil Moisture Deficit Index
SPI	Standardized Precipitation Index
SPI3	3-month Standardized Precipitation Index
SPEI	Standardized Precipitation Evapotranspiration Index
TCI	Temperature Condition Index
TIFF	Tagged Image File Format
TRMM	Tropical Rainfall Measuring Mission
TVX	Temperature-Vegetation Index
VCI	Vegetation Condition Index
VHI	Vegetation Health Index

ABSTRACT

Drought is a significant climatic event that adversely affects agricultural productivity, water resources, and livelihoods, particularly in regions such as the Awash River Basin in Ethiopia. This study aims to monitor drought conditions from 2000 to 2021 by integrating remote sensing data and in-situ observations using the Google Earth Engine (GEE) platform. The study utilized the Vegetation Condition Index (VCI), Temperature Condition Index (TCI), and Vegetation Health Index (VHI) derived from MODIS satellite imagery. These indices were categorized into drought severity levels (No Drought, Mild, Moderate, Severe, and Extreme) and were used to monitor the spatial and temporal patterns of drought. SPI3 data were derived from rainfall records at 23 meteorological stations in the basin, and Pearson correlation analysis was conducted to assess the relationship between SPI3 and satellite-derived indices. The results show that mild and moderate drought conditions were predominant in the Awash River Basin over a 22-year period. The VCI results indicated that mild drought affected over 50% of the area in many years, with notable peaks in 2001, 2010, 2011, and 2021, where mild drought extended over 70% of the basin. Moderate drought conditions were prevalent in 2008, 2009, and 2016, affecting up to 50% of the basin area. Severe and extreme droughts, although less frequent, occurred in specific years such as 2009, 2015, and 2017, particularly in the middle and lower parts of the basin. The TCI results revealed that temperature-related drought stress was significant in 2009 and 2017, with severe and extreme droughts affecting the northern and central regions. The VHI, which combines the VCI and TCI, showed that moderate droughts were most common across the study period, especially in 2009 and 2017. The highest VHI values, which indicate healthier vegetation conditions, were observed in 2020 and 2021.Pearson correlation analysis between SPI3 and the satellite-based indices showed strong positive correlations. The VCI and SPI3 exhibited moderate to strong correlations across most stations, with the highest correlation in Asebe Teferi (0.57). TCI correlation with SPI3 ranged from -0.26 to 0.53, while VHI demonstrated strong correlations, particularly in Asebe Teferi (0.63), validating the use of vegetation-based indices for drought monitoring. This study underscores the broader significance of effective drought monitoring in the Awash River Basin because droughts in this region have profound impacts on local agriculture, water availability, and livelihoods. The ability to monitor and assess drought conditions supports more resilient agricultural practices and informs water resource management strategies that are crucial for sustaining the region's economy and food security. The findings of this study have practical applications such as enhancing early warning systems and guiding resource allocation for drought mitigation efforts. By leveraging GEE's capabilities of GEE, policymakers and stakeholders can better plan and implement timely interventions, reduce the adverse effects of drought, and support sustainable development initiatives. Therefore, the results demonstrate the effectiveness of utilizing GEE as a powerful tool for monitoring and analyzing drought.

Keywords: Drought Assessment, Drought Indices, Remote Sensing; Google Earth Engine, Awash River Basin

1. INTRODUCTION

1.1. Background of the Study

Drought is a significant climatic phenomenon characterized by an extended period of deficient precipitation that affects large areas and lasts for months or even years(Nagarajan, 2010). This prolonged dry period leads to various detrimental effects, including soil degradation, water scarcity, desertification, vegetation destruction, sandstorms, and wildfires, which significantly affect both the environment and human livelihoods (F. Wang et al., 2020).

In Ethiopia, most drought-monitoring methods traditionally rely on situ-based indices. These indices combine data from various indicators, such as temperature, precipitation, streamflow, groundwater, and evapotranspiration, to define key drought characteristics, including the spatial extent, duration, and severity (Abera Tareke & Gebeyehu Awoke, 2022; Gebreyesus et al., 2020). In situ-based indices can provide accurate drought predictions near meteorological stations. However, their effectiveness is limited in areas with sparse station coverage or high spatial variability, making it challenging to comprehensively monitor and characterize drought conditions (K. Hazaymeh & Hassan, 2016; Sun et al., 2020).

Remote sensing has emerged as a valuable tool for drought monitoring to address these limitations. Remote sensing technologies provide continuous and comprehensive datasets including precipitation, temperature, soil moisture, potential evapotranspiration, actual evapotranspiration, and vegetation growth. These datasets allow for the analysis of drought spatiality over extended periods and over large areas. However, massive volumes of data collected by remote sensing systems pose significant challenges for management and analysis using conventional software and desktop computing resources(Amani et al., 2020).

To address these challenges, Google developed GEE, a cloud-based platform designed for geospatial analysis. GEE offers high-performance computing resources and easy access to multitemporal satellite data, enabling users to process and analyze large datasets online. The platform provides a programming interface (API) that is accessible over the Internet, allowing users to acquire and manipulate data using JavaScript and Python. This capability has greatly facilitated the processing of information, enabling the production of trend maps and characterization of Earth's surface resources without the need for high-processing-power computers(Gorelick et al., 2017).

GEE's ability to analyze and classify satellite data at high speeds allows for the generation of more relevant and accurate outputs. Numerous studies have demonstrated the effectiveness of remote sensing in various aspects of drought monitoring. For example, Abera Tareke and Gebeyehu Awoke (2022) explored the use of remote sensing data for drought monitoring, while (Edossa et al., 2010) and Gebreyesus et al. (2020) investigated different drought indices and their applications. Despite these advancements, there is a notable gap in basin-level drought monitoring, particularly when utilizing GEE and comparing remote sensing-based assessments with in situ-based methods.

This study aims to fill this gap by leveraging the GEE platform to acquire and analyze MODIS satellite images for drought monitoring in the Awash River Basin. The results obtained from the GEE were compared with those derived from in situ drought assessments, providing a comprehensive evaluation of drought conditions in the basin. By integrating remote sensing data with in-situ observations, this research seeks to enhance the understanding of drought dynamics and improve monitoring in the Awash River Basin.

The integration of remote sensing and in-situ data for drought monitoring offers several additional advantages. Remote sensing provides broad spatial coverage, which is not feasible using ground-based observations alone. This allows for the detection of drought conditions in remote and inaccessible areas, thereby ensuring a more comprehensive monitoring. Furthermore, remote sensing data can be updated frequently, providing near real-time monitoring capabilities that are crucial for timely decision making and response (Ettehadi Osgouei et al., 2019).

In addition, the use of remote sensing in drought monitoring can enhance the development of drought indices that are more sensitive to local conditions. For instance, the Normalized Difference Vegetation Index (NDVI) derived from satellite imagery has been widely used to assess vegetation health and to detect drought conditions. Combining such indices with in-situ data can improve the accuracy and reliability of drought monitoring (West et al., 2019).

Moreover, the application of advanced data analysis techniques such as machine learning and data fusion can further enhance the capabilities of drought monitoring systems. Machine learning algorithms can be used to identify complex patterns and relationships in large datasets, thereby improving the prediction and characterization of drought events. Data fusion techniques can integrate multiple sources of information, providing a more comprehensive view of drought conditions(Mokhtari & Akhoondzadeh, 2021).

This study's focus on the Awash River Basin aims to address the critical need for improved drought monitoring in Ethiopia. By leveraging the capabilities of GEE and integrating remote sensing with in-situ data, this study provides valuable insights into the spatiotemporal dynamics of drought in the region. This approach not only enhances the understanding of drought impacts but also supports the development of more effective drought management strategies, ultimately contributing to the resilience and sustainability of affected communities.

1.2. Problem Statement

Over the past 10–15 years, the frequency of drought has increased across all regions of Ethiopia, resulting in severe consequences. Approximately one-third of the population has faced famine, and 90% of livestock has perished due to drought (Liou & Mulualem, 2019; Mera, 2018; Teshome & Zhang, 2019). In particular, the Awash Basin is highly vulnerable to frequent droughts, falling food scarcity and impacting both human and livestock populations. In addition to these immediate effects, drought threatens regional water resources, socioeconomic stability, and ecosystem diversity. In terms of public health, drought-induced reductions in water quality have escalated the prevalence of waterborne diseases, such as cholera and diarrhea, especially in vulnerable communities (P. Wang et al., 2022). Accurate and timely drought monitoring is crucial to guide mitigation efforts and improve community resilience.

While in-situ drought indices are valuable near meteorological stations, their limited spatial coverage presents a challenge for comprehensive monitoring. By contrast, satellite-based indices offer spatially continuous, rapid, and cost-effective monitoring across vast areas (K. Hazaymeh & Hassan, 2016). However, managing extensive datasets from remote sensing requires advanced data handling tools. The GEE provides a unique advantage for such studies, as it simplifies the handling, analysis, and visualization of large-scale data. However, a significant challenge lies in adapting GEE outputs to local conditions because the suitability of various indices may differ based on region-specific factors (Huang et al., 2020). This study addresses this gap by integrating satellite data with in-situ observations to provide a more holistic perspective on drought impacts. The combination of GEE's capabilities with in-situ data can improve the accuracy and relevance of drought assessments, supporting more effective mitigation and adaptation strategies (Qiu et al., 2023). Specifically, this study seeks to validate the integration of GEE and in-situ data with the aim of enhancing the accuracy of drought monitoring in the Awash Basin. By employing both agricultural and meteorological drought indices, this study aligns with the goal of advancing real-time drought monitoring and supporting sustainable water management in drought-prone regions.

1.3. General Objective:

The general objective of this study was to monitor drought in the Awash River Basin over the past decades using in-situ satellite imagery from the Google Earth Engine platform.

1.3.1. Specific Objectives:

- To analyze the spatiotemporal drought in the basin using remote sensed and in-situ (meteorological) data
- To characterize drought events in the basin in terms of frequency, severity, and spatial extent
- To assess the accuracy and effectiveness of specific remote sensing-based drought indices (VCI, TCI and VHI) for drought monitoring by comparing them with in-situ data

1.4. Research Questions

Therefore, this study examined the following three questions:

- How can spatiotemporal drought patterns in the Awash River Basin be analyzed using remote sensing and in-situ data?
- How do drought events in the basin vary in terms of frequency, severity, and spatial extent during the study period?
- How accurate and effective are remote sensing-based drought indices (VCI, TCI, and VHI) for drought monitoring when compared with in-situ data in the basin?

1.5. Significance of the Study

Drought monitoring is a critical task, particularly in data-sparse regions where traditional methods often fall short. The Awash River Basin in Ethiopia exemplifies this region, where limited data availability poses significant challenges for effective drought monitoring and management. This study employed GEE to integrate in-situ and satellite imagery for comprehensive drought monitoring, offering several significant contributions. This innovative approach enhances the accuracy and spatial resolution of drought monitoring in the Awash River Basin, providing a reliable method for identifying and analyzing drought conditions across extensive areas.

Moreover, by validating the effectiveness of GEE in drought monitoring, this study promotes the adoption of advanced cloud-computing platforms for environmental monitoring. By demonstrating how GEE can achieve high-precision surface detection and mapping, this research underscores the potential of modern technology to facilitate timely and effective drought response. Furthermore, the development of accessible codes for drought monitoring, made available on GitHub, ensures that a diverse range of users, including engineers, scientists, policymakers, NGOs, field workers, and the general public, can utilize these tools with minimal effort, expense, and time. This accessibility encourages replication of the study in other regions, fostering broader applications and inspiring further research.

Additionally, the implications of this study extend to policy and decision making, offering valuable insights for water resource management and agricultural planning in drought-prone areas. By providing a robust method for drought monitoring, this research supports informed decision-making that can mitigate the adverse impacts of drought on communities and ecosystems.

In general, this study holds significant potential for advancing drought monitoring practices, especially in developing countries with limited resources. The use of cutting-edge technology, such as GEE, can inspire other researchers to explore and utilize this platform in their own work, leading to further advancements in remote sensing and environmental management. Ultimately, this study enhances our understanding of drought dynamics and improves the capacity for effective drought mitigation and management.

1.6. Scope and Limitation of the Study

The scope of this study was to utilize remote sensing techniques through the GEE to assess drought in the Awash River Basin from 2000 to 2021. This study employs the VCI, TCI, and VHI to analyze the spatial and temporal variability of drought across the region. Additionally, this study aims to examine the correlation between these indices and SPI3 to provide a comprehensive understanding of drought severity. The outcomes of this research will contribute to improved drought monitoring practices, helping policymakers, farmers, and water resource managers in the Awash River Basin to better understand and mitigate the impacts of drought.

The effectiveness of GEE in this study was demonstrated by its ability to process large datasets and analyze drought conditions at multiple locations across the basin. This will provide valuable insights into the drought dynamics of different parts of the Awash River Basin, particularly in areas with limited ground-based observations.

However, the study was limited by the quality and availability of satellite imagery used in the analysis. The accuracy of the results depends on the resolution and reliability of the remote sensing data, which may not fully capture localized drought conditions or vegetation stress in complex terrains. Additionally, while this study focused on the Awash River Basin, the findings may not be fully generalizable to other regions with different climatic or geographic conditions. This study excludes hydrological drought due to the limited availability of ground-based streamflow data across the Awash River Basin. Monitoring hydrological drought effectively requires comprehensive streamflow measurements, which are sparse in many parts of the basin. Consequently, this study focuses on meteorological and agricultural drought.

1.7. Organization of the Thesis

This thesis is organized into five chapters. Chapter One introduces the study's background, problem statement, general and specific objectives, research questions, significance, and scope. Chapter Two reviews the literature on drought monitoring: a concept overview, causes, monitoring methods, and how the GEE was applied as a remote operation tool. It describes the materials and methods used in the study, including the study area, data, tools, and methodology flowcharts. The results are presented in Chapter Four, including drought using various indices and drought-affected areas across different severity levels and trends. We also discuss the findings of this study. Chapter Five finally concludes the study.

2. LITERATURE REVIEW

2.1. Drought Monitoring Overview

2.1.1. General Concepts of Drought

Drought is a prolonged period of dryness within the natural climate cycle that can occur globally. It is characterized by a gradual onset, often resulting from insufficient rainfall. This costly natural hazard has significant and widespread impacts, affecting various economic sectors such as agriculture, water resources, tourism, energy, and ecosystems. Historical records highlight its recurrent nature, impacting larger areas compared to other hazards such as floods, which are typically confined to specific regions. The far-reaching impacts of droughts have been observed across diverse geographical scales and climate conditions worldwide (Dai, 2011).

2.1.2. Types of Droughts

Droughts can be categorized into four primary types, each corresponding to a distinct set of drought indicators: meteorological, hydrological, agricultural, and socioeconomic.

Meteorological drought is typically characterized by the extent of dryness compared to normal conditions and the length of the dry spell. It's important to note that definitions of meteorological drought are region-specific due to the varying atmospheric conditions that lead to precipitation deficits across different areas (Sivakumar et al., 2011).

Hydrological drought is marked by consistently low water levels in streams and reservoirs over extended periods, often lasting months or years. These droughts are frequently linked to meteorological droughts and share similar recurrence patterns. Land use changes and degradation can influence the severity and frequency of hydrological droughts (Van Loon, 2015).

Agricultural drought occurs when soil moisture becomes insufficient for plant requirements. This type of drought connects various aspects of meteorological or hydrological drought to agricultural impacts. It focuses on factors such as lack of rainfall, disparities between actual and potential evapotranspiration, soil water shortages, and decreased groundwater or reservoir levels (X. Liu et al., 2016).

Socioeconomic drought definitions link the supply and demand of certain economic goods to elements of meteorological, hydrological, and agricultural drought. This type differs from the others as its occurrence depends on the temporal and spatial processes of supply and demand to identify or classify droughts. Socioeconomic drought emerges when demand for an economic good surpasses supply due to weather-related water shortages (Wilhite, 2000).

Drought manifests in various forms, including meteorological, hydrological, agricultural, and socioeconomic factors, each affecting different sectors over time. Figure 2.1 illustrates the sequence and interconnected impact of these drought types.

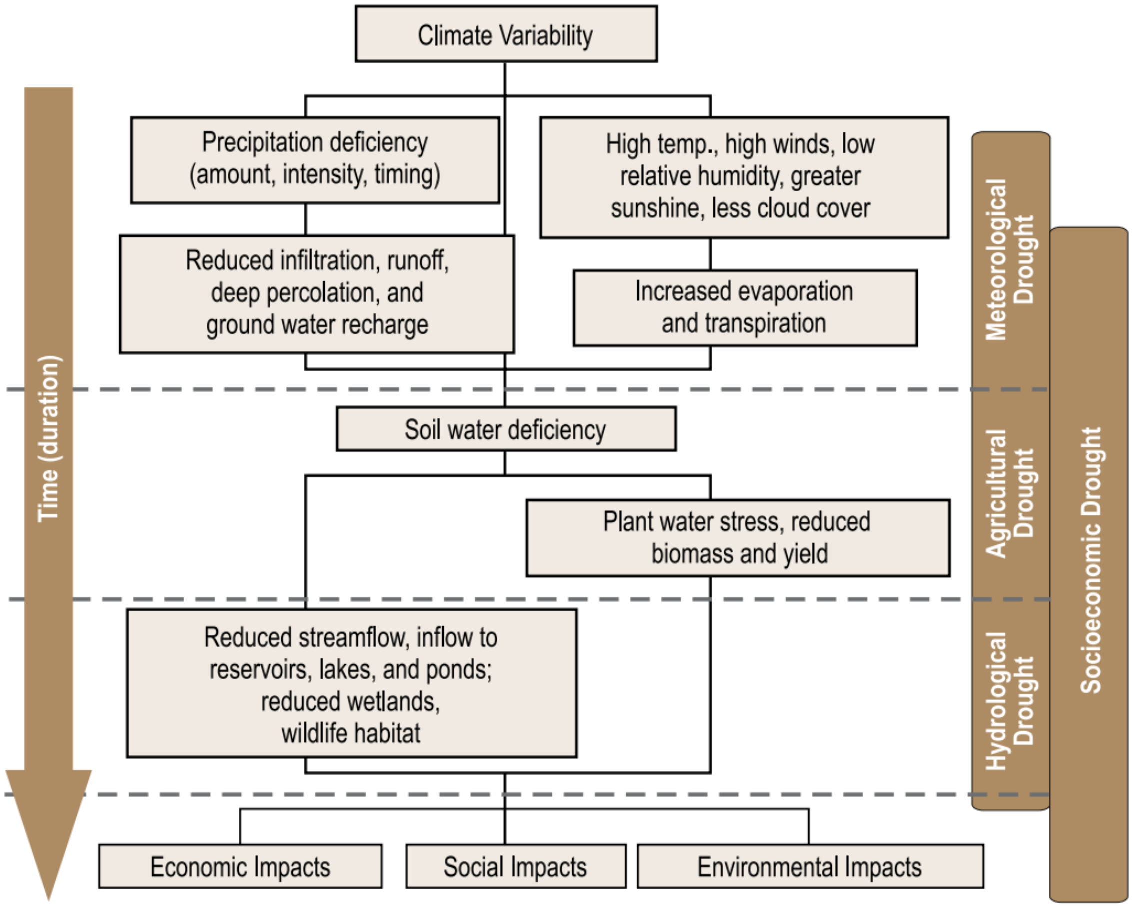

Figure 2-1 Relationship between meteorological, agricultural, hydrological, and socio-economic drought

(Source: https://drought.unl.edu/Education/DroughtIn-depth/TypesofDrought.aspx accessed on November 15, 2023)

2.1.3. Causes of Drought

Drought is primarily caused by lower precipitation and higher evaporation rates; however, its severity and occurrence are influenced by a variety of natural and anthropogenic factors. The interplay of hydroclimatic parameters, as demonstrated in the Cesar River Basin in

Colombia, shows that precipitation shortfalls and high potential evapotranspiration are significant contributors to drought conditions in different regions of the basin (Paez-Trujilo et al., 2023). In Eastern China, the extreme drought of 2019 was driven by central Pacific El Niño events and warm sea surface temperature anomalies over the Kuroshio extension region, which induced cyclonic circulation anomalies and resulted in deficient moisture and anomalous descent over the area (Lyu et al., 2023). Natural climate variability, such as El Niño and La Niña, further contributes to drought by influencing atmospheric circulation patterns and causing variations in precipitation and temperature (Pachauri et al., 2014). The impacts of climate change have exacerbated the frequency, severity, and spatial extent of droughts, as well as anthropogenic activities such as deforestation, overgrazing, soil degradation, and water mismanagement, creating a vicious cycle of ecological degradation (Li et al., 2024). Despite a historical ample rainfall situation in the Democratic Republic of Congo, drought conditions are emerging due to decreased rainfall and are exacerbated by desertification processes (Saidi et al., 2023). Human-induced changes such as deforestation, urbanization, and alterations in land cover contribute to local and regional climate shifts, creating conditions conducive to drought (Dale et al., 2001). Furthermore, the over-extraction of groundwater for various purposes depletes underground water sources, exacerbating drought conditions (Scanlon et al. 2012). Additionally, the Standardized Precipitation Index and Normalized Difference Vegetation Index have been instrumental in assessing droughts, highlighting that substantial rainfall deviation and skewed spatial or temporal distribution significantly affect crop production and water availability (Panda et al., 2020).

2.1.4. Impacts of Drought in Ethiopia

Drought is a recurrent and severe issue in Ethiopia that significantly impacts agriculture, pastoral livelihoods, and socioeconomic stability. Analyzing historical drought patterns from 1981 to 2018, one study highlighted the increasing frequency and intensity of droughts across Ethiopia's major river basins, with notable episodes in 1984, 2009, and 2015, influenced by climatic factors, such as the Indian Ocean Dipole and El Niño (Liou & Mulualem, 2019). In the Borana Zone, extreme droughts from 2000 to 2022, driven by decreasing rainfall and increasing temperatures, have significantly affected vegetation and livestock, highlighting the need for enhanced drought monitoring using Earth observational data(Bojer et al., 2024). The socio-economic impact is profound, particularly in pastoral communities in Eastern Ethiopia, where high vulnerability and low adaptive capacity exacerbate the effects of recurrent droughts, leading to significant losses in livestock and livelihoods (Tofu, 2024). Additionally, in Yabello district, droughts have caused substantial livestock mortality and increased malnutrition, calling for immediate humanitarian aid and policy intervention (Bamedo, 2024). Perceptions of rural households in Northeast Ethiopia align with these findings, recognizing the increasing frequency of droughts and their adverse effects on agriculture and livelihoods, stressing the importance of integrating local knowledge into climate policy (Molla et al., 2024). Moreover, droughts have had a significant impact on food security in Africa, with 57% of the world's drought events recorded in Africa, predominantly affecting the Greater Horn of Africa, which includes Ethiopia due to its climate and reliance on rain-fed agriculture (Alasow et al., 2024; Babaousmail et al., 2024). Over the past 50 years, drought in Ethiopia has shown both spatial and temporal variations, with certain areas experiencing more frequent occurrences, particularly the eastern, southeastern, and rift valley regions, where droughts recurred once in ten years historically (Mera, 2018; Haile, 1988). Effective drought management strategies, such as improving water access, providing early warning systems, and diversifying livelihoods, are crucial to mitigating these impacts and enhancing resilience.

2.2. Drought Monitoring Approaches

Drought monitoring is crucial for the early warning, planning, and mitigation of the impact of drought on communities. However, monitoring drought is complex due to its gradual impact and varying effects across regions. Drought monitoring indicators and indices include measurements of precipitation, temperature, and water supply to assess changes in a region's hydrological cycle. Since the 1960s, different drought indices and methods have been proposed to identify and monitor drought events (Jain et al., 2015). These indices describe meteorological drought based on precipitation series and hydrological or agricultural drought or water shortages in urban water supply systems.

2.2.1. In-situ Based Approach of Drought Monitoring

The in-situ approaches, also known as traditional or conventional approaches, involve monitoring indices for meteorological, hydrological, and agricultural drought. These indices rely on ground-available data collected from climatic, agricultural, and hydrologic stations, drawing on readings of climatic variables such as rainfall, streamflow, groundwater, evapotranspiration, temperature, and relative humidity (Qamer et al., 2019). These indices offer extensive and precise quantitative and qualitative information regarding agricultural drought conditions at specific locations where input data are collected. However, interpolation is essential to extend these indices between weather stations and achieve continuous spatial data coverage, introducing uncertainties (Hazaymeh and Hassan, 2016; Sun et al., 2020). Recent innovations leverage satellite data, providing a permanent data archive, cost-effectiveness, and a consistent view of nearly all of Earth's surfaces (L. Zhang et al., 2017). This shift towards satellite data addresses many limitations associated with in-situ approaches, enhancing spatial coverage and accuracy in drought monitoring. Table 2.1 summarizes some of the most commonly used in-situ based drought monitoring indices.

The in-situ approaches, also known as traditional or conventional approaches, involve monitoring indices for meteorological, hydrological, and agricultural drought. These indices rely on ground-available data collected from climatic, agricultural, and hydrologic stations, drawing on readings of climatic variables such as rainfall, stream flow, groundwater, evapotranspiration, temperature, and relative humidity, as emphasized by (Qamer et al., 2019).

These indices offer extensive and precise quantitative and qualitative information regarding agricultural drought conditions at specific locations where input data are collected. However, interpolation is essential to extend these indices between weather stations and achieve continuous spatial data coverage. Despite its utility, spatial interpolation introduces uncertainties, as highlighted by (Hazaymeh and Hassan, 2016) and (Sun et al., 2020). To address these challenges, recent innovations leverage satellite data, providing a permanent data archive, cost-effectiveness, and a consistent view of nearly all of Earth's surfaces (L. Zhang et al., 2017). This shift towards satellite data addresses many limitations associated with in-situ approaches, enhancing spatial coverage and accuracy in drought monitoring. Table 2.1 summarizes some of the most commonly used in-situ based drought monitoring indices.

Table 2-1 Most commonly used in-situ-based drought monitoring indices.

Index	Inputs Data	Advantage	Disadvantage	Source
Standardized Precipitation Index (SPI)	Precipitation	Easy to use, needs only precipitation data, measures drought over time.	Uses only precipitation, hard to interpolate over large areas.	McKee et al., 1993
Standardize Precipitation Evapotranspiration Index	Temperature and precipitation	Addresses climate change impacts on drought beyond precipitation-based indices like SPI	SPEI matches SPI when there's no temperature change	Vicente-Serrano et al., 2010
Palmer Drought Severity Index (PSDI)	Temperature, precipitation, soil moisture, evapotranspiration	Offers a fuller view of drought	sophisticated computation.	Palmer, 1965
Soil Moisture Deficit Index (SMDI)	Weekly evapotranspiration and soil moisture values	Improves the ability for modeling and monitoring hydrologic system and soil moisture deficient at a finer resolution	Irrespective to soil properties across different climatic conditions	Narasimhan and Srinivasan, 2005
Crop Moisture Index (CMI)	Precipitation and temperature	Easley calculated using temperature and precipitation data	Not suitable for long term assessment of agricultural drought	Palmer, 1968
Crop Specific Drought Index (CSDI)	Temperature, precipitation, evapotranspiration	Estimates daily soil water for various zones and types	Requires extensive data: climate, crop phenology, soil type.	Meyer et al., 1991
Evapotranspiration Deficit Index (ETDI)	Weekly evapotranspiration and soil moisture values	Accounts for water stress, providing weekly values for short-term dryness.	Evapotranspiration and irregular rainfall increase spatial variation in summer.	Narasimhan & Srinivasan, 2005

2.2.2. Remote Sensing Based Approach of Drought Monitoring

Remote sensing has emerged as a critical tool for drought monitoring due to its advanced temporal and spatial capabilities, enabling comprehensive and near-real-time assessments of drought conditions (Lei et al., 2015). This method leverages satellite-based rainfall estimates and vegetation indices, such as the Standardized Precipitation Index (SPI) and the NDVI, to evaluate vegetation health and moisture stress. These indicators are crucial for understanding both the short- and long-term impacts of drought on ecosystems and agricultural areas. The integration of satellite-derived data with hydrological modeling has proven particularly effective in generating robust drought indicators, enhancing drought resilience and early warning systems (Senay et al., 2015). In the realm of remote sensing, techniques such as the thermal inertia and vegetation index methods have been applied to detect large-scale droughts. These methods often incorporate data from Land Surface Temperature (LST) and NDVI, which are instrumental in developing indices like the Vegetation Drought Response Index (VegDRI) (Thenkabail and Rhee, 2017). Kogan's Vegetation Condition Index (VCI), introduced in 1990, utilizes long-term NDVI records to measure vegetation health relative to extreme conditions in prior years. Low VCI values are indicative of vegetation stress, often associated with water deficiency, while high values suggest healthier vegetation, thus providing a reliable measure of drought severity (Gebrehiwot et al., 2011; Liou and Mulualem, 2019).

Another critical advancement in remote sensing-based drought monitoring is the use of Land Surface Temperature data to evaluate evapotranspiration, soil moisture, and vegetation stress. In 1995, Kogan developed the Temperature Condition Index (TCI), which uses thermal data to detect vegetation stress caused by temperature extremes and excessive wetness. TCI is especially effective in highlighting thermal effects on vegetation, as it can detect minor changes in vegetation health that arise due to moisture shortages and high temperatures. TCI surpasses NDVI and VCI in detecting vegetation stress under conditions of high soil moisture, often resulting from prolonged rainfall or persistent cloud cover (Kogan, 1995; Qamer et al., 2019). Some of the most commonly used remote sensing-based drought monitoring indices, along with their specific applications and limitations, are summarized in Table 2-2. These indices support the broader aim of improved drought preparedness and management by facilitating early detection, continuous monitoring, and effective response strategies.

Table 2-2 Most commonly used remote sensing-based drought monitoring indices

Index	**Expression**	**Advantage**	**Disadvantage**	**source**
Normalized Difference Vegetation Index (NDVI)	$\mathrm{NDVI} = \frac{\mathrm{NIR} - \mathrm{R}}{\mathrm{NIR} + \mathrm{R}}$	Measures vegetation health or greenness.	Sensitive to dark, wet soils and shows a lag in soil moisture response	Tucker, 1979
Vegetation Condition Index (VCI)	$\mathrm{VCI} = \left(\frac{\mathrm{NDVI_i} + \mathrm{NDVI}}{\mathrm{NDVI_{max}} - \mathrm{NDV}}\right. * 100$	Indicates vegetation greenness.	Requires long-term data.	Kogan, 1990
Moisture Stress Index (MSI)	$\mathrm{MSI} = \frac{\mathrm{SWIR}}{\mathrm{NIR}}$	More sensitive at the canopy level than the leaf level.	Suitable for densely vegetated areas.	Hunt and Rock, 1989
Temperature condition index (TCI)	$\mathrm{TCI} = \left(\frac{\mathrm{LST_{max}} - \mathrm{LST_i}}{\mathrm{LST_{max}} - \mathrm{LST_{mi}}}\right. * 100$	Input data is easy to obtain	Needs clear skies during imaging.	Kogan, 1995
Precipitation Condition Index (PCI)	$\mathrm{PCI} = (\frac{\mathrm{TRMM} - \mathrm{TRM}}{\mathrm{TRMM_{max}} - \mathrm{TR}}$	Performs well regionally in most weather conditions.	Low spatial resolution and limited imaging at high latitudes.	A. Zhang and Jia, 2013
Vegetation health index (VHI)	$\mathrm{VHI} = 0.5 * \mathrm{VCI} + (1 - 0.5) * \mathrm{TCI}$	Provides more comprehensive drought monitoring capabilities	Requires appropriate data fusion for VCI and TCI	Kogan, 1997
Temperature -vegetation index (TVX)	$\mathrm{TVX} = \frac{\mathrm{LST}}{\mathrm{NDVI}}$	Depicts drought conditions at regional scale	TVX/VSWI slopes may vary from one place to another	Lambin and Ehrlich, 1996

Building upon the advancements in remote sensing methodologies, the role of cloud computing platforms in enhancing the efficiency and scalability of drought monitoring comes into focus. While remote sensing has significantly enriched our ability to capture temporal and spatial characteristics, the integration of powerful cloud-based tools such as the GEE brings a new dimension to the analysis of large-scale environmental datasets. GEE has been effectively used for mapping water distribution, assessing drought risks, and integrating optical and radar imagery to enhance drought monitoring (Conversi et al., 2023; K. M. A. Hazaymeh & Zeitoun, 2024; Ngoc Hanh et al., 2024; Nones, 2024; J. Zhou et al., 2024).

2.3. Drought Monitoring Studies in Ethiopia

Evaluating and analyzing droughts is crucial for effective water resource management and planning, encompassing socio-economic, meteorological, hydrological, and agricultural aspects. A comprehensive understanding of historical drought occurrences and their impacts is vital for accurate drought assessment. Traditional drought assessments in Ethiopia primarily rely on ground data collection and analysis.

For instance, Abera Tareke and Gebeyehu Awoke (2022) used the Streamflow Drought Index (SDI) to analyze hydrological drought in Ethiopia, revealing that seasonal time scales exhibit a high frequency of drought with short durations, while annual analyses show low frequency but larger magnitudes. The most severe drought years were identified as 1984/85, 1986/87, 2002/03, and 2010/11. Different river basins in Ethiopia share similar characteristics, with the Omo Gibe River basin exhibiting a unique pattern.

Edossa et al. (2010) conducted a study on the Awash River Basin and found that the Middle and Lower Awash Basin experienced the most frequent and severe droughts. The most severe drought events occurred in May 1988 to June 1988 and April 1998 to May 1998 in the Middle Awash Basin. Hydrological drought events at the Melka Sedi stream gauging station lagged behind meteorological drought events in the Upper Awash by an average of seven months, with a variation ranging from three to thirteen months. Similarly, Gebreyesus et al. (2020) analyzed drought patterns in the Awash River Basin using the Reconnaissance Drought Index (RDI) and identified recurrent drought events with increasing severity, with the most severe impact observed in 1984 and the highest meteorological drought occurring in 2015.

Lemma et al. (2022) investigated the effectiveness of the CHIRPSv2 satellite rainfall product in monitoring droughts across Ethiopia's river basins using the Effective Drought Index (EDI) and the Standardized Precipitation Index (SPI). The results indicate that CHIRPSv2 effectively identifies drought periods, making it a valuable tool for drought monitoring and early warning systems in Ethiopia.

Shalishe et al. (2022) focused on the Gamo Zone in Southern Ethiopia, evaluating the CHIRPS rainfall product and its performance in assessing meteorological drought using SPI from 2000 to 2020. The study confirmed CHIRPS as a useful supplement for measuring rainfall data to estimate rainfall and drought monitoring in this region.

Tareke et al. (2022) analyzed hydrological and meteorological drought trends in the Abbay River Basin using the SDI, SPI, and RDI indices. The study found severe and extreme droughts in specific years, with significant meteorological drought trends in some stations. Abera et al. (2023) modeled agricultural drought in the South Wollo Zone using VHI and SPEI indices, highlighting the increasing frequency of droughts over 2001-2021 and demonstrating the effectiveness of these indices for agricultural drought evaluation and early warnings.

Additional studies emphasize the effectiveness of remote sensing-based monitoring and the use of cloud computing platforms like GEE to enhance analytical processes, ensuring efficiency and effectiveness in assessing drought conditions. However, limitations related to data quality, temporal resolution, sensitivity to atmospheric conditions, validation challenges, and algorithm selection emphasize the need for continual improvement for reliable drought assessments using these technologies.

2.4. GEE for Environmental Monitoring

2.4.1. Explanation and Development of GEE

Recent advancements in satellite imagery technology have made extensive data freely accessible through various U.S. Government agencies like NASA, the U.S. Geological Survey, and NOAA, as well as the European Space Agency. Numerous tools have been created to process large-scale geospatial data. However, leveraging these resources requires significant technical skills, accessibility, and resources.

A major hurdle is the need for fundamental IT management skills, including data acquisition and storage, handling complex file formats, managing databases, machine allocations, job scheduling, and networking, along with using various geospatial data processing frameworks (Gorelick et al., 2017). This technical burden can restrict many researchers and operational users from utilizing these tools, limiting access to extensive remote-sensing datasets to specialists in the field. To address these challenges and meet future needs in remote sensing applications, developing a secure, efficient, and state-of-the-art cloud computing platform is essential (Chi et al., 2016).

Cloud computing platforms provide efficient methods for storing, accessing, and analyzing datasets on powerful servers, essentially turning them into virtual supercomputers for users. These platforms offer infrastructure, storage services, and software packages in various configurations to meet diverse user needs (Chi et al., 2016). Notable cloud computing platforms include Amazon Web Services (AWS), Microsoft's Azure, and GEE, introduced by Google in 2010.

GEE is a cloud-based platform for large-scale geospatial analysis, utilizing Google's extensive computational power to address significant societal issues (Gorelick et al., 2017). It excels in handling big data analysis challenges by processing vast amounts of data rapidly. Numerous studies have used GEE for geospatial analysis across various local and global applications (Tamiminia et al., 2020). Compared to other cloud computing platforms, GEE simplifies the use of high-performance computing for managing large geospatial datasets without typical IT complexities. Additionally, GEE is accessible to everyone, user-friendly for algorithm development, and supports batch processing of image processing tools (Amani et al., 2020).

While GEE stands out for its accessibility and computational power, it also integrates a unique feature that differentiates it from other cloud platforms: its focus on collaboration and educational outreach. GEE’s collaborative environment allows users from various disciplines and skill levels to share and develop projects collectively. This approach not only accelerates scientific discovery but also democratizes access to advanced geospatial analysis tools, fostering a more inclusive research community. Additionally, GEE's extensive documentation and user community support facilitate learning and application, making it a preferred choice for educational institutions and research organizations aiming to integrate remote sensing into their curricula and research programs.

2.4.2. Key Features and Capabilities

GEE's features have been extensively discussed in the literature. Recent research categorizes its key characteristics as follows:

2.4.2.1. Computational Resources

GEE provides vast public remote sensing imagery and other ready-to-use products through a user-friendly web application. It offers researchers access to an extensive archive of public datasets, including a remote sensing archive with petabytes of cloud-stored data. Covering a range from local to global scales and spanning multiple time periods, GEE enables researchers to conduct studies with minimal costs and equipment (Kumar & Mutanga, 2018). Additionally, GEE allows users to upload and analyze their own data, use preprocessed images, and benefit from its data storage capabilities, thereby expanding research opportunities globally (Tamiminia et al., 2020).

2.4.2.2. High-Speed Computation

GEE leverages Google's powerful computing infrastructure for parallel processing of geospatial data, significantly reducing computation time. By utilizing cloud computing capabilities, GEE processes large amounts of image and vector data without local storage or analysis, facilitating fast parallel processing and the use of machine learning algorithms with Google's advanced computational resources.

2.4.2.3. Application Programming Interfaces (APIs)

GEE offers a library of APIs compatible with popular programming languages like JavaScript and Python. Its data accessibility, computing infrastructure, programming capabilities, API documentation, and Git-based script management enable both experts and those with limited programming skills to use GEE for their applications (Tamiminia et al., 2020). These features allow users to explore, analyze, and visualize geospatial big data effectively without requiring supercomputers or extensive coding skills. Earth Engine is designed to facilitate the sharing of findings between scientists, policymakers, non-profits, field personnel, and the broader community. It doesn't require proficiency in application creation, web development, or HTML to develop interactive tools or produce structured data once an algorithm is established using Earth Engine (Amani et al., 2020a).

2.4.2.4. Innovative Applications and Future Directions

Looking beyond the typical use cases, GEE is increasingly being employed in innovative applications such as real-time environmental monitoring, urban planning, and disaster response (Gorelick et al., 2017; Tamiminia et al., 2020). Its ability to handle real-time data streams and integrate with IoT devices opens new avenues for dynamic, responsive analysis of environmental changes and urban development (Amani et al., 2020). Moreover, future developments could see GEE expanding its integration with artificial intelligence and machine learning frameworks, further enhancing its capability to deliver predictive analytics and automated insights (Kumar & Mutanga, 2018). This evolution positions GEE not just as a tool for current geospatial analysis, but as a cornerstone for future smart city initiatives and environmental sustainability efforts globally (Tamiminia et al., 2020).

2.4.3. Application of GEE Cloud Computing Platform

The creation of the GEE platform aimed to facilitate the analysis and visualization of large-scale geospatial datasets within the scientific field. It has gained recognition as the most widely utilized platform for processing big geo data. By granting users free access to a range of remotely sensed datasets, GEE supports the scientific discovery process (Gorelick et al., 2017b). Users can utilize GEE through an internet-based Application Programming Interface (API) and a web-based Interactive Development Environment, without the need for web programming language. GEE possesses features such as automatic parallel processing and a fast computational platform, effectively addressing the challenges associated with processing big data (Amani et al., 2020).

Due to its capabilities in dealing with big data analysis challenges, GEE has been applied in various research areas for different purposes. Some of the major applications of GEE include Land Use/Land Cover Change, mapping irrigated cropland, forest mapping, flood mapping, drought monitoring, crop yield estimation, evapotranspiration, wetland mapping, species habitat monitoring, disease risk mapping, and natural hazard management. Mapping surface water is another application of GEE. It has been widely utilized for the mapping, detection, and monitoring of surface water. For example, Zilong et al. (2020) used GEE for surface water mapping and found that the platform can achieve greater accuracy and efficacy in complex water environments compared to traditional methodologies. Similarly, Nghia et al. (2022) used GEE to monitor and map flooding across their study area, recommending GEE for flood monitoring in other regions as well.

Tamiminia et al. (2020) analyzed 349 studies that utilized GEE as a tool for geo-big data analysis in various remote sensing applications, categorizing them into different groups. Amani et al. (2020) examined 450 GEE-related journal articles to determine the primary disciplines and subsequently divided the papers into different categories representing their main applications. A significant number of these studies applied GEE in vegetation and forest monitoring as well as land cover/use change mapping (Kumar & Mutanga, 2018). Therefore, the major applications of GEE can be categorized as follows:

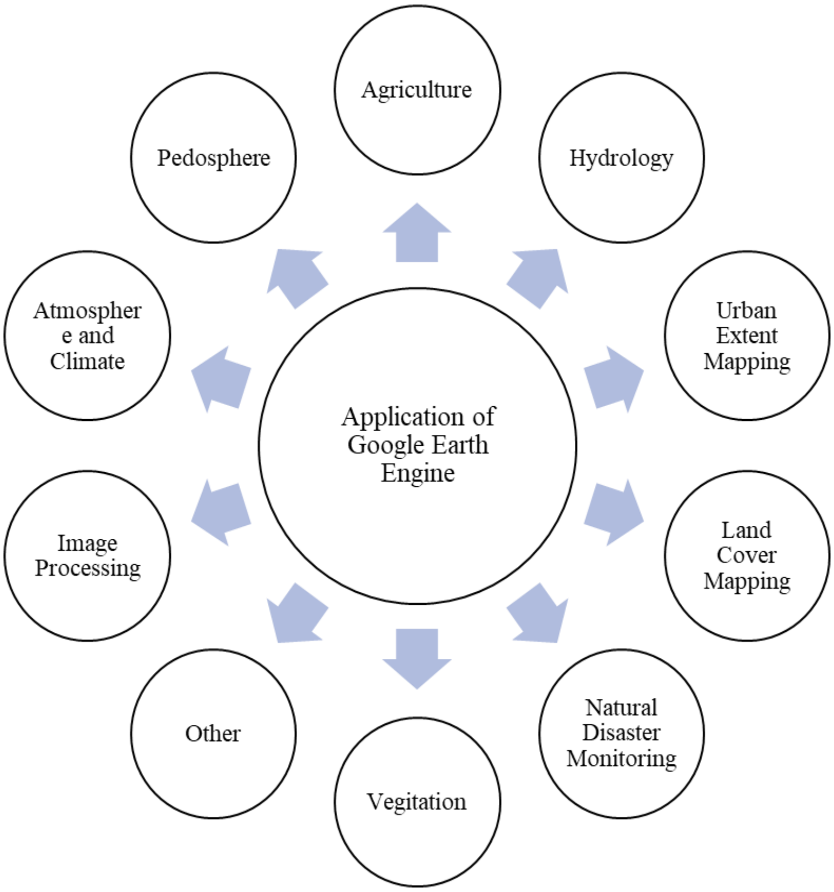

Figure 2-2 Applications of Google earth engine

(Source: Amani et al., (2020))

2.5. GEE for Environmental Monitoring

Monitoring spatiotemporal drought conditions in various climatic regions has been achieved through the utilization of the GEE and geographic information system. Several studies have been conducted worldwide using GEE as a tool for drought monitoring (Aksoy et al., 2019; Ejaz et al., 2023; Thilagaraj et al., 2021). However, in Ethiopia, limited research has been conducted using GEE for drought monitoring.

Aksoy et al., 2019 used MODIS satellite data in GEE to examine the spatial and temporal distribution of drought conditions in Turkey from 2000 to 2019. By utilizing indicators, the study evaluated the severity of drought at the country level for different months and years. The findings confirm the effectiveness of MODIS-derived drought indices for assessing geographical areas and highlight the efficiency of the GEE platform in accessing and analyzing extensive environmental data. They conclude that GEE platform not only enables monitoring of drought but also supports broader applications in environmental assessment.

Similarly, Ejaz et al., (2023) utilized Landsat-derived indices and the GEE platform to monitor drought in the Al-Lith Watershed, located in the Kingdom of Saudi Arabia. The results of their research indicate that the Vegetation Health Index (VHI) and Standardized Precipitation Evapotranspiration Index (SPEI) exhibit strong correlation as drought indices, proving their effectiveness in monitoring drought in regions with limited data, particularly hyper-arid areas. This study highlights the suitability of the GEE platform for efficient drought monitoring in challenging environments.

(Fentaw et al., 2023), examines drought dynamics in Ethiopia's Tekeze basin from 1981 to 2021 using the SPI, VCI, TCI, and VHI. Utilizing data from MODIS and CHIRPS-v2 through GEE. Results showed significant drought periods in 1984, 1985, 1987, 1993, 1997, and 2015 (SPI) and in 2002, 2004, 2009, 2015, 2016, and 2017 (VCI and TCI). NDVI trends mostly declined, except in managed areas. July rainfall was critical for NDVI, LST, TCI, and VCI, with VCI strongly correlating with precipitation. VCI identified more severe drought areas than TCI, emphasizing its importance in drought classification, particularly in drylands. The study highlights that GEE is an optimal platform for drought monitoring due to its ability to process large datasets and perform comprehensive analyses efficiently.

Furthermore, Thilagaraj et al., (2021) monitor agricultural drought in the Kodavanar watershed in the Amaravathi basin using the GEE platform. By employing remote sensing indices, the study reveals a significant decrease in healthy vegetation and a concerning rise in extreme drought conditions, particularly in 2019 and 2020. The research highlights the effectiveness of the GEE platform for monitoring agricultural drought.

To monitor drought conditions, GEE helps in assessing various drought indicators such as soil moisture, vegetation health, and precipitation anomalies. Two fundamental tasks must be performed as inputs for this method. Firstly, it is essential to choose satellite data from the GEE dataset that meets the analytical requirements. Secondly, the appropriate drought indices must be calculated by identifying the most relevant indices. Utilizing this platform, these indices can be determined over time, allowing for the creation of an updated drought severity map. In the context of this study, the availability of satellite data and the effectiveness of the chosen drought indices are important factors to consider. The capability of the indices to be used and the availability of satellite data were therefore discussed below for the current study.

2.5.1. Satellite Data and Imagery for Drought Monitoring

GEE is a comprehensive and powerful computational service that incorporates a massive, multi-petabyte data library with a highly efficient and parallel processing system (Gorelick et al., 2017). This extensive data library comprises a diverse range of freely available geospatial information, including satellite and aerial imagery from various sources, environmental data, weather and climate projections, land cover data, topographical information, and socioeconomic datasets. Moreover, the catalog is updated daily with nearly 6,000 new scenes, ensuring that it remains current with a typical delay of only 24 hours. The majority of the catalog consists of remote sensing images of the Earth from a multitude of sources.

The GEE platform hosts over 40 years of remote sensing data, sourced from an array of satellites, such as MODIS, Landsat, NOAA AVHRR, Sentinel-1, Sentinel-2, Sentinel-3, Sentinel-5P, and ALOS (Gorelick et al., 2017). In addition to offering a vast collection of raw remote sensing images, GEE users can access preprocessed, cloud-removed, and mosaicked images from the GEE data catalog.

According to Tamiminia et al. (2020), optical images sourced from MODIS and Landsat are the primary data sources employed in GEE. These sources are favored for their extensive temporal and spatial coverage, which proves valuable for various environmental monitoring applications. MODIS data, in particular, offers high temporal resolution and can be utilized for monitoring large-scale phenomena, such as vegetation conditions, land cover changes, and atmospheric properties. Consequently, considering the aforementioned literature, the utilization of MODIS is advantageous for this study.

2.5.2. Vegetation Indices

The Normalized Difference Vegetation Index (NDVI) and the Enhanced Vegetation Index (EVI) are pivotal tools for extracting vegetation, each tailored to different environmental conditions and vegetation types. NDVI is calculated using the formula:

$$NDVI = \frac{NIR + Red}{NIR - Red}$$

where NIR stands for near-infrared reflectance and Red for red light reflectance. NDVI has been extensively used in drought monitoring because it effectively indicates vegetation health by highlighting the contrast between healthy, NIR-reflective vegetation and stressed, red-reflective vegetation. This index is particularly useful in areas with moderate to sparse vegetation, where it reliably signals vegetation stress due to drought conditions (Benedict et al., 2021).

EVI, on the other hand, was developed to overcome some limitations of NDVI, particularly its tendency to saturate in regions with dense vegetation. The formula for EVI is:

$$EVI = G \times \frac{NIR - Red}{NIR + C_1 \times Red - C_2 \times Blue + L}$$

where G is a gain factor, C_1 and C_2 are coefficients for atmospheric correction, and L is a canopy background adjustment. This index includes a blue light reflectance band to correct for atmospheric conditions and reduce background noise, making it particularly effective in dense, forested areas (Priya et al., 2023).

The research conducted by Kovács, (2018) revealed the effectiveness of NDVI in monitoring drought effects on forest ecosystems in Hungary's Great Plain. The study disclosed that NDVI was particularly sensitive to vegetation changes during drought, showing significant drops during dry periods. Although EVI was also applied, it did not provide significantly different insights in this specific environment, underscoring the robustness of NDVI for drought monitoring in such regions.

Furthermore, Ozelkan et al.,(2016) examined the application of NDVI in the arid/semi-arid regions of Southeast Anatolia, Turkey, where it displayed strong correlations with the Standardized Precipitation Index (SPI) in rainfed areas. However, the correlation was weaker in irrigated areas, suggesting that while NDVI is effective in natural conditions, its accuracy can be diminished where artificial irrigation alters vegetation reflectance.

Moreover, (Priya et al., 2023) investigated vegetation dynamics in Tamil Nadu using both NDVI and EVI. Their findings indicated that while NDVI captured overall biomass intensity better, EVI offered more detailed insights into vegetation conditions, particularly in densely vegetated areas, supporting its use in high-biomass environments. Furthermore, (Wei & Fang, 2024)emphasized the adaptability of NDVI in advanced agricultural systems, such as vertical farms, where it was capable of detecting drought stress earlier than traditional visual observations, demonstrating its applicability in various contexts.

While, EVI provides certain advantages in dense, forested regions or environments with high atmospheric interference, NDVI remains the preferred index for drought monitoring in regions like the Awash River Basin due to its broader applicability, simplicity, and reliability across diverse land cover types.

2.5.2.1. Selecting Appropriate Drought Monitoring Indices

Selecting the appropriate drought monitoring indices is crucial for accurately assessing and managing drought impacts, especially in the context of climate variability. In recent decades, numerous remote sensing-based vegetation and thermal indices, such as the VCI, TCI, and VHI, have been extensively employed to detect and monitor drought conditions both regionally and globally. The choice of a suitable drought index significantly influences the precision of drought detection and monitoring. Various studies have been conducted globally to identify the most effective drought indices for different regions. For example, Ngoc Hanh et al., (2024) conducted an in-depth analysis of drought trends in Hoa Vang district, Vietnam, utilizing VCI, TCI, and VHI indices over a 30-year period (1991-2020). Their research indicated that drought severity varied across the studied years, with an observable increase in regions at higher risk of drought during the latter years, suggesting a potential escalation in drought severity over time. Similarly, Menegbo, (2024) utilized these indices in Rivers State, Nigeria, and found that VCI and VHI were reliable in indicating the absence of drought conditions, with VHI and VCI values around 4.8 and 4.7, respectively, while TCI indicated mild vegetation stress.

Factors influencing the selection of a drought index include data availability, the spatial and temporal scale of interest, research objectives, and the unique characteristics of the region being studied. The World Meteorological Organization (WMO) endorses MODIS-derived indices like VCI, TCI, and VHI as effective tools for drought assessment at various scales (Xie & Fan, 2021). These indices, particularly TCI, VCI and VHI are widely used for their proven efficacy in capturing critical aspects of drought conditions, providing comprehensive insights into vegetation health and thermal stress, as demonstrated in multiple case studies, including the Awash River Basin.

2.6. Integration of In-Situ and Remote Sensing Data for Enhanced Drought Monitoring

The integration of in-situ and remote sensing data is critical in advancing drought monitoring by merging localized accuracy with expansive spatial coverage, ultimately enabling more accurate, high-resolution assessments of drought conditions (Mukhawana et al., 2023). In-situ measurements, like soil moisture and precipitation, offer detailed accuracy but lack broad geographic representation. Remote sensing, particularly through satellite data, fills this gap by providing consistent, large-scale observations, capturing key indicators like vegetation health, land surface temperature, and soil moisture. By combining these datasets, researchers can develop precise models that facilitate timely detection and analysis of drought events. Studies highlight the efficiency of this integration, such as using Landsat data for high-resolution soil moisture estimation in drought monitoring over agricultural areas, which supports precision agriculture and early warning systems (Atnurkar & Ramadas, 2024) (Atnurkar & Ramadas, 2024). Additionally, advanced machine learning methods have been shown to improve the performance of integrated drought indexes, further enhancing accuracy and responsiveness to drought conditions (Xu et al., 2023) (Xu et al., 2023). This integrative approach enables improved drought resilience by facilitating proactive management strategies, essential for regions with limited ground-based infrastructure. The synergy between in-situ and remote sensing data in drought monitoring thus offers transformative potential, making it indispensable in the face of increasing climate variability and its impacts on agriculture and water resources.

3. MATERIALS AND METHODS

3.1. Description of the Study Area

The Awash River Basin, located in northeastern Ethiopia, is marked by diverse climatic conditions, varied topography, and significant ecological and hydrological dynamics. It plays a crucial role in the country's agriculture and water resource management. The basin is one of the 12 river basins of Ethiopia, situated between latitudes 7°53′ N and 12° N and longitudes 37°57′ E and 43°25′ E (Figure 3-1). It constitutes the central and northern part of the Rift Valley and is bounded by the Blue Nile to the west, the Rift Valley lakes to the southeast, and the Wabeshebele Basin to the south. Covering a total area of 117,772 km² and stretching over 1200 km in length, the basin is home to about 15 million inhabitants. It has been the most utilized basin in Ethiopia since the introduction of modern agriculture in the 1950s and is divided into upper, middle, and lower valleys (Gedefaw et al., 2019).

The climate of the basin is mainly tropical, with temperature variations influenced by elevation. The mean annual maximum temperature is around 30.5 °C, while the minimum averages 9.9 °C. Temperature increases in recent decades may impact agriculture and water availability. Climatic variability and land use changes increase the basin's vulnerability, emphasizing the need for adaptive management strategies.(Malede et al., 2024)

Land use and land cover changes over recent decades, driven by agricultural expansion and urbanization, have affected biodiversity and water sustainability, adding stress to the basin's ecological balance. The basin’s topography features significant elevation changes, from about 3000 m in the central highlands to approximately 250 m at Lake Abe. This varied topography contributes to climatic diversity and affects hydrology and vegetation patterns. The basin’s division into upper, middle, and lower sections comes with distinct geological and hydrological characteristics that influence water flow, soil types, and land use(Daba & You, 2022).

3.1.1. Rainfall

The rainfall patterns in the Awash Basin are highly variable and erratic, largely influenced by its diverse topography. Annual precipitation ranges from 1,600 mm in the highland’s northeast of Addis Ababa to only 160 mm in the northern part of the basin. This significant variation in rainfall suggests diverse topography and climatic conditions within the basin. The rainfall in the Middle and Lower Awash is bimodal, while in the Upper Awash, it is unimodal with one main rainy season. The Western catchment receives an average annual rainfall of 850 mm, while at the Awash headwaters, precipitation is relatively concentrated and amounts to 1,216 mm per year. In contrast, the Eastern catchment is significantly drier, with an average annual rainfall of 465 mm. The irregular rainfall profile and its temporal variability make the region susceptible to extreme weather conditions such as severe droughts and flooding, as rainfall can fluctuate greatly from year to year (Sime & Dibaba, 2023).

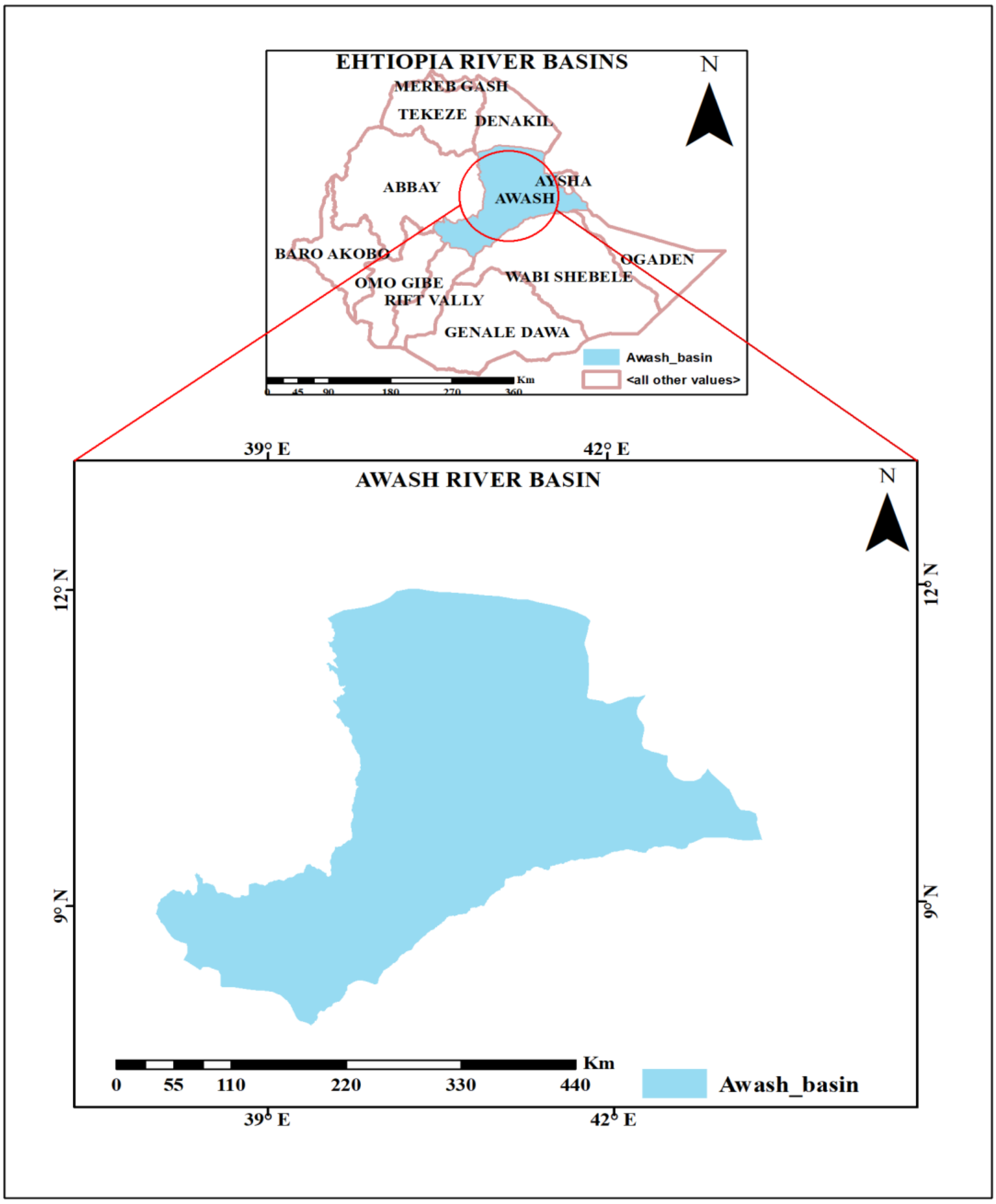

Figure 3-1 Location map of the study area

3.2. Data and Tools Used

3.2.1. The Google Earth Engine Platform

GEE is a cloud-based platform that offers the ability to conduct large-scale geospatial analysis, among other capabilities, leveraging the considerable computing power of Google to address numerous significant societal challenges (Gorelick et al., 2017). This platform features a multi-petabyte collection of satellite images and geospatial data, along with global-scale analytical tools, which empower researchers, scholars, and developers in detecting changes, plotting trends, and quantifying variations on the Earth's surface (Singh et al., 2018). Secondly, it is open-access and user-friendly, providing an appropriate environment for developing algorithms. Thus, scientists, researchers, and communities can utilize this platform to perform data analysis and create trend maps to identify resources or other related entities on the surface of the earth (Kumar & Mutanga, 2018). The GEE platform comes equipped with a free and open-access API for Python and Javascript languages. Moreover, it includes the integration of cloud computing and ready-to-use processing functions, as described by Gorelick et al. (2017). The JavaScript API, which can be accessed through a web-based integrated development environment, allows for the viewing and exporting of images, results, tables, and charts. While the Python API offers similar functionalities and processes, it lacks the visualization features of a web-based IDE. Therefore, in this study, the JavaScript API was chosen to acquire and analyze images from MODIS satellites.

3.2.2. Satellite Data

Access to cloud-free satellite images is essential to evaluating drought conditions effectively. The GEE data catalog offers optical satellite imagery from 2000 to the present, enabling researchers to conduct extensive earth-monitoring investigations. This study utilized data from the Moderate Resolution Imaging Spectroradiometer (MODIS) satellite. MODIS provides global coverage with high frequency and spatial resolutions ranging from 250 meters to 1 kilometer, making it particularly suitable for monitoring environmental changes such as drought conditions.

For the analysis of drought conditions affecting the basin, MODIS data for the period of 2000-2021 was used at different resolutions for the selected indices, as described in Table 3-1 below. This period was chosen to capture recent trends and patterns in drought severity and distribution. Specifically, the MOD11A2 V6 (Land Surface Temperature and Emissivity

8-Day, temporal resolution) and MOD13Q1 V6 (Vegetation Indices 16-Day, temporal resolution) products were employed. The MOD11A2 V6 dataset provides crucial land surface temperature data that helps assess temperature-induced stress on vegetation, which is a key factor in identifying areas prone to drought. High temperatures can exacerbate drought conditions by increasing evapotranspiration rates, leading to greater water stress on vegetation.

The MOD13Q1 V6 product, which provides the NDVI and EVI, is essential for assessing vegetation health and detecting early signs of drought. Vegetation indices are reliable indicators of plant vigor and can signal reduced photosynthetic activity due to water scarcity. The combination of temperature and vegetation indices allows for a comprehensive understanding of drought impacts, capturing both direct temperature stress and the overall condition of vegetation.

To validate the current drought assessment methodology, a comparison with historical data was conducted. For this validation, meteorological drought was assessed using the SPI for the same period. The SPI, a widely recognized drought index, was calculated using historical precipitation data to provide a comprehensive comparison with the satellite-derived drought indicators. This dual approach of using both MODIS satellite data and SPI ensures robust validation of the current methodology, facilitating a more accurate interpretation of drought trends and impacts over time.

Table 3-1 Selected satellite products used for the study

Index	Satellite Product	Spatial Resolution	Period	Provider	Temporal Resolution
TCI	MOD11A2 V6	1km*1km	2000-2021	NASA	8 Days
VCI	MOD13Q1 V6	250m*250m	2000-2021	NASA	16 Days

3.2.3. Meteorological Data

Rainfall data spanning from 2000 to 2021 were gathered from 23 meteorological stations across Awash River basin, as provided by the Ethiopian Meteorological Institute (EMI) (Appendix A.1). The names and locations of these stations are summarized in the same appendix. This rainfall data was utilized to calculate the Standardized Precipitation Index (SPI), an in-situ drought index. The SPI was then used to assess the accuracy of remote sensing-based drought indices derived from GEE.

3.3. Drought Monitoring Based on Google Earth Engine Platform

The study utilized the GEE platform to monitor drought conditions in the Awash River Basin from 2000-2021. MODIS satellite data, specifically NDVI and LST indices, were used to assess vegetation health and temperature variations. These indices were filtered and scaled to calculate the VCI and TCI, which were combined to form the VHI, offering a comprehensive measure of drought severity (Hashemzadeh Ghalhari et al., 2022). Results were visualized using time series charts and spatial maps, and the final indices were exported as TIFF images for further analysis in ArcGIS. To validate the drought assessments, the MODIS results were compared with the SPI, ensuring consistency between remote sensing and ground-based data for a reliable assessment of drought conditions in the region. The geo-referencing datum used by GEE shape-files is the WGS84 datum, ensuring consistency in spatial referencing. All steps and codes used are covered in the following sections, starting with image importation and processing of the imported images. All steps and codes used are covered in the following sections, starting with image importation and processing of the imported images.

3.3.1. Importing and Filter MODIS Satellite Images

In this study, data from the MODIS sensors onboard NASA's Terra and Aqua satellites were obtained from the GEE data catalog using specific algorithms. MODIS data is classified and processed into various products that are widely used for environmental monitoring due to their high temporal resolution and broad spectral coverage. For this study, the MODIS/061/MOD11A2 product, which provides LST data with an 8-day temporal resolution and 1 km spatial resolution, and the MODIS/006/MOD13Q1 product, offering NDVI data with a 16-day temporal resolution and 250 m spatial resolution, were used (Baser et al., 2022). These products are calibrated and corrected for various atmospheric, geometric, and radiometric distortions, ensuring consistency and reliability across the entire dataset.

All the MODIS data used in this study were sourced from the GEE platform, which provides free access to a comprehensive collection of satellite imagery. Data filtering was applied to select relevant temporal periods, specifically filtering the datasets to include only data from 2000 to 2021. This was achieved using GEE's filtering functions, which allow users to define date ranges and other criteria to extract the desired subset of data from the broader dataset. The *filterDate* function was used to constrain the dataset to the years of interest, ensuring that only the data within the specified period was analyzed.

Additionally, the area of interest (ROI) was uploaded to the Assets section on GEE using a shapefile format. The map view was centered over the ROI with a zoom level of 5 for better visualization. This shapefile was first processed in ArcGIS to ensure proper geospatial referencing and accuracy before being utilized in GEE. Figures 3-2 below illustrate the code used to import area of interest map, MODIS images and filter the data to the period select the NDVI data, and apply the corresponding visualization parameters.

```
var NDVI = ee.ImageCollection("MODIS/006/MOD13Q1");
var LST = ee.ImageCollection("MODIS/061/MOD11A2");
var ROI = ee.FeatureCollection('projects/ee-freabtenaye/assets/awash_river_basin');
Map.centerObject(ROI, 5)

// Set the start and end years for analysis.
var startyear = 2000;
var endyear = 2005;
// Set the start and end months for analysis.
var startmonth = 1;
var endmonth = 12;
// Define the date range for filtering the image collections.
var startDate = ee.Date.fromYMD(startyear, startmonth, 1);
var endDate = ee.Date.fromYMD(endyear, endmonth, 30);

// Filter NDVI images by date, spatially by the ROI, and select the 'NDVI' band for
analysis.
var filterNDVI = NDVI.filterDate(startDate, endDate)
                .filterBounds(ROI)
                .select('NDVI');
print('NDVI', filterNDVI);

// Filter LST images similarly but also map a function to add a formatted date property to
each image.

var filterLST = LST.filterBounds(ROI)
              .filter(ee.Filter.calendarRange(startyear, endyear, 'year'))
```

```
            .filter(ee.Filter.calendarRange(startmonth, endmonth, 'month'))
            .select('LST_Day_1km').map(function (img) {
              return img.set('date', img.date().format('YYYY_MM_dd'));
            });
```
Figure 3-2 Code used to import MODIS satellite images and study area map

3.3.2. Add a Day Number (dn) Property to Images

Adding Day Number Property is a function that calculates a day number (dn) for a given image based on its acquisition date. This calculation enables easier aggregation of satellite images into specific time periods, such as 8-day or 16-day composites, facilitating more efficient data analysis.

The function takes several parameters to customize its operation. The first parameter, img, represents the input image to which the day number will be added. The second parameter, *beginDate*, specifies the starting date for the calculation; if not provided, it defaults to the image's acquisition date, ensuring the function operates on the most relevant temporal data. The third parameter, *IncludeYear*, is a *boolean* that indicates whether to include the year in the day number format, allowing for a clearer contextual understanding of the aggregated data. Finally, the parameter n defines the number of days in each aggregation period, defaulting to 8. This flexibility allows users to customize the aggregation according to their specific analytical needs.

This function enhances the capability to manage and analyze satellite imagery by providing a systematic way to categorize and aggregate images based on their acquisition dates. The code used for this function is shown in Figure 3-3.

```
// Function to add a day number (dn) property to images
var add_dn_date = function(img, beginDate, IncludeYear, n) {
   beginDate = beginDate || img.get('system:time_start');
   if (IncludeYear === undefined) { IncludeYear = true; }
   n = n || 8;
   beginDate = ee.Date(beginDate);
   var year = beginDate.get('year');
   var diff = beginDate.difference(ee.Date.fromYMD(year, 1, 1), 'day').add(1);
   var dn = diff.subtract(1).divide(n).floor().add(1).int();
```

```
    var yearstr = year.format('%d');
    dn = dn.format('%02d');
    dn = ee.Algorithms.If(IncludeYear, yearstr.cat("-").cat(dn), dn);
    return ee.Image(img)
        .set('system:time_start', beginDate.millis())
        .set('date', beginDate.format('yyyy-MM-dd'))
        .set('year', yearstr)
        .set('month', beginDate.format('MM'))
        .set('yearmonth', beginDate.format('YYYY-MM'))
        .set('dn', dn);
```

Figure 3-3 Code used to add a day number (*dn*) property to images

3.3.3. Wrapper Day Number Property to Images

The *Wrapper Function for Day Number* simplifies the application of the *add_dn_date* function by providing default values for its parameters, thereby enhancing code readability and usability. This function is particularly useful when processing multiple images, as it streamlines the process and reduces the need to repeatedly specify parameters.

The wrapper function accepts optional parameters, including *IncludeYear*, which determines whether to include the year in the day number format, defaulting to true, and n, which specifies the number of days in each aggregation period and defaults to 8. By returning a new function that applies *add_dn_date* with the specified or default parameters, this wrapper facilitates efficient processing of images without the need to define parameters each time.

This wrapper enhances user experience and code maintainability, making it easier to work with the images. The code used for this function is shown in Figure 3-4.

```
// Wrapper function to apply the add_dn_date function with default parameters.
var add_dn = function(IncludeYear, n) {
    if (typeof IncludeYear === 'undefined') { IncludeYear = true; }
    if (typeof n === 'undefined') { n = 8; }
    return function (img) {
        return add_dn_date(img, img.get('system:time_start'), IncludeYear, n);
    };
}
```

Figure 3-4 Code used wrapper day number property to images

3.3.4. Validate Lists for Aggregation Operations

Validate Aggregation Lists is a function that ensures the lists of bands and reducers are formatted correctly for aggregation operations in GEE. This function is essential for applying multiple reducers across multiple bands effectively, preventing errors that could arise from improperly formatted inputs.

The function takes parameters for the *bandList*, *reducerList*, and the image collection *(ImgCol).* It converts inputs into arrays if they are not already formatted as such, which is crucial for ensuring that the aggregation process can proceed without issues. Additionally, it handles cases where there is only one band but multiple reducers, replicating the band as necessary to accommodate all specified reducers. This ensures that each reducer has a corresponding band, maintaining the integrity of the analysis.

In conjunction with this function, the Function to Get Last Image from Collection retrieves the most recent image from an image collection, which is particularly useful for temporal analysis or monitoring changes over time. By allowing users to specify how many of the last images to retrieve, this function facilitates quick access to the most relevant data for analysis.

The Function to Copy Properties Between Images plays a crucial role in maintaining metadata consistency across images. By copying specified metadata properties from a source image to a destination image, this function ensures that important attributes are preserved after transformations. This functionality is vital for maintaining accurate and consistent metadata, which is essential for reliable data interpretation.

Together, these functions enhance the workflow for processing satellite imagery by ensuring that images are correctly accessed, properties are maintained, and aggregation lists are validated, contributing to more efficient and accurate data analysis in GEE. The code used for the Validate Aggregation Lists function is shown in Figure 3-5.

```
// Function to get the last image from an image collection.
var imgcol_last = function(imgcol, n) {
   n = n || 1;
   var res = imgcol.toList(n, imgcol.size().subtract(n));
   if (n <= 1) { res = ee.Image(res.get(0)); }
   return res;
}
```

```
// Function to copy properties from one image to another.
var copyProperties = function(source, destination, properties) {
    properties = properties || destination.propertyNames();
    return source.copyProperties(destination)
                .copyProperties(destination, properties);
};
// Function to validate lists for aggregation operations.
var check_aggregate = function(bandList, reducerList, ImgCol) {
    function check_list(x) {
        if (!Array.isArray(x)) x = [x];
        return x;
    }
    reducerList = reducerList || ['mean'];
    bandList = bandList || ImgCol.first().bandNames();
    reducerList = check_list(reducerList);
    bandList = check_list(bandList);

    if (bandList.length === 1 && reducerList.length > 1) {
        temp = bandList[0];
        bandList = [];
        reducerList.forEach(function (reducer, i) {
            bandList.push(temp);
        });
    }
    return { bandList: bandList, reducerList: reducerList };
}
```
Figure 3-5 Code used to validate lists for aggregation operations

3.3.5. Image Collection Aggregation

Image collection aggregation is one of the key steps in the following code (Figure 3-6) because it allows for multiple satellite images to be synthesized, captured over a defined time. This step is very important for the analysis of trends and patterns that would be difficult to assess in original image data. This aggregation logic is implemented in the *aggregate_process* function, which further breaks down an image collection with common properties like year or month and applies multiple statistical reducers, like mean or sum, to create summary images (Gorelick et al., 2017).

To begin with, the collection of images is filtered and sorted in terms of time of acquisition to ensure that the aggregation happens chronologically. It is especially important in time series analysis where one needs to represent change over time accurately. The function iterates over the selected bands and reducers, aggregating the images together to form a new image that contains statistical information from the initial collection of images. When the delta parameter is set to true, it can calculate the difference between the first and last images and provide further insight into the change rather than just on the aggregated values.

Furthermore, the aggregate picture holds onto important metadata, such as the date of acquisition, through copying properties from the first image in the series. This can be useful for further analysis and visualization. A big advantage of image collection aggregation is that it can help alleviate the problem of cloud cover. Temporal averaging of images minimizes those transient clouds that may have been blocking individual images, hence providing a less noisy dataset and more reliable information on vegetation health, temperature, and other ecologically related indicators (Chapman et al., 2013). Thus, with aggregation, not only are the data complications reduced but also the quality of analysis improved, taking into account the effects from cloud cover.

However, there are several challenges associated with aggregate image collection. One significant challenge is the data size; aggregating high-resolution satellite images over large time frames and areas can lead to massive data volumes, which can strain storage and processing capabilities. The temporal and spatial resolution of satellite images also presents a challenge. Variations in these resolutions can complicate the process of aligning and aggregating images accurately, as different satellites might capture data at different intervals and scales (X. Zhou & Wei, 2024).

Varying image characteristics, such as differences in spectral bands, calibration settings, or sensor types, can further add complexity to the aggregation process. These discrepancies can lead to inconsistencies in the aggregated output unless harmonized properly. Additionally, computational limits pose a substantial challenge. Aggregating and processing large image collections can require significant computational power and memory, potentially necessitating the use of advanced cloud computing resources or specialized software to handle the workload efficiently. These challenges need to be carefully managed to achieve meaningful and reliable aggregation results.

```
// Function to aggregate images in a collection based on a property and reducers.
var aggregate_process = function (ImgCol, prop, prop_val, bandList, reducerList, delta) {
    var nreducer = reducerList.length;
    var imgcol = ImgCol.filterMetadata(prop, 'equals', prop_val).sort('system:time_start');
    var first = ee.Image(imgcol.first());
    var last = imgcol_last(imgcol);
    var ans = ee.Image([]);
    if (!delta) {
        for (var i = 0; i < nreducer; i++) {
            var bands = bandList[i];
            var reducer = reducerList[i];
            var img_new = imgcol.select(bands).reduce(reducer);
            ans = ans.addBands(img_new);
        }
    } else {
        ans = last.subtract(first);
    }
    return copyProperties(ee.Image(ans), first);
}
var aggregate_prop = function (ImgCol, prop, reducerList, bandList, delta) {
    if (delta === undefined) { delta = false; }
    var dates = ee.Dictionary(ImgCol.aggregate_histogram(prop)).keys();
    var options = check_aggregate(bandList, reducerList, ImgCol);
    function process(prop_val) {
        return aggregate_process(ImgCol, prop, prop_val,
            options.bandList, options.reducerList, delta);
    }
    var ImgCol_new = dates.map(process);
    var bands = ee.List(options.bandList).flatten();
    var out = ee.ImageCollection(ImgCol_new);
    if (options.reducerList.length === 1) {
```

```
        out = out.select(ee.List.sequence(0, bands.length().subtract(1)), bands);
    }
    return out;
};
```
Figure 3-6 Code used to aggregate image collection

3.3.6. Applying Day Number (dn) Property to the LST Images

Applying the day number (dn) property to LST images is crucial for standardizing their temporal resolution, which enables comparisons with other datasets NDVI. This process involves using the *add_dn* function to assign a day number to each image, including the year and setting the aggregation period to 16 days. After verifying the day numbers, the *aggregate_prop* function calculates the mean LST values over each 16-day period, resulting in a new image collection. The code used for this process is shown in Figure 3-7.

```
// Apply the day number property to the LST images and aggregate into 16-day
composites.
filterLST = filterLST.map(add_dn(true, 16));
print('orig LST', filterLST);
var lst16days = aggregate_prop(filterLST, "dn", 'mean');
print('LST', lst16days);
```
Figure 3-7 Code used to apply dn property to the LST images

3.3.7. Scaling NDVI and LST Values

The preparation of NDVI and Land Surface Temperature (LST) data involves scaling the values to ensure accurate analysis. NDVI values are commonly stored as integers to save storage space, requiring a multiplication factor of 0.0001 to convert them to the appropriate range of -1 to 1. This scaling is crucial because the original integer values represent a broader range that needs accurate interpretation for reliable analysis. According Huete et al., (2002), this scaling technique helps maintain precision while minimizing file size, ensuring that processed NDVI values accurately reflect vegetation health and cover, facilitating meaningful comparisons and insights.

For LST data, values are expressed in Kelvin, and converting them to Celsius is essential for practical applications. This conversion is achieved by subtracting 273.15 from the Kelvin values. Additionally, LST values in the MOD11A2 product are scaled by a factor of 0.02 to improve data interpretability. This scaling enhances storage efficiency since raw temperature values can be large integers, making the data more manageable without significant loss of precision. While it is possible to analyze LST values in Kelvin, Celsius is more intuitive for most applications, especially in environmental studies.

To apply these adjustments to each image in the *filterNDVI* and lst16days collections, a mapping function is used. For NDVI, the function multiplies the values by 0.0001, and for LST, another function scales the values by 0.02 and converts them to Celsius. Both functions also copy essential properties, such as *system:time_start* and *system:time_end*, from the original images to maintain metadata integrity. The code for these processes is shown in Figures 3-8:

```
// Scale NDVI values by the appropriate factor (0.0001)
var scaledNDVI = filterNDVI.map(function(img){
   return img.multiply(0.0001)
            .copyProperties(img, ['system:time_start', 'system:time_end']);
});
// Convert LST from Kelvin to Celsius
var scaledLST = lst16days.map(function(img){
   return img.multiply(0.02).subtract(273.15)
            .copyProperties(img, ['system:time_start', 'system:time_end']);
});
```

Figure 3-8 Code used to scale NDVI and LST values

3.3.8. Calculating Vegetation Condition Index (VCI)

VCI serves as a crucial metric for monitoring and evaluating agricultural drought, offering a sophisticated understanding of vegetation response to fluctuations in precipitation and water stress conditions. In contrast to the more generalized NDVI, VCI specifically accounts for the relative changes in vegetation health over time by normalizing NDVI values against historical minimum and maximum records for each pixel (Liu & Kogan, 1996). This methodology renders VCI particularly effective in differentiating between short-term anomalies and long-term trends in vegetation stress, thus providing a more reliable indicator of drought impact. The VCI is calculated using the following formula:

$$VCI = \frac{(\mathrm{NDVI}_i - \mathrm{NDVI}_{\min})}{(\mathrm{NDVI}_{\max} - \mathrm{NDVI}_{\min})} \times 100$$

Where:

$NDVI_i$ represents the NDVI value for each image,

$NDVI_{min}$ is the minimum NDVI value, and

$NDVI_{max}$ is the maximum NDVI value.

VCI values range from 0 to 100, with higher values indicating healthier vegetation and lower drought intensity. Research has demonstrated that VCI not only correlates strongly with crop yield reductions during drought years but also serves as a predictive tool for identifying areas at risk of severe drought before visible signs of stress appear. For instance, a study by Kogan, (1995) linked VCI values between 0 and 35 to a significant 20% reduction in corn yield, establishing this range as a critical threshold for drought severity classification. Building on this, the VCI scale has been further refined into five categories: no drought (VCI > 70), mild drought ($50 < VCI \leq 70$), moderate drought ($30 \leq VCI \leq 50$), severe drought ($20 \leq VCI \leq 30$), and extreme drought (VCI < 20)(Dutta et al., 2015; Liang et al., 2021; Qian et al., 2016).

Furthermore, VCI has been widely adopted in various global drought monitoring systems due to its robustness and adaptability across different climatic regions. It is particularly valuable in regions where ground-based measurements are scarce, as it utilizes satellite-derived data to provide continuous, large-scale monitoring. This capability has established VCI as a fundamental component in early warning systems, enabling proactive measures to mitigate the impacts of drought on agriculture and food security. The code for this process is shown in Figure 3-9:

```
// Compute the Vegetation Condition Index (VCI) using the scaled NDVI data.
var VCI = scaledNDVI.map(function(image){
   var Imin = scaledNDVI.reduce(ee.Reducer.min());
   var Imax = scaledNDVI.reduce(ee.Reducer.max());
   return image.expression('(Ia-Imin)/(Imax-Imin)*100',
   {
      Ia: image,
      Imin: Imin,
      Imax: Imax
   }).clip(ROI).rename('VCI')
     .copyProperties(image, ['system:time_start', 'system:time_end']);
```

```
});
print('VCI', VCI);
// Add the VCI layers to the map for visualization.
Map.addLayer(VCI, VisParams, 'VCI');
```

Figure 3-9 Code used to calculate vegetation condition index

3.3.9. Calculating Temperature Condition Index (TCI)

The TCI is a critical metric used in monitoring vegetation stress due to temperature variations, particularly in drought-prone areas. The TCI is valuable in assessing the impact of temperature extremes on vegetation health by comparing current temperature conditions to historical extremes (Kogan, 1995). For the present study, the TCI was calculated to evaluate vegetation stress across the study area. The TCI is based on the principle that vegetation stress increases as the temperature deviates from the optimal range for plant growth. The TCI is calculated using the following formula:

$$TCI = \frac{(Tmax - T)}{(Tmax - Tmin)} * 100$$

Where:

T represents the current LST of observed period,

T_{max} is the maximum temperature observed during the period of interest, and

T_{min} is the minimum temperature observed during the same period.

The TCI values range from 0 to 100, where higher values indicate less stress and better vegetation conditions, while lower values reflect higher stress levels.

The TCI was computed utilizing satellite-derived LST data from the MODIS sensor. The LST data was processed and analyzed using GEE. The computation involved applying the TCI formula to the temperature datasets, wherein each pixel's temperature value was compared against the maximum and minimum temperatures observed across the entire study period. The resulting TCI values were subsequently mapped to visualize areas experiencing varying levels of vegetation stress(Tucker & Choudhury, 1987).

The TCI thresholds were established to categorize the stress levels into distinct classes, employing the same thresholds as those applied to the VCI. These thresholds are based on existing literature and were selected to provide a clear differentiation of stress levels in the study area. As illustrated in Figure 3-10, the TCI calculation process facilitated the identification of areas within the study region most affected by temperature-induced stress. This provided critical insights into vegetation health and highlighted the potential impacts of ongoing drought conditions.

```
// Compute the Temperature Condition Index (TCI) using the scaled LST data.
var TCI = scaledLST.map(function(image){
    var Imin = scaledLST.reduce(ee.Reducer.min());
    var Imax = scaledLST.reduce(ee.Reducer.max());
    return image.expression('(Imax-Ia)/(Imax-Imin)*100',
    {
        Ia: image,
        Imin: Imin,
        Imax: Imax
    }).clip(ROI).rename('TCI')
      .copyProperties(image, ['system:time_start', 'system:time_end'])
      .set('date', image.date().format('YYYY_MM_dd'));
});
print('TCI', TCI);
// Load a color palette.
var assets = require('users/gena/packages:palettes');
// Visualization parameters for displaying the indices.
var VisParams = {
    min: 0,
    max: 100,
    palette: assets.colorbrewer.RdYlGn[9]
};
// Add the TCI layers to the map for visualization.
Map.addLayer(VCI, VisParams, 'VCI');
Map.addLayer(TCI, VisParams, 'TCI');
```

Figure 3-10 Code used to calculate temperature condition index

3.3.10. Calculating the Vegetation Health Index (VHI)

The VHI is a robust metric utilized to assess vegetation health by integrating both the VCI and the TCI. This integration facilitates a comprehensive evaluation of vegetation health, accounting for both moisture availability and temperature stress, which are critical factors influencing vegetation growth, particularly in arid and semi-arid regions.

Research has consistently shown that the VHI is highly effective in monitoring agricultural drought and evaluating the influence of weather conditions on vegetation. Zeng et al., (2022) highlighted that the integration of the VCI and the TCI within VHI is crucial for accurately mapping the spatial extent, intensity, and severity of agricultural droughts. The common practice is to apply equal weighting to VCI and TCI, reflecting the often-uncertain contributions of moisture and temperature to overall vegetation health, as noted by Kogan (Karnieli et al., 2006). VHI is calculated as a weighted sum of VCI and TCI, a method first introduced by Kogan (1995), and typically involves assigning a weight of 0.5 to each component. This balanced approach provides a comprehensive assessment of vegetation health, recognizing that stressed vegetation usually correlates with lower-than-normal NDVI values and higher-than-normal temperatures. The VHI is determined using the following formula:

$$VHI = \alpha \times VCI + (1 - \alpha) \times TCI$$

Where:

α = The contributions of the VCI and the TCI to the VHI

VCI = Vegetation condition index

TCI = Temperature Condition Index

VHI = Vegetation health index

In this study, the VHI can be calculated by first creating a combined image collection of VCI and TCI in GEE. The methodology begins by defining a filter to match images by their *system:time_start* property, ensuring that the indices correspond to the same time periods. Subsequently, the VHI is computed as the average of VCI and TCI. In this implementation, the expression $0.5 \times a + (1 - 0.5) \times b$ ensures that both VCI and TCI are equally weighted in the calculation of VHI. The value of 0.5 for each index reflects the standard practice of treating moisture availability and temperature stress as equally important factors affecting vegetation health. By combining these indices, the VHI provides a balanced assessment of vegetation health, making it valuable for environmental monitoring and management applications. The VHI thresholds were established to categorize the stress levels into distinct classes, employing the same thresholds as those applied to the VCI. The code for calculating VHI is included in Figure 3-11:

```
// Define a filter to join VCI and TCI images by matching the 'system:time_start'
property.
var filter = ee.Filter.equals({
   leftField: 'system:time_start',
   rightField: 'system:time_start'
});

// Define the join operation to combine the two collections.
var join = ee.Join.saveFirst({
   matchKey: 'match',
});

// Apply the join to create a combined image collection of VCI and TCI.
var both = ee.ImageCollection(join.apply(VCI, TCI, filter))
         .map(function(image) {
            return image.addBands(image.get('match'))
                     .set('date', image.date().format('YYYY_MM_dd'));
         });
// Compute the Vegetation Health Index (VHI) as the average of VCI and TCI.
var VHI = both.map(function(img) {
   return img.addBands(
      img.expression('a1/2 + b1', {
         a1: img.select('VCI'),
         b1: img.select('TCI'),
      }).rename('VHI')).select('VHI');
});
print('VHI', VHI);

// Add the VHI layer to the map for visualization.
Map.addLayer(VHI, VisParams, 'VHI');
```

Figure 3-11 Code used to calculate vegetation health index

3.3.11. Calculating Area under Different Drought Categories

Calculating the areas affected by different drought severity categories is essential for understanding the spatial extent of drought impact over time. This information is crucial for monitoring drought conditions, assessing the vulnerability of regions to drought, and supporting informed decision making for resource management and disaster preparedness. By quantifying areas under various drought conditions, stakeholders can better evaluate the effectiveness of mitigation strategies, plan future interventions, and track long-term environmental trends.

The code in Figure 3-12 is designed to calculate the areas affected by different drought severity categories—No Drought, Mild Drought, Moderate Drought, Severe Drought, and Extreme Drought—utilizing indices such as the VCI, TCI, and VHI over a specified ROI. The process commences with the calculation of the pixel area in square meters within the ROI, followed by the classification of each pixel based on the index value into predefined drought categories. The code employs the *reduceRegion* function to sum the areas of pixels in each category, and these areas are subsequently reported in square kilometers.

Calculating areas under different drought categories presents several challenges. One significant challenge is the need to utilize the quality assessment (QA) of data to ensure accuracy, as inconsistencies or data noise can affect the reliability of the results. Additionally, the complexity of drought impacts, which can be influenced by factors such as land use, land cover, and soil type, adds to the difficulty in obtaining precise measurements. These factors can introduce variability and necessitate careful interpretation of the results (Gottfriedsen et al., 2021). Calculations were performed for each image in the *ImageCollection*, facilitating the temporal analysis of drought conditions. The results were returned as a feature collection, with each feature corresponding to a specific date, and containing the calculated areas for each drought category. This feature collection was printed on the console, providing a clear, date-specific summary of drought-affected areas. The ability to map these calculations over time enables users to track the evolution of drought severity across a region, offering valuable insights for managing and mitigating drought impacts. This code demonstrates versatility and can be adapted to other environmental indices, rendering it a powerful tool for Earth observation and environmental monitoring.

```
// Function to classify drought categories and calculate area for a given index (VCI, TCI, or VHI)
```

```
var classifyAndCalculateArea = function(image, indexName) {
    var areaImage = ee.Image.pixelArea().addBands(image);
    var noDrought = areaImage.updateMask(image.gt(70)).reduceRegion({
        reducer: ee.Reducer.sum(),
        geometry: ROI,
        scale: 250,
        maxPixels: 1e13
    }).get('area');

    var mildDrought =
areaImage.updateMask(image.gt(50).and(image.lte(70))).reduceRegion({
        reducer: ee.Reducer.sum(),
        geometry: ROI,
        scale: 250,
        maxPixels: 1e13
    }).get('area');

    var moderateDrought =
areaImage.updateMask(image.gte(30).and(image.lte(50))).reduceRegion({
        reducer: ee.Reducer.sum(),
        geometry: ROI,
        scale: 250,
        maxPixels: 1e13
    }).get('area');

    var severeDrought =
areaImage.updateMask(image.gte(20).and(image.lt(30))).reduceRegion({
        reducer: ee.Reducer.sum(),
        geometry: ROI,
        scale: 250,
        maxPixels: 1e13
    }).get('area');
```

```
  var extremeDrought = areaImage.updateMask(image.lt(20)).reduceRegion({
    reducer: ee.Reducer.sum(),
    geometry: ROI,
    scale: 250,
    maxPixels: 1e13
  }).get('area');

  var totalArea = areaImage.reduceRegion({
    reducer: ee.Reducer.sum(),
    geometry: ROI,
    scale: 250,
    maxPixels: 1e13
  }).get('area');

  var otherArea = ee.Number(totalArea).subtract(noDrought).subtract(mildDrought)
    .subtract(moderateDrought).subtract(severeDrought).subtract(extremeDrought);
   // Return a Feature with the calculated areas and the date
  return ee.Feature(null, {
    'Index': indexName,
    'Date': image.date().format('YYYY-MM-dd'),
    'No Drought Area (sq km)': noDrought.divide(1e6),
    'Mild Drought Area (sq km)': ee.Number(mildDrought).divide(1e6),
    'Moderate Drought Area (sq km)': ee.Number(moderateDrought).divide(1e6),
    'Severe Drought Area (sq km)': ee.Number(severeDrought).divide(1e6),
    'Extreme Drought Area (sq km)': ee.Number(extremeDrought).divide(1e6),
    'Total Area (sq km)': ee.Number(totalArea).divide(1e6)
  });
};
// Map over the entire collection to calculate the drought-affected areas for each date
var droughtAreaVCI = VCI.map(function(image) {
  return classifyAndCalculateArea(image, 'VCI');
});
var droughtAreaTCI = TCI.map(function(image) {
```

```
    return classifyAndCalculateArea(image, 'TCI');
});

var droughtAreaVHI = VHI.map(function(image) {
    return classifyAndCalculateArea(image, 'VHI');
});

// Print the results for all images in the collections
print('Drought Affected Area for VCI:', droughtAreaVCI);
print('Drought Affected Area for TCI:', droughtAreaTCI);
print('Drought Affected Area for VHI:', droughtAreaVHI);
var vciFirstFeature = droughtAreaVCI.first();
var vciFormatted = {
    'Index': vciFirstFeature.get('Index').getInfo(),
    'Date': vciFirstFeature.get('Date').getInfo(),
    'No Drought Area (sq km)': vciFirstFeature.get('No Drought Area (sq km)').getInfo(),
    'Mild Drought Area (sq km)': vciFirstFeature.get('Mild Drought Area (sq
km)').getInfo(),
    'Moderate Drought Area (sq km)': vciFirstFeature.get('Moderate Drought Area (sq
km)').getInfo(),
    'Severe Drought Area (sq km)': vciFirstFeature.get('Severe Drought Area (sq
km)').getInfo(),
    'Extreme Drought Area (sq km)': vciFirstFeature.get('Extreme Drought Area (sq
km)').getInfo(),
    'Total Area (sq km)': vciFirstFeature.get('Total Area (sq km)').getInfo()
};
print('Formatted Drought Affected Area for VCI (First Date):', vciFormatted);
```
Figure 3-12 Code used to calculate area under different drought categories

3.3.12. Generating Time Series Charts

Time series analysis of the VCI, TCI, and VHI is essential for comprehending the dynamics of vegetation health over time. Through continuous monitoring of these indices, researchers can track vegetation responses to environmental factors, including climatic variations, seasonal changes, and anthropogenic activities (D. Zhang et al., 2023).

The present study generating the time series charts typically involves the utilization of GEE's *Chart.image.seriesByRegion* function. This function plots the mean value of the index for a defined ROI over time, providing a clear visual representation of trends and variations (Gorelick et al., 2017). This approach enables a comprehensive analysis of vegetation health by examining both moisture and temperature conditions simultaneously. By visualizing the data in time series format, significant trends, anomalies, and correlations are elucidated, facilitating the interpretation of complex information by stakeholders—such as policymakers and land managers—to make informed decisions regarding land use, crop management, and conservation efforts. Below in Figure 3-13 are code used to generate the time series charts for VCI, TCI, and VHI:

```
// Generate and display time series charts for the selected period.
// VCI Time Series Chart
var VCI_TS_CHART = Chart.image.seriesByRegion(VCI, ROI, ee.Reducer.mean(),
'VCI', 1000, 'system:time_start').setOptions({
   title: 'VCI Time Series (' + startyear.toString() + '-' + endyear.toString() + ')',
   vAxis: { title: 'VCI Index' },
});
print(VCI_TS_CHART);
// TCI Time Series Chart
var TCI_TS_CHART = Chart.image.seriesByRegion(TCI, ROI, ee.Reducer.mean(),
'TCI', 1000, 'system:time_start').setOptions({
   title: 'TCI Time Series (' + startyear.toString() + '-' + endyear.toString() + ')',
   vAxis: { title: 'TCI Index' },
});
print(TCI_TS_CHART);
// VHI Time Series Chart
var VHI_TS_CHART = Chart.image.seriesByRegion(VHI, ROI, ee.Reducer.mean(),
'VHI', 1000, 'system:time_start').setOptions({
   title: 'VHI Time Series (' + startyear.toString() + '-' + endyear.toString() + ')',
   vAxis: { title: 'VHI Index' },
});
print(VHI_TS_CHART);
```

Figure 3-13 Code used to generate time series charts

3.4. Drought Monitoring Based on In-Situ Data

Drought monitoring using in-situ data highlights the importance of ground-based observations for assessing and tracking drought conditions. These observations provide direct, real-time measurements that are essential for validating and complementing satellite-based remote sensing data. Among the various parameters, rainfall data is the most critical for identifying drought. Long-term precipitation records allow for the calculation of drought indices, which quantify deviations from normal precipitation patterns over various timescales.

In the present study, rainfall data from 21 stations in the Awash River Basin, collected by the Ethiopian Meteorological Institute, was utilized to monitor drought conditions. The SPI was employed to assess drought severity due to its ability to measure precipitation deficits across multiple timescales. Developed by McKee *et al.*, (1993), the SPI has since become one of the most important indices for quantifying meteorological drought on different time scales. The calculation of SPI is based on the probability of precipitation for any given time scale, making it a reliable indicator for monitoring drought conditions (Dutta et al., 2013).

Ensuring data quality is crucial for accurately monitoring drought conditions and conducting reliable analysis.

3.4.1. Data Quality Analysis

i. Filling of Missed Data

After collecting the necessary rainfall data, the next step involves preparing the data for analysis, ensuring that it aligns with the objectives of the study. A common challenge encountered during this phase is the presence of missing values within the dataset. To address this, a robust data imputation technique was applied using the Multiple Imputation by Chained Equations (MICE) method in R. Multiple Imputation was then performed using the MICE package in R, with Predictive Mean Matching (PMM) as the chosen imputation method. This technique involved creating five imputed datasets, from which one was selected for further analysis. The use of PMM ensured that the imputed values were plausible and consistent with the observed data, thereby enhancing the reliability of the dataset (Gao et al., 2018). The code used for this imputation process is illustrated in Figure 3-14.

```
# Install and load necessary packages
library(readxl)   # for reading Excel files
```

```
library(mice)     # for multiple imputation
library(dplyr)    # for data manipulation
library(writexl)  # for writing Excel files

# Read the Excel file.
data<-read_excel("E:/Data_for_Thesis/Hydro-Met
Data/Stational_RF_Data/Monthly/Akaki.xlsx")

# Check for missing values before imputation
print(colSums(is.na(data)))

# Replace specific string representations of missing values with NA
data <- data %>%
  mutate_all(~ ifelse(. %in% c(' ', '-   ', '-', '         '), NA, .))
# Perform multiple imputation using MICE
imputed_data <- mice(data, method = "pmm", m = 5, maxit = 50, seed = 123)

# Combine the imputed datasets
completed_data <- complete(imputed_data, 1)

# Check for missing values after imputation
print(colSums(is.na(completed_data)))

# Write the imputed data back to an Excel file
write_xlsx(completed_data, "C:/Users/WRE LAB/Documents/Filled-rainfall-data/Akaki-
filled.xlsx")
```

Figure 3-14 Code used to fill missed rainfall data

ii. **Consistency Test for the Data Series**

The consistency of the cumulative annual maximum rainfall records for 23 stations in the Awash River Basin was evaluated using the Double Mass Curve method. This approach compares the cumulative annual maximum rainfall, and the consistency of cumulative annual maximum rainfall records for 23 stations in the Awash River Basin was evaluated using the Double Mass Curve method. This approach compares the cumulative annual maximum rainfall of each station against the cumulative rainfall of nearby reference stations, typically calculated as the mean of the data from several neighboring stations. The cumulative pairs are plotted in an XY coordinate system, where a linear trend indicates data consistency, while a break in the slope suggests inconsistencies requiring correction.

The analysis depicted in Figure 4.12, show that the rainfall data from most stations follow a straight-line relationship, confirming consistency and reliability. One notable exception was the Debre Sina station, which exhibited a slight deviation from the linear trend. However, this variation is not significant enough to affect the overall reliability of the data, and may be due to local environmental factors or minor data discrepancies.

The Double Mass Curve method, known for its simplicity and practicality, is widely employed for assessing consistency and long-term trends in hydrometeorological data (Pirnia et al., 2018). The consistency observed across the majority of the Awash River Basin stations ensures the validity of future analyses involving rainfall and drought trends in the region, despite differences in rainfall distribution, with the middle basin receiving less rainfall than the upper basin. Overall, the consistency of the rainfall records across the stations supports their use in further drought analyses. This robust evaluation confirmed that rainfall data are suitable for comprehensive drought studies in the Awash River Basin.

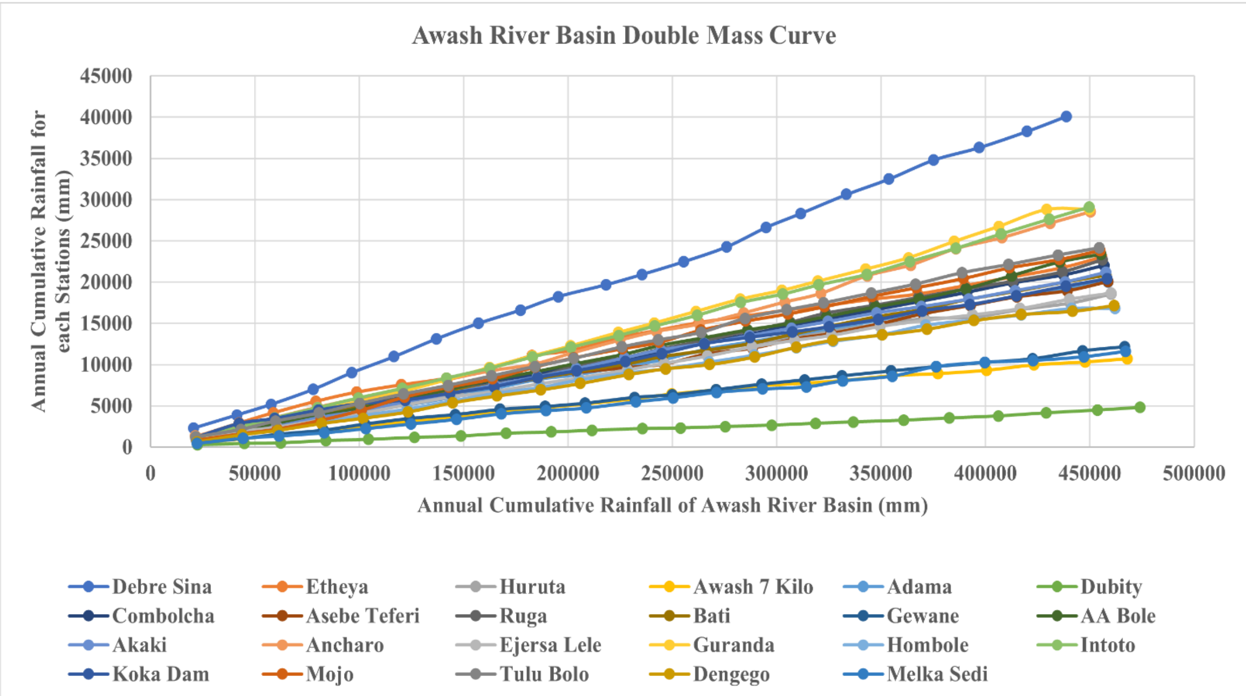

Figure 3-15 Data consistency analysis using double mass curve for Awash River Basin

iii. Homogeneity Test for the Data Series

Homogeneity testing is essential in time-series analysis to ensure reliable statistical models, particularly in meteorology. Various methodologies assess homogeneity with distinct advantages, including the Von Neumann ratio (VNR), Pettitt's test, the standard normal homogeneity test (SNHT), and the Buishand range test (BRT) (Machiwal et al., 2022). The BRT, implemented using RAINBOW software in this study, evaluates cumulative deviations from the mean, focusing on the maximum deviation (Q) and range (R). Additionally, the detected change points were homogenized using R Studio, further enhancing data integrity. This approach facilitates robust decision-making with confidence levels of 90%, 95%, and 99%, ensuring a comprehensive evaluation of homogeneity in time-series data (Buishand, 1982). A comprehensive homogeneity test of rainfall data for 23 stations in the Awash River Basin was conducted using the RAINBOW software, focusing on cumulative deviation metrics. The test evaluated the probability of rejecting homogeneity at 90%, 95%, and 99% significance levels. For instance, as shown in Figure 3-16, Adama station indicated no probability of rejecting homogeneity at any of these significance levels. Similarly, none of the 23 stations demonstrated rejection at the 90%, 95%, and 99% thresholds, confirming that the rainfall data were homogeneous and suitable for further analysis. This consistency across stations supports the reliability of the dataset for subsequent modeling and decision-making.

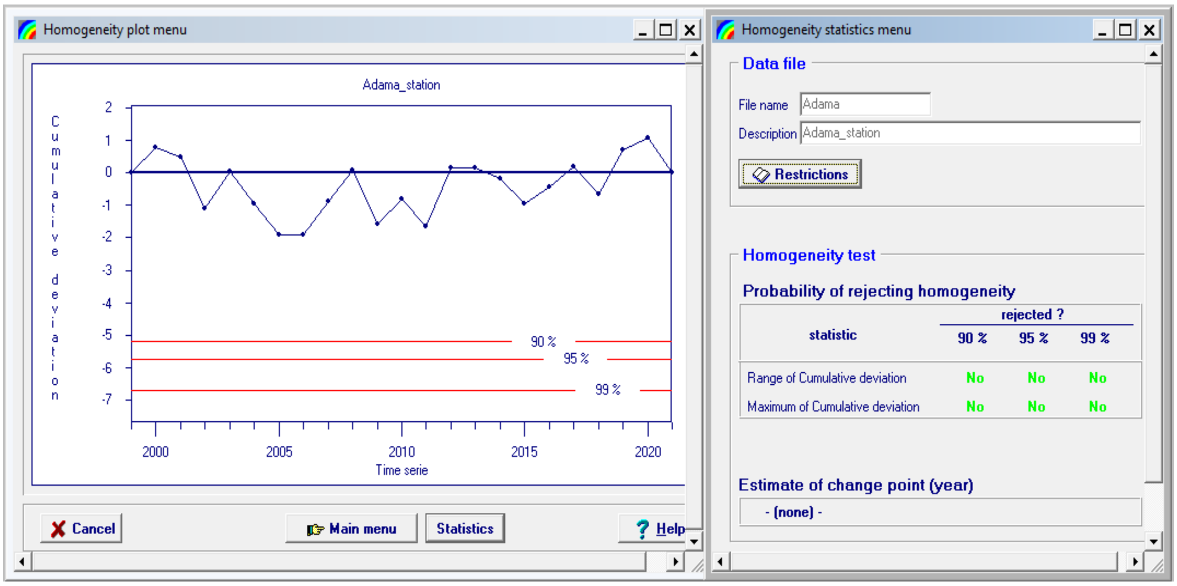

Figure 3-16 Homogeneity test using rainbow software for Adama station

3.4.2. Standardized Precipitation Index (SPI)

The SPI was first introduced by McKee et al., (1993)at Colorado State University and has since become the most widely used index for meteorological drought monitoring. Its popularity stems from its simplicity, as it requires only precipitation data, and its ability to describe droughts across various spatial and temporal scales. The SPI is calculated using the formula:

$$SPI \ \frac{X_i - X_m}{\sigma}$$

Where:

X_i is the value of precipitation at i_{th} month or season and year,

X_m is the mean monthly, seasonal, or annual precipitation, and

σ is the standard deviation of recorded precipitation.

The SPI is widely recognized as a robust tool for monitoring drought conditions due to its minimal data requirements, statistical rigor, and ease of calculation. By capturing drought over different timescales, the SPI provides a clear understanding of both short-term and long-term drought impacts. For this study, SPI3 was computed specifically to monitor meteorological drought across the basin. Meteorological drought analysis often focuses on short-term indices like SPI1, SPI3, and SPI6, which reflect the immediate effects of drought, particularly relevant for agricultural and water resource planning (Dutta et al., 2013). In contrast, longer-term indices such as SPI12 and higher are used to assess hydrological drought, especially in regions with limited hydrological data. In this analysis, SPI3 time series from July, August, and September were utilized to assess drought and wet conditions across multiple stations over a 21-year period. The classification of the SPI is according to McKee et al. (1993), holding four categories of drought condition as illustrated below Table 3-2.

Focusing on the months of July, August, and September for drought monitoring in Ethiopia is crucial due to their alignment with the *Kiremt* season. This main rainy period provides the majority of the annual rainfall essential for agriculture and water resources. The *Kiremt* season significantly influences crop yields and water availability, which are vital for food security and livelihoods in the region. Any rainfall deficits during this period can trigger agricultural droughts, leading to substantial impacts on food production and rural communities. Thus, monitoring these months helps identify potential drought risks and supports timely interventions to mitigate adverse effects, safeguarding both agricultural productivity and water resource management.

Table 3-2 Classification of drought severity based on SPI3 values

Category	**SPI3 Value Range**
Mild Drought	0 to −0.99
Moderate Drought	−1.00 to −1.49
Severe Drought	−1.50 to −1.99
Extreme Drought	< −2.0

For this analysis, R Studio was used to calculate the SPI values. R Studio, with its powerful data analysis libraries and statistical functions, provided an efficient platform for performing the SPI computation. The integration of precipitation data and the calculation of SPI using R allowed for a more streamlined approach to analyzing drought trends across different time periods and locations. The code used to calculate SPI3 in R Studio is provided below in Figure 3-15.

```
# Install and load necessary packages
library(SPEI)
library(dplyr)
library(tidyr)
library(readr)
library(stringr)
# Define a function to read and prepare data from one CSV file
read_and_prepare_data <- function(file_path) {
  data <- read_csv(file_path, show_col_types = FALSE)
  data <- data %>%
    pivot_longer(cols = -Year, names_to = "Month", values_to = "Precipitation") %>%
    mutate(
      # Retain Month as character without converting to number
      Date = as.Date(paste(Year, Month, "01", sep = "-"), format = "%Y-%b-%d")  # %b
for abbreviated month names
```

```
    ) %>%
    arrange(Date)
  return(data)
}
# List all CSV files
file_paths <- list.files("C:/Users/WRE LAB/Documents/Filled-rainfall-data/CSV",
pattern = "*.csv", full.names = TRUE)
combined_data <- bind_rows(data_list, .id = "Site")
combined_data$Site <- as.character(combined_data$Site)
calculate_spi3 <- function(data) {
  spi_values <- spi(data$Precipitation, scale = 3)$fitted
  return(spi_values)
}
spi_data <- combined_data %>%
  group_by(Site) %>%
  arrange(Date) %>%
  mutate(
    SPI_3 = calculate_spi3(cur_data())  # Calculate SPI for 3 months
  ) %>%
  ungroup()
save_spi_results <- function(data, file_path) {
  site_name <- str_remove(basename(file_path), "\\.xlsx$")
  output_file <- file.path("C:/Users/WRE LAB/Documents/Filled-rainfall-
data/SPI_output", paste0(site_name, ".csv"))
    print(paste("Saving to:", output_file))
  tryCatch({
    write_csv(data, output_file)
    print(paste("Successfully saved to:", output_file))
  }, error = function(e) {
    print(paste("Error saving file:", e))
  })
}
file_names <- basename(file_paths)
```

```
spi_split <- split(spi_data, spi_data$Site)
for (i in seq_along(file_names)) {
  save_spi_results(spi_split[[as.character(i)]], file_paths[[i]])
}
```

Figure 3-17 Code used to calculate SPI3 in R Studio

3.5. Methodology Flow Chart

The complete code for the study component, developed in JavaScript, is available at Google Earth Engine API.

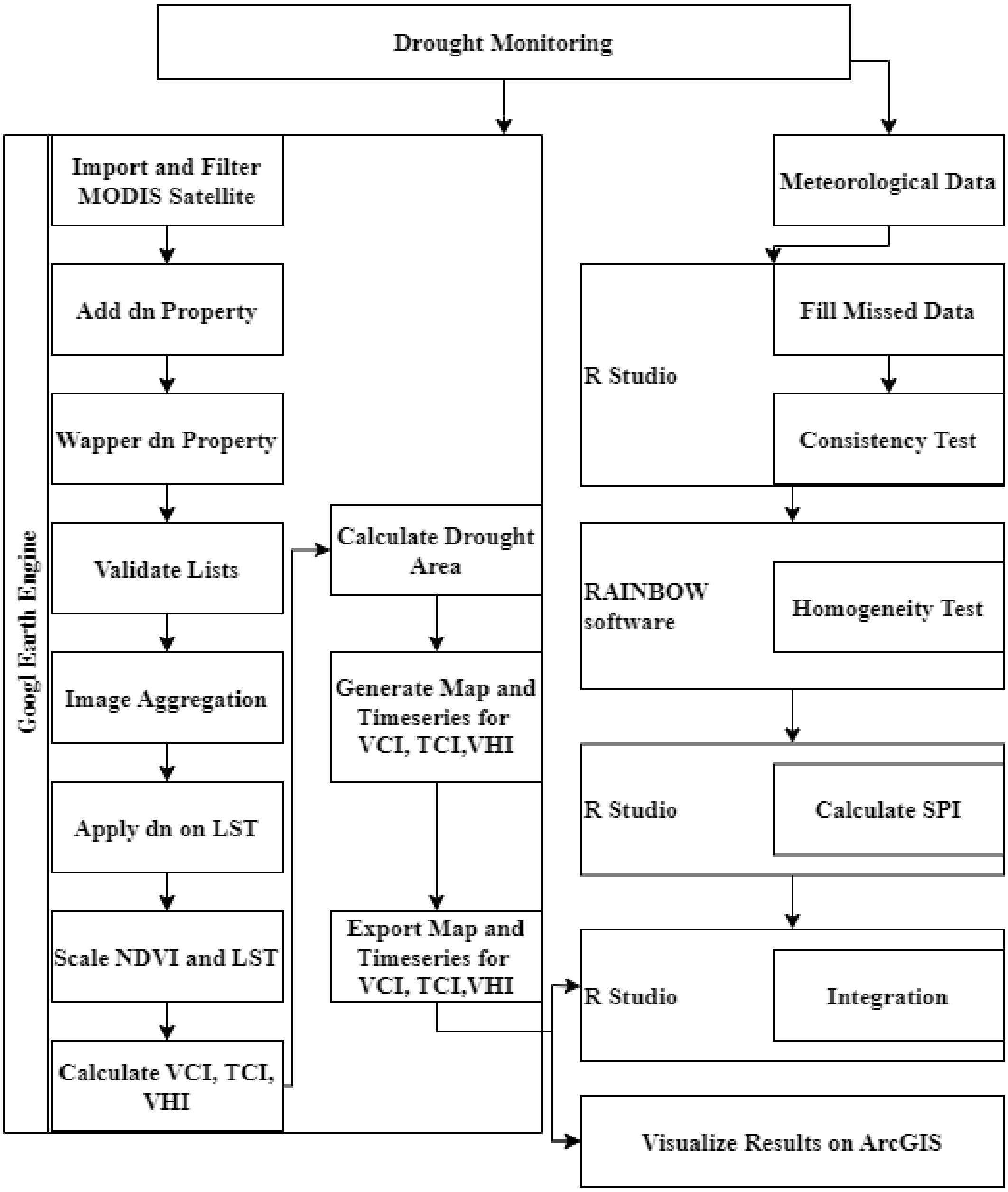

Figure 3-18 Methodology flow chart

3.6. Integration of In-Situ and Remote Sensing Data for Enhanced Drought Monitoring

Integrating in-situ data with remote sensing provides a powerful approach for monitoring drought conditions. By overlaying satellite-derived indices with spatially aligned in-situ data points, we can effectively analyze their relationships. R Studio is an essential tool for conducting the statistical analyses necessary to ensure these datasets are aligned both temporally and spatially.

In this study, we employ Pearson correlation analysis in R Studio to quantify the linear relationship between in-situ observations such as the SPI and satellite-derived indices like VCI, TCI, and VHI. A strong positive Pearson correlation indicates that satellite data accurately reflects ground conditions, enhancing confidence in the use of remote sensing for drought monitoring.

The Pearson correlation coefficient measures both the strength and direction of the linear relationship between the two datasets. Using the *cor()* function in R Studio, we calculate this correlation: a value close to +1 signifies a strong positive relationship, while a value near 0 suggests a weak or nonexistent correlation. Details on calculating Pearson correlation in R Studio can be found in Appendix B.4.

4. RESULT AND DISCUSSIONS

4.1. Drought Analysis Using Vegetation Condition Index (VCI)

The VCI has been widely recognized as a robust tool for detecting drought conditions and monitoring their temporal characteristics, such as onset, intensity, duration, and spatial dynamics, while also assessing their impacts on vegetation health (Kogan, 1995). Due to its reliance on satellite-derived data, VCI effectively captures vegetation stress caused by drought and provides an insightful measure for agricultural drought monitoring. Numerous studies have supported its application in this context (Bento et al., 2020; Kogan, 1995), highlighting its ability to discern variations in drought severity over time and space.

Research by Wu et al. (2013) emphasized the VCI’s effectiveness in distinguishing drought patterns across diverse climatic zones, demonstrating its adaptability and reliability as an indicator. Similarly, studies conducted in arid and semi-arid regions (e.g., Bhuiyan et al., 2006; Rhee et al., 2010) underscored the VCI’s capability to provide early warning signs of drought and track its evolution, which is critical for timely agricultural response and policy-making.

The analysis presented in this study used VCI to evaluate the drought severity and its spatial distribution across the region from 2000 to 2021 (Figure 4-1 and Figure 4-2). This 22-year period allowed for a comprehensive assessment of both short-term and long-term drought patterns, contributing to a better understanding of the region's vulnerability to agricultural drought. This extended timeframe provided insight into recurrent drought cycles and facilitated the identification of trends that may inform future drought preparedness strategies.

Since June typically marks the dry season for most of the study area, the analysis concentrated on the following three consecutive months, from July to September, when the agricultural growing season is most affected by water stress. This approach allowed for a more focused examination of VCI dynamics and its relevance in identifying and tracking agricultural droughts. The use of satellite-derived VCI during this critical period provided valuable data to understand how water stress impacted vegetation health, crop yields, and overall agricultural productivity.

As illustrated below in Figure 4-1, the VCI maps from 2000 to 2010 demonstrate spatial variations in drought conditions across the study area. The time series map of VCI indicates that the basin experienced mild droughts in 2000, 2001, 2006, 2007, and 2010 in the middle to lower part of the basin. Conversely, in the years 2002, 2004, 2008, and 2009, the area experienced moderate drought conditions. The spatial distribution of VCI during these years also revealed that certain sub-regions were consistently more prone to severe conditions, highlighting areas of concern for targeted interventions. This comprehensive analysis contributes to improved understanding and monitoring of agricultural droughts, supporting better decision-making for sustainable water resource management and agricultural practices.

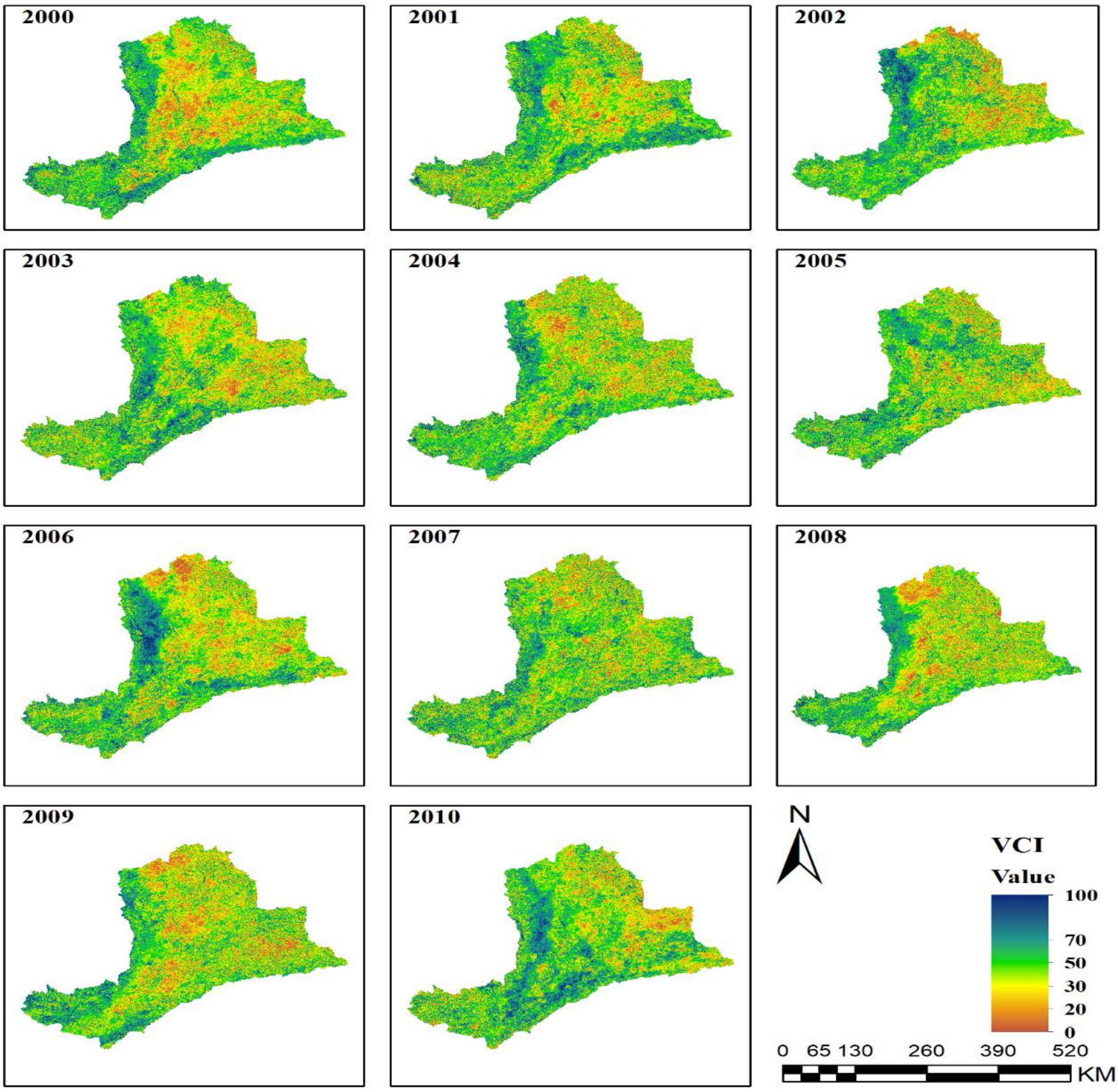

Figure 4-1 Spatio-temporal patterns of mean VCI of the main growing seasons over the study area from 2000 to 2010.

Figure 4-2 shows the VCI maps for the period from 2011 to 2021, illustrating similar spatial variations in drought conditions. The time series map of VCI indicates that the basin experienced mild droughts in 2013, 2020, and 2021 in the middle to lower part of the basin.

In contrast, in the years 2011, 2014, 2015, 2017, and 2018, the area experienced moderate drought conditions. The analysis highlights the fluctuations in drought conditions over the decades and emphasizes the importance of continuous monitoring to identify vulnerable areas and guide mitigation efforts.

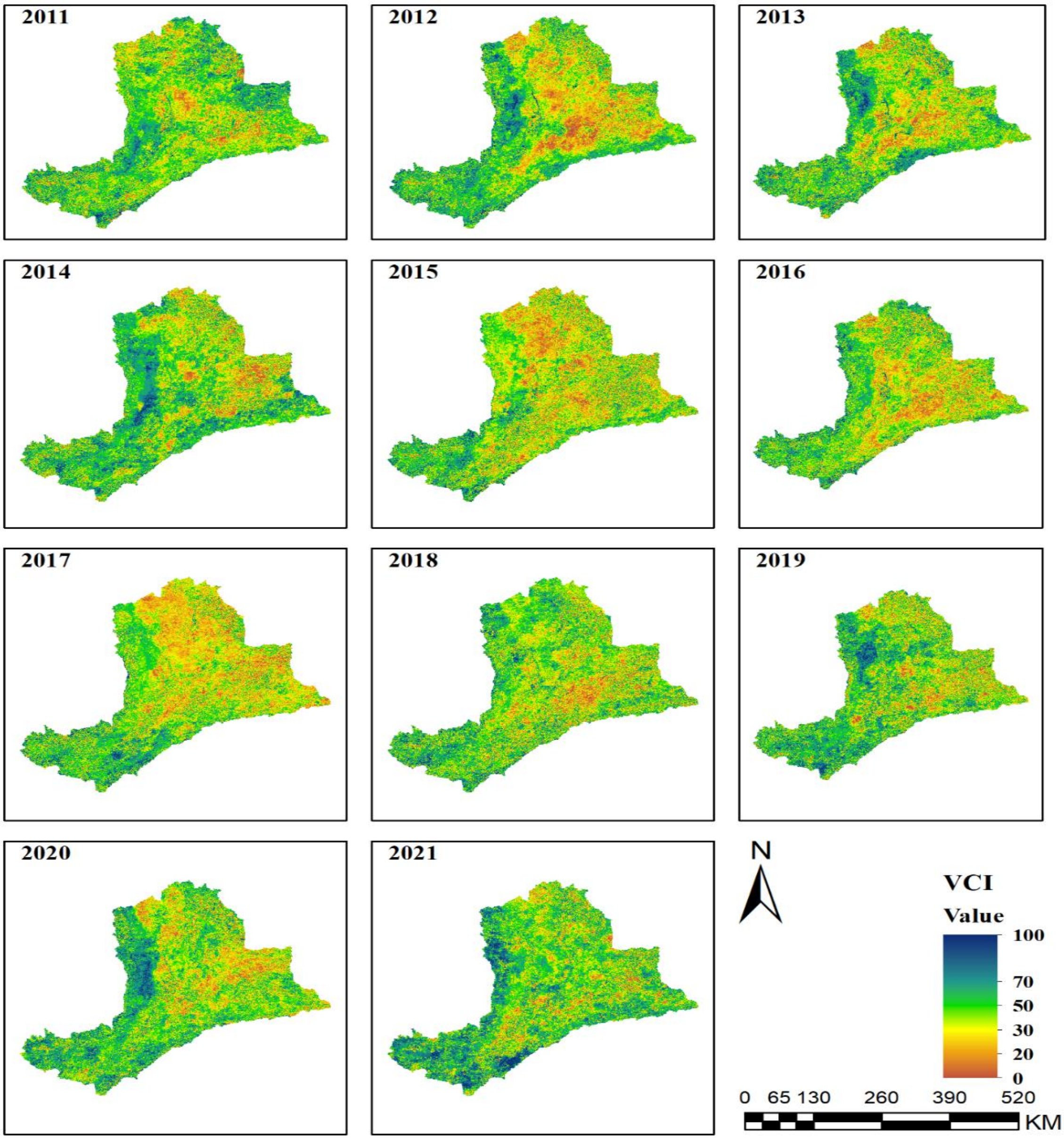

Figure 4-2 Spatio-temporal patterns of mean VCI of the main growing seasons over the study area from 2011 to 2021.

This result is consistent with Ethiopia's major historical drought events. For instance, a study by Meskelu et al., (2024) in Awash River Basin, Ethiopia, employed and the research found that moderate to extreme hydrometeorological droughts occurred approximately every six to eight years, with significant drought events recorded in 2002, 2004, 2015, and 2017. These findings underscore the importance of continuous monitoring and analysis of drought patterns to inform effective water resource management and agricultural practices.

4.1.1. Drought areas across various severity levels of VCI

In the analysis of drought areas across various severity levels from 2000 to 2021 in Figure 4-3, the VCI Mild Drought (represented by orange) predominates in the majority of the drought-affected area throughout the years. This category consistently comprises over 50% of the area in numerous years, with the highest occurrences in 2001, 2010, 2011, and 2021, where the affected area exceeds 70%. Mild drought represents the most persistent drought condition throughout the period, exhibiting peaks in these aforementioned years.

The VCI Moderate Drought represents a significant portion of the drought-affected area, typically ranging between 30% and 50%. Years with a particularly high percentage of moderate drought are 2008, 2009, and 2016, where it reaches its highest levels, slightly above 50%. This category shows consistent stability across the years, reflecting that moderate drought is a recurring condition affecting substantial areas annually.

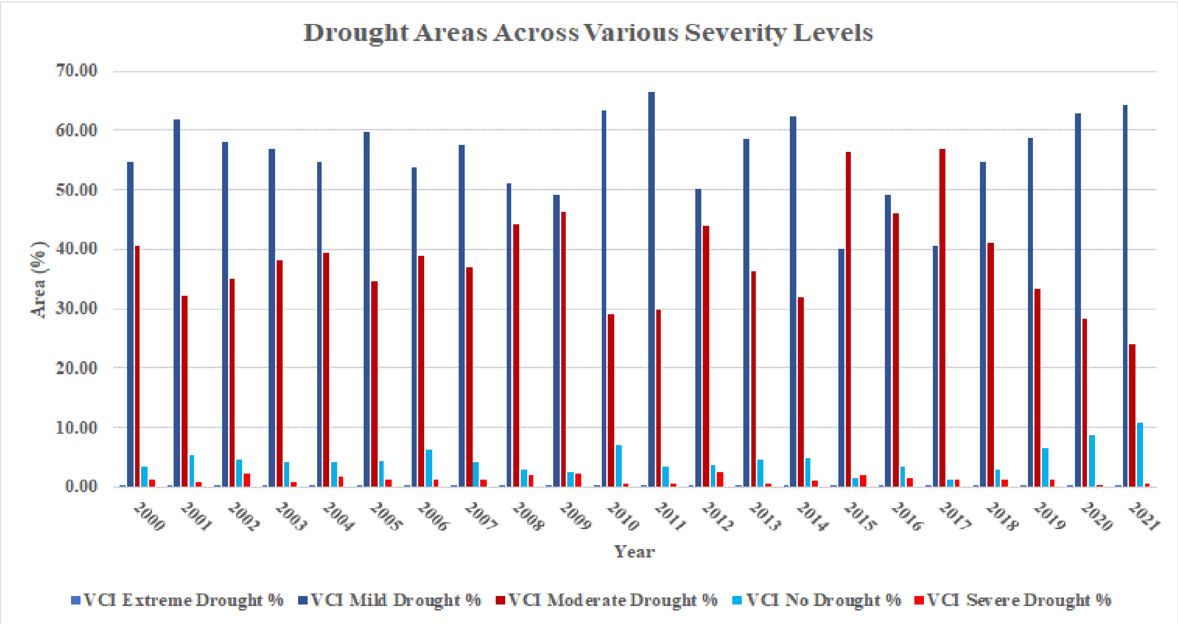

Figure 4-3 Drought areas across various severity levels of VCI from 2000 to 2021

The VCI No Drought category indicates the percentage of areas free from drought. These percentages are significantly lower compared to the drought-affected areas, generally staying below 20%. However, 2010 and 2011 show a slight increase in no drought areas, with the percentage climbing to around 10% to 20%. This indicates better conditions in these years, with more areas escaping drought compared to other years.

The VCI Severe Drought category accounts for a very small percentage across all years, generally staying below 5%. Years like 2009, 2012, and 2015 saw slightly higher occurrences of severe drought, with the affected areas reaching closer to 5%. However, severe drought remains a less frequent and less impactful category over the period.

Similarly, the VCI Extreme Drought shows the smallest percentage across the years, often close to zero, indicating that extreme drought conditions are rare. The highest occurrences of extreme drought were observed in 2002, 2008, and 2009, where the percentage slightly exceeded 1%. However, extreme drought conditions are rare and localized, contributing minimally to the overall drought-affected areas. Mild and moderate droughts are the most common drought conditions, affecting large portions of the area consistently throughout the years. Severe and extreme droughts are relatively rare, contributing only small percentages of the affected areas. Although there are slight increases in the No Drought category during certain years, particularly in 2010 and 2011, drought conditions remain widespread, with mild and moderate droughts being dominant across the period. All the area percentages under different severity levels for all the years are attached in Appendix B.1.

4.1.2. Trend of Mean Annual VCI from 2000 to 2021

The trend of the mean annual from 2000 to 2021, as illustrated in Figure 4-4, reveals notable fluctuations, reflecting the variability of vegetation health and environmental conditions over the period. The VCI, as an indicator of vegetation health, shows no consistent long-term upward or downward trend, suggesting that the vegetation's response to climatic factors has been dynamic. From 2000 to 2002, there is a clear dip, with the VCI starting moderately in 2000 (55.771), peaking in 2001 (61.7183), and sharply declining in 2002 (41.56). This drop may be associated with stress factors like drought or temperature extremes. Following this, a gradual recovery is observed between 2003 and 2005, with the VCI peaking again in 2007 (64.276), likely reflecting favorable climatic conditions that supported healthier vegetation.

The period from 2006 to 2010 is marked by moderate VCI values, fluctuating between 37.848 and 56.996, indicating some stability but with persistent environmental stresses affecting vegetation health. The slight improvement towards 2010 (56.9963) suggests potential recovery. Between 2011 and 2017, alternating peaks and troughs in the VCI reflect the dynamic nature of climatic conditions during this period, with vegetation health fluctuating in response to changing rainfall and temperature patterns. A particularly low point is observed in 2015 (39.7868), followed by a recovery in 2016 (50.662).

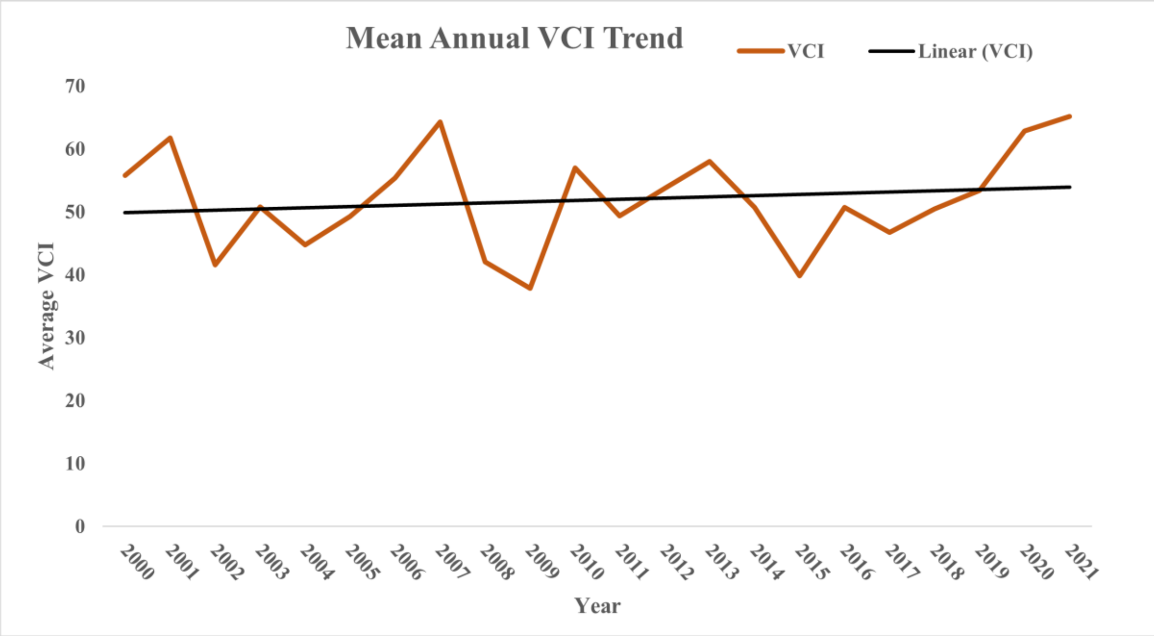

Figure 4-4 Trend of mean annual VCI in the study area from 2000 to 2021.

In the later years, from 2018 to 2021, the VCI stabilizes around moderate values, though 2020 stands out with a higher VCI average (62.885), signaling good vegetation health, likely due to favorable environmental conditions. The trend continues with a slight improvement in 2021 (65.1877), indicating healthier vegetation by the end of the period. Overall, while short-term fluctuations in vegetation health are evident, no significant long-term trend is observed, underscoring the variability in environmental conditions that influence vegetation. This variability highlights the sensitivity of vegetation to climatic changes, with peaks corresponding to favorable conditions and troughs indicating periods of stress. The absence of a clear long-term trend suggests the need for continued monitoring and adaptive strategies to mitigate the impacts of climate variability on vegetation health.

4.1.3. Drought Frequency Using VCI

The VCI analysis for the months of July, August, and September (Figure 4-5) revealed significant variations in drought frequency and intensity. In July, there were 22 drought events, with the majority categorized as moderate and severe. The month recorded 14 moderate and 7 severe drought events, indicating substantial drought stress during this period, with no instances of "No Drought" conditions, suggesting persistent drought throughout the month. Conversely, August experienced a total of 22 drought events as well;

however, the majority were classified as mild. The month recorded 12 mild and 2 moderate drought occurrences, along with 8 instances of "No Drought" conditions, indicating a reduction in drought intensity compared to July.

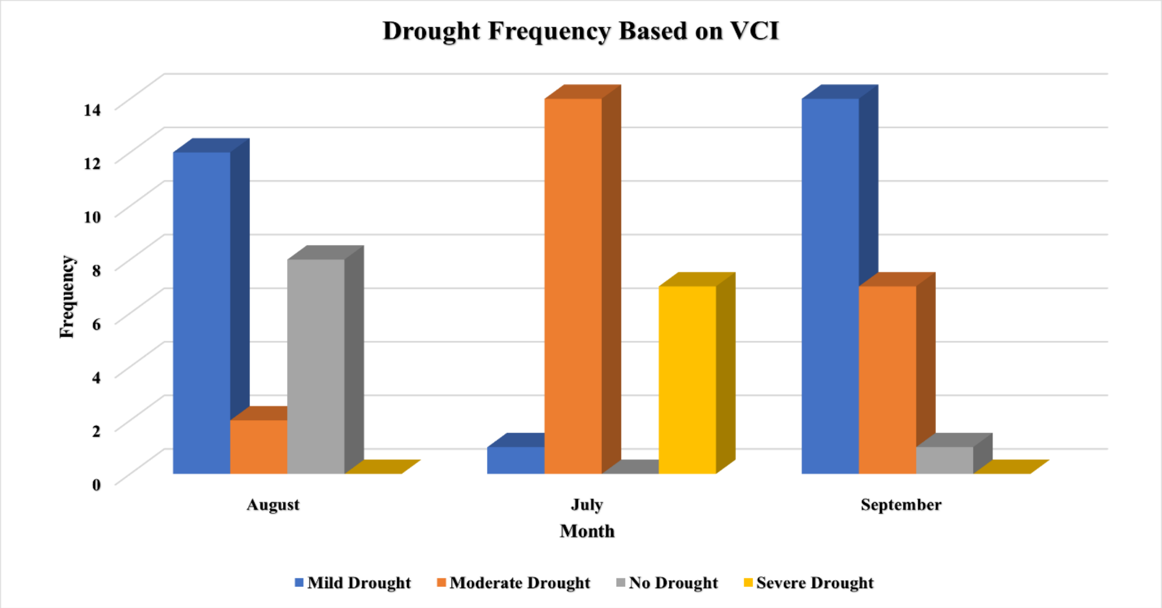

Figure 4-5 Frequency of drought based on VCI

September exhibited a total of 22 drought events, the highest among the analyzed months. However, the majority of these were classified as mild drought, with 14 mild and 7 moderate drought occurrences, and only one instance of "No Drought." This observation indicates that, while September had the highest frequency of drought occurrences, they were generally less severe than those in July. July emerged as the most significantly drought-affected month, with the highest frequency of severe drought events. Conversely, September demonstrated the largest number of mild drought occurrences, suggesting that drought conditions were more intense earlier in the period and became less severe towards the conclusion.

4.2. Drought Analysis Using Temperature Condition Index (TCI)

The TCI analyzes drought conditions by reflecting temperature-induced stress on vegetation, which is a critical factor in determining drought severity. Higher TCI values indicate favorable temperature conditions, while lower values correspond to increased temperature stress and potential drought. The TCI maps in Figure 4-6 and Figure 4-7 from 2000 to 2021 illustrate the temporal and spatial variations in drought intensity across the region.

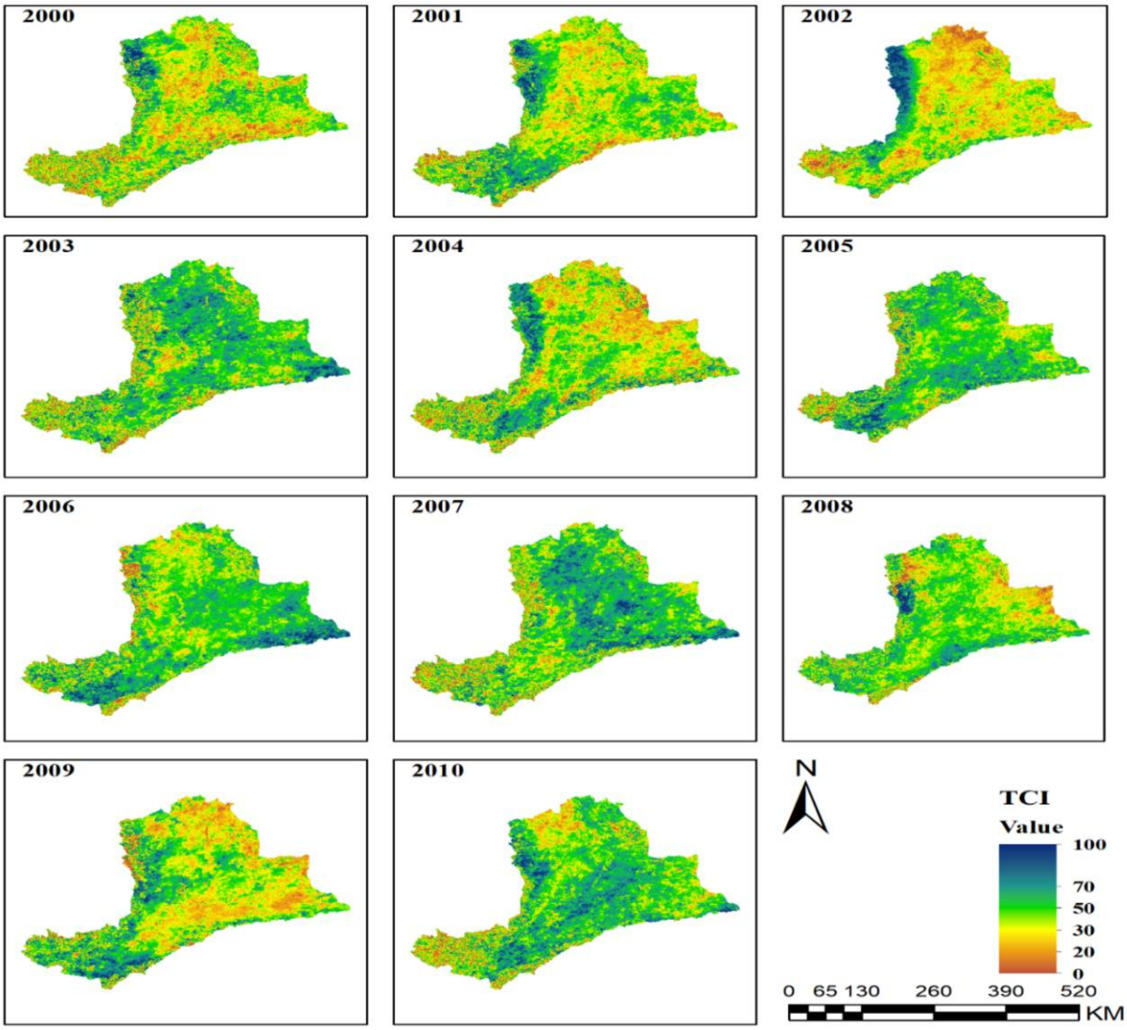

Figure 4-6 Spatio-temporal patterns of mean TCI of the main growing seasons over the study area from 2000 to 2010.

In 2000, the region predominantly experienced no drought conditions, as evidenced by widespread green and blue areas, with only isolated patches exhibiting mild or moderate drought. This favorable condition persisted in 2001, although some localized areas exhibited indications of mild drought in certain northern regions. By 2002, the maps demonstrated a significant increase in drought severity, with substantial portions of the region experiencing moderate to severe drought conditions, particularly in the northern areas. The drought conditions further intensified in 2003, with regions of extreme drought emerging, as evidenced by maps.

The year 2004 marked a recovery, with much of the region returning to no drought and mild drought categories, although moderate and severe drought persisted in localized areas. Between 2005 and 2008, drought severity fluctuated. In 2005, the region experienced mainly no drought or mild drought conditions, while 2007 and 2008 saw a rise in temperature stress, with several areas falling into severe and extreme drought categories. A significant increase in temperature-related drought occurred in 2009, with large parts of the region experiencing moderate to severe drought, and even some areas entering extreme drought. However, 2010 saw a substantial recovery, with most of the region falling back into the no drought and mild drought categories (Figure 4-6).

Figure 4-7 in next page, in contrast to the recovery observed in 2010, 2011 was characterized by severe drought conditions, with widespread moderate, severe, and extreme drought categories predominating the map. The region experienced alternating patterns in 2012 and 2013, with 2012 exhibiting more favorable conditions (predominantly no drought and mild drought), while 2013 demonstrated a return to moderate and severe drought. The year 2014 was notable for its extensive severe and extreme drought, affecting substantial portions of the region. This pattern persisted through 2015 and 2016, although 2016 exhibited some recovery with fewer areas experiencing extreme drought.

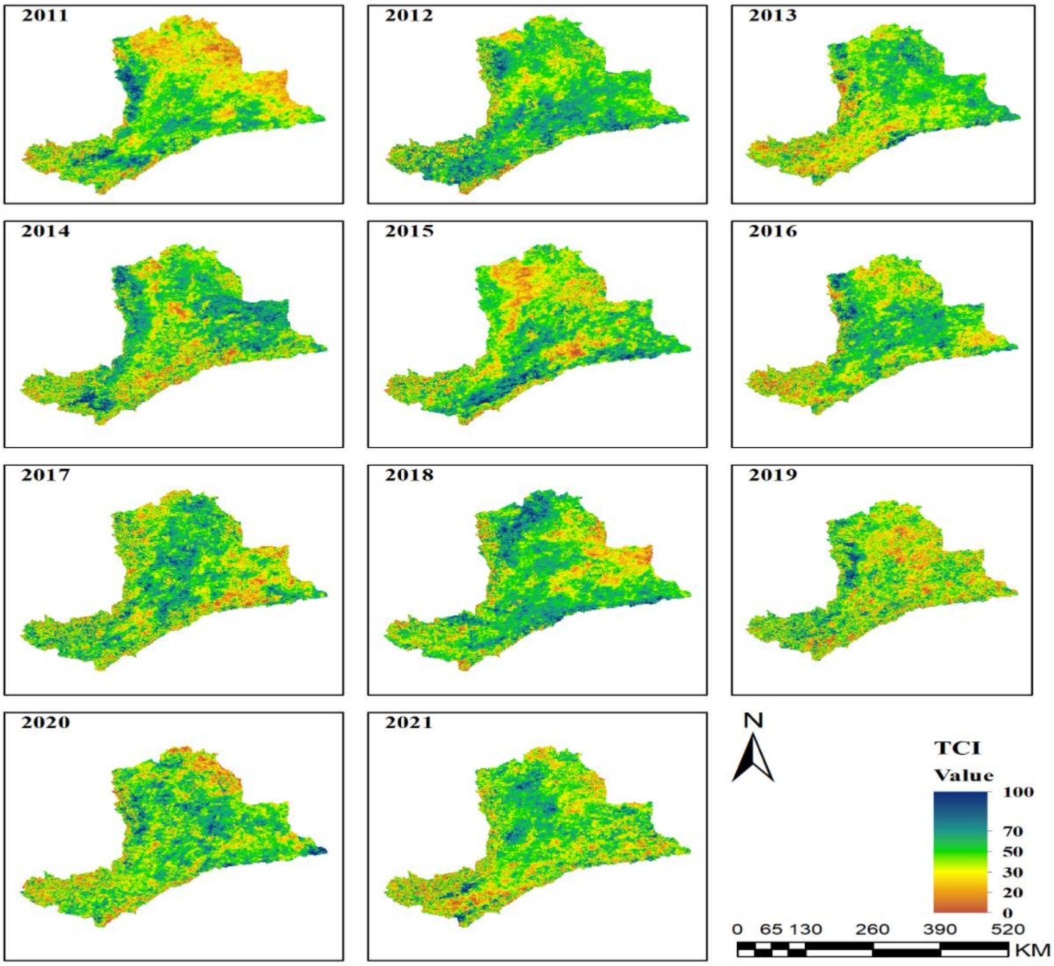

Figure 4-7 Spatio-temporal patterns of mean TCI of the main growing seasons over the study area from 2011 to 2021.

Drought conditions intensified in 2017 and 2018, with substantial areas under severe and extreme drought, particularly in 2017. In 2019, the region observed some improvement, characterized by a reduction in severe drought and an increase in areas categorized as mild or moderate drought. However, this trend was not sustained, as 2020 and 2021 demonstrated a return to widespread moderate to severe drought, with some areas progressing to extreme drought. The spatial variation in drought categories across these years reveals that the northern and central regions are more prone to severe and extreme drought conditions, while the southern parts of the region generally experience less drought, often falling into the no drought or mild drought categories.

4.2.1. Drought areas across various severity levels of TCI

The graph in Figure 4-8 depicting drought areas across various severity levels of the from 2000 to 2021 highlights notable trends. Throughout the period, mild drought conditions dominate, consistently covering the largest percentage of the area. Particularly in years such as 2006, 2012, and 2018, mild drought affects more than 70% of the land, indicating frequent mild drought episodes with potentially significant impacts on agriculture and water resources. Moderate drought, while fluctuating over the years, also occupies a substantial portion of the area, especially in years like 2009, 2013, and 2017, pointing to worsening drought conditions during those periods.

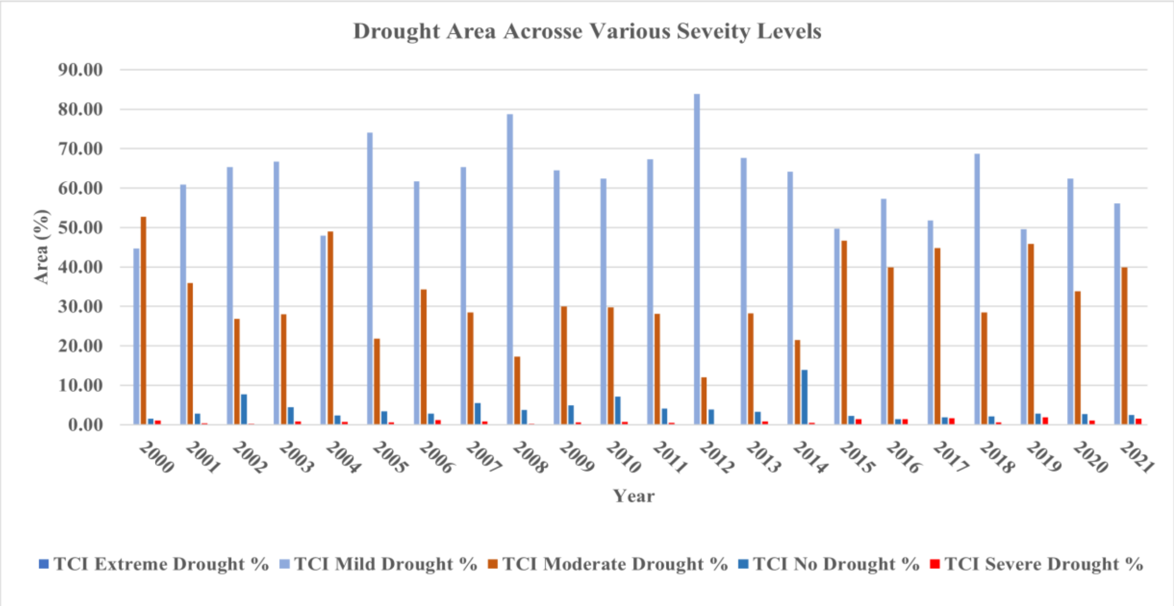

Figure 4-8 Drought areas across various severity levels of TCI from 2000 to 2021

On the other hand, the proportion of the area experiencing no drought remains relatively low, rarely surpassing 20%, with year like 2014 showing slightly higher percentages of no drought conditions. Extreme and severe droughts, although less prevalent, show notable spikes in certain years, such as 2000, 2010, and 2012, where extreme drought covers more than 5% of the area. These extreme conditions, while infrequent, would have severe impacts on vegetation and water availability. The variability in drought severity across the years reflects the region's dynamic climatic conditions, likely influenced by factors such as El Niño, which could exacerbate drought in some years. In recent years (2019-2021), there appears to be a decline in the percentage of areas experiencing mild and moderate drought, suggesting a potential improvement in climatic conditions, although mild drought remains a dominant feature.

4.2.2. Trend of Mean Annual TCI from 2000 to 2021

Figure 4-9 shows the mean annual TCI trend from 2000 to 2021 with a linear trendline. The TCI fluctuates over the two decades, with periods of increase and decrease. Starting from a high value in 2000, the TCI declines notably in the early 2000s, reaching a low around 2002, indicating severe temperature-related drought conditions.

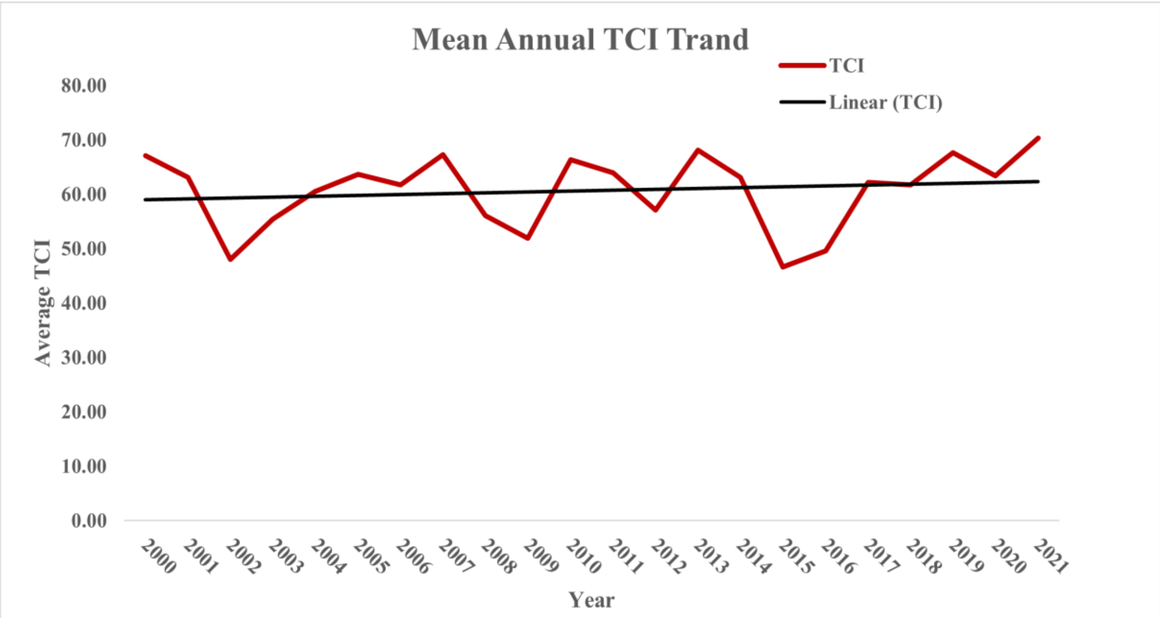

Figure 4-9 Trend of mean annual TCI from 2000 to 2021

The TCI then recovers, rising through the mid-2000s, particularly between 2005 and 2008, before another drop occurs around 2010. After 2011, a gradual upward trend is observed, peaking in 2020 and 2021. The linear trendline suggests an overall increase in TCI, pointing to improved temperature-related drought conditions over time. This consistent rise in later years may reflect better climatic conditions or adaptive measures. The sustained upward trend in recent years aligns with reported regional climate improvements. Continued monitoring is essential to understand the factors contributing to these changes. In summary, the analysis from 2000 to 2021 highlights fluctuations but indicates an overall positive trend in temperature stress conditions in the region.

4.2.3. Frequency of Drought Based on TCI

Figure 4-10 shows the drought frequency of a three-month period consisting of July, August, and September using the TCI classification. This will be helpful in understanding the distribution of drought conditions within those months for the period under analysis.

In July, the majority of the cases fall into the No Drought category, with 16 cases. This is relatively good regarding temperature in this month. On the second thought, July is also the month that sees a high rate of occurrence of severe drought conditions at 7 occurrences. Compared to Severe Drought conditions, Mild Drought cases are only 5 in number. There is only 1 occurrence of Moderate Drought in July.

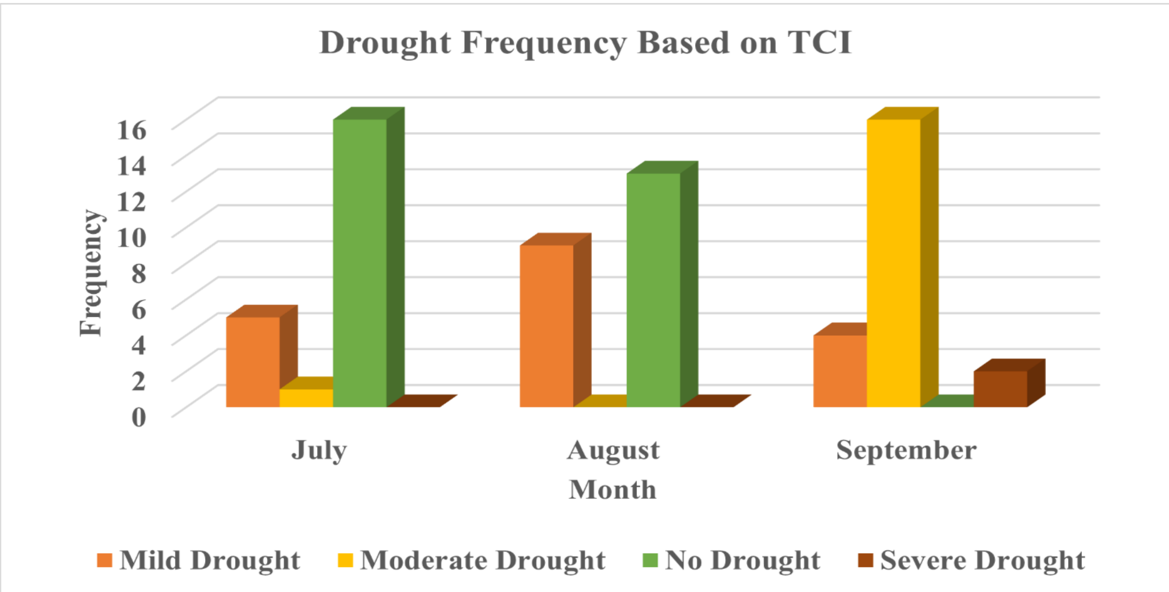

Figure 4-10 Frequency of drought based on TCI

In contrast, August has an almost normal spread in between No Drought and Mild Drought categories, with 13 and 9 occurrences, respectively. That would thereby indicate a combination of both favorable and mild drought conditions in August indeed but does not record any severities. There is also an evident lack of Moderate Drought in this month, which can again reveal that August usually exhibits either mild or no drought conditions.

This is the month of September, which has recorded the highest frequency of Moderate Drought, numbering 16. This shows that during this period, temperature conditions are highly recorded as moderately drought. In addition, it has recorded 4 cases of Mild Drought and 2 cases of Severe Drought during September. The few occurrences of No Drought (0 cases) portray that September experiences worse temperature conditions compared to the rest of the months. In general, the data provides remarks on variability in the drought conditions of the three-month period. July has a wider range of drought conditions, from no drought to severe drought. August is more favorable, with most instances in the mild or no drought categorizations. In contrast, September indicates a higher frequency of moderate droughts—meaning that this month experiences more challenging temperature-related drought conditions.

4.3. Drought Analysis Using Vegetation Health Index (VHI)

The VHI analysis from 2000 to 2010 indicates in Figure 4-11 significant spatial and temporal variability in drought severity across the region.

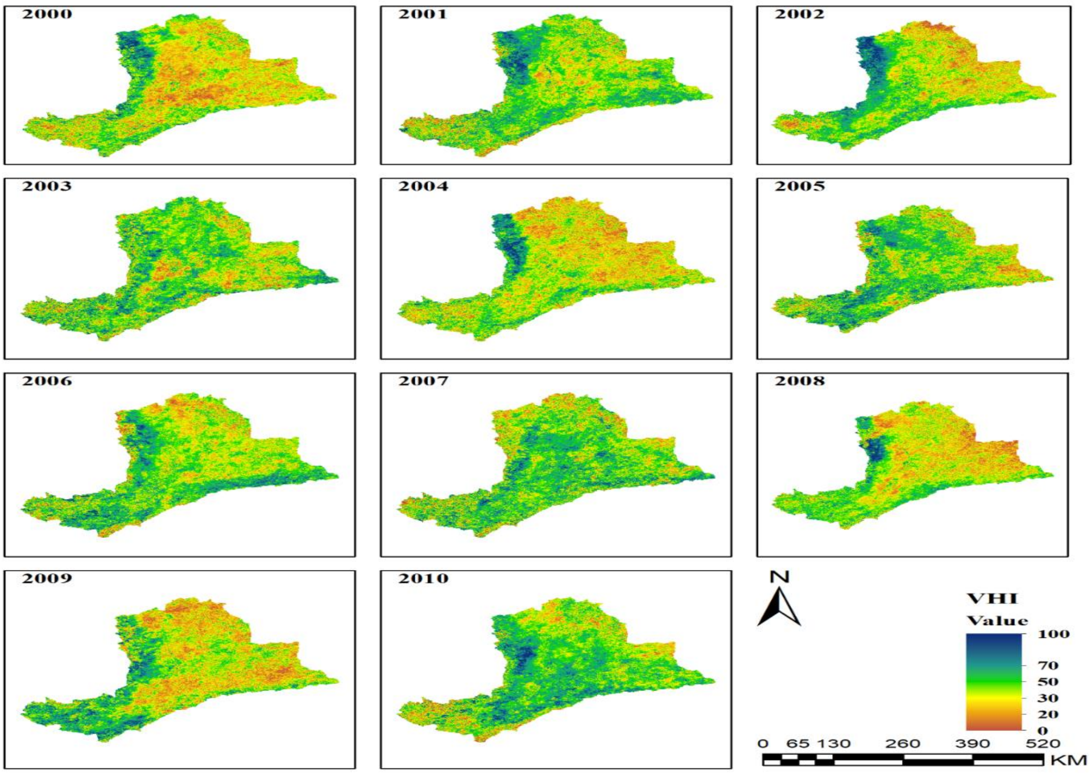

Figure 4-11 Spatio-temporal patterns of mean VHI of the main growing seasons over the study area from 2000 to 2010

From 2000 to 2004, the maps reveal mild to moderate drought conditions, with more severe instances observed particularly in the northeast and central areas during 2002 and 2003. The year 2002 stands out for experiencing extreme drought conditions predominantly in the northeast, while 2003 continued this trend with noticeable drought in central areas.

In 2005, severe drought affected the southern and central regions, signaling a shift in drought patterns. The following year, 2006, marked some recovery, as the western part of the region exhibited areas with no drought, demonstrating a brief period of healthy vegetation. However, this recovery was short-lived as severe drought returned in 2007 and 2008, with the southern regions being notably affected. By 2009, the situation escalated further, with extreme drought spreading across the southern and eastern parts of the region. The year 2010 depicted a mixed scenario, showcasing healthier vegetation conditions in the western and northern regions. Despite this, drought persisted in some central and southern areas, indicating a fluctuation between recovery and stress during this period.

From 2011 to 2021 (Figure 4-12), the region continued to experience notable fluctuations in drought severity. In 2011, there was moderate drought affecting many parts of the region.

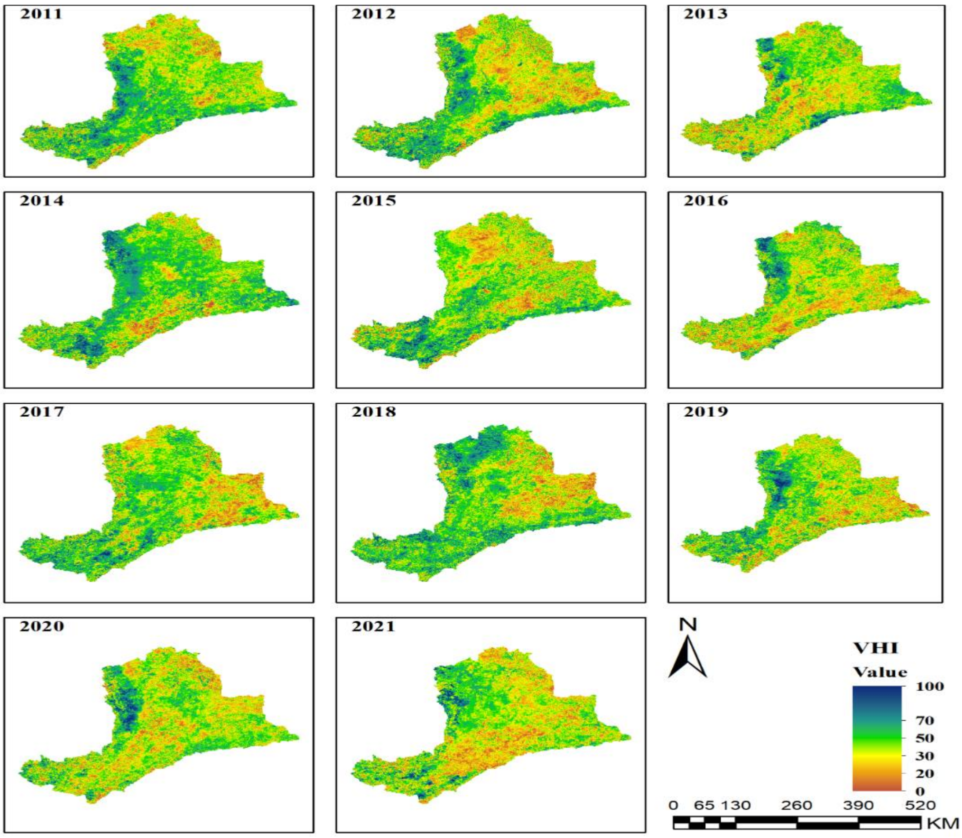

Figure 4-12 Spatio-temporal patterns of mean VHI of the main growing seasons over the study area from 2011 to 2021

The year 2012 showed some recovery with more balanced conditions, but moderate drought persisted in several areas, particularly in the south and central regions.

By 2013, the drought patterns stabilized slightly, showing a mix of mild to moderate drought conditions across the region. However, 2014 saw a return of severe drought, especially affecting the south and central areas. The situation worsened in 2015, where severe and extreme drought conditions became widespread, particularly in the southeastern part of the region. The maps for 2016 and 2018 reflected some recovery, with notable improvements in vegetation health, although pockets of moderate drought were still present.

In 2019, moderate to severe drought once again became predominant, affecting much of the central and southern regions. The year 2020 showed significant recovery, with healthier vegetation observed, particularly in the northern parts of the region. However, this positive trend was short-lived, as 2021 experienced a resurgence of severe and extreme drought, affecting central and southern areas most intensely.

Overall, the analysis highlights that the southern and central regions were consistently vulnerable to severe drought throughout the period from 2000 to 2021. The northern regions, on the other hand, demonstrated greater resilience, showing periods of recovery and healthy vegetation amidst recurring drought conditions.

4.3.1. Drought areas across various severity levels of VHI

The analysis of drought areas across various VHI severity levels from 2000 to 2021, as shown in Figure 4-13, reveals significant fluctuations in the percentage of regions affected by drought over time. Data on drought severity levels provide critical insights into the impact on vegetation during this 21-year period. Extreme drought was rare, peaking in 2017 (19.84 km^2, 0.02%) and 2018 (13.58 km^2, 0.01%). Severe droughts were more notable in 2009 (439.80 km^2, 0.37%) and 2017 (2022.99 km^2, 1.72%), indicating vegetation stress, while occurrences in 2019 and 2021 were lower at 173.81 km^2 (0.15%) and 103.04 km^2 (0.09%), respectively.

In contrast, moderate drought was common, significantly affecting the region, especially in 2009 (69,181.68 km^2, 58.74%) and 2017 (74,497.48 km^2, 63.26%). Other notable years included 2015 (53,054.87 km^2, 45.05%) and 2016 (54,942.55 km^2, 46.65%), with nearly half the region under moderate drought. Mild drought was the most prevalent condition, impacting large areas across most years, with peak effects in 2001 (89,595.86 km², 76.08%) and 2010 (87,962.84 km², 74.69%).

No drought areas showed variability, with the largest in 2010 (10,265.67 km², 8.72%) and 2021 (8,916.47 km², 7.57%). Conversely, extreme drought years like 2009, 2017, and 2018 had minimal no-drought areas, highlighting significant vegetation stress. Overall, Figure 4-10 illustrates that while extreme and severe droughts were infrequent, moderate and mild droughts were widespread, affecting large areas annually. Mild drought dominated in several years, while moderate drought varied but remained significant. Despite some years with no drought areas, drought stress was a persistent issue throughout the period.

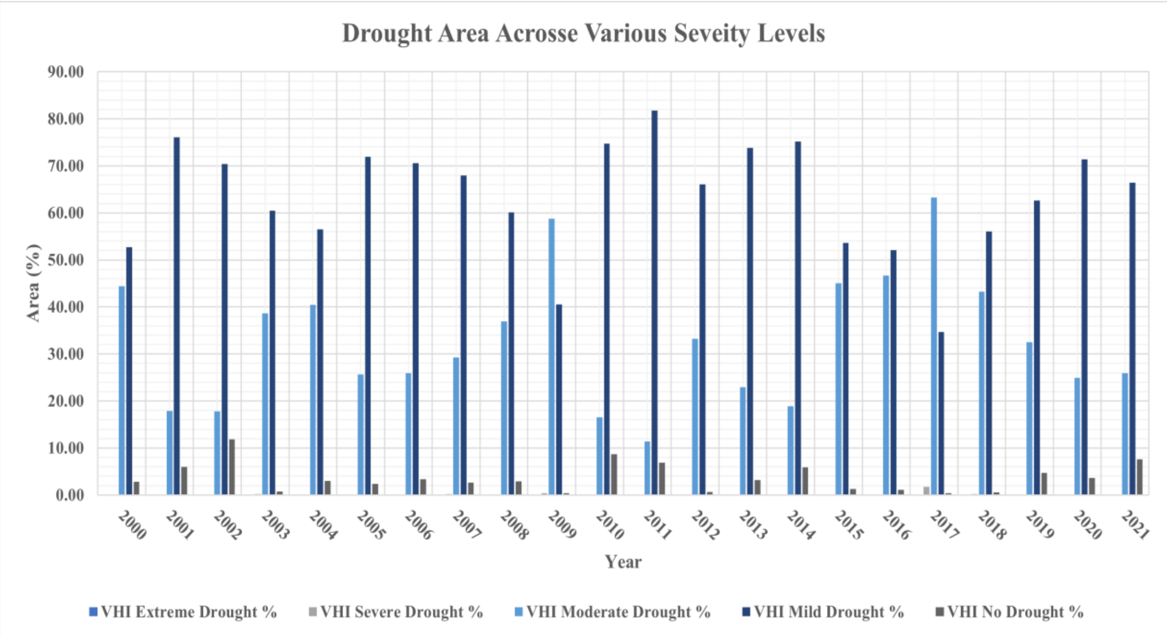

Figure 4-13 Drought areas across various severity levels of VHI from 2000 to 2021

4.3.2. Trend of Mean Annual VHI from 2000 to 2021

The analysis of the Mean Annual VHI from 2000 to 2021 shows variability in vegetation health conditions over the years (Figure 4-14). The VHI values ranged between a minimum of 43.21 in 2015 and a maximum of 68.07 in 2021. The overall trend, as indicated by the linear regression line, suggests a slight increase in VHI over the 21-year period, reflecting an overall improvement in vegetation health despite notable fluctuations. In the early years, VHI started at 61.60 in 2000 and slightly increased to 62.43 in 2001. However, there was a significant drop in 2002 to 46.31, which likely indicated severe vegetation stress. The VHI values recovered in subsequent years, reaching 58.15 in 2003 and 52.63 in 2004.

From 2005 to 2011, the VHI fluctuated between 56.47 and 61.79, with a peak in 2007 at 65.87, indicating healthier vegetation during that period. However, this was followed by a decline in 2008 and 2009, with VHI values of 51.07 and 44.87, respectively. Despite this, the VHI recovered significantly in 2010 to 61.79, but slightly declined again to 56.69 by 2011. In the later years, VHI continued to fluctuate, but there was an overall upward movement. The VHI reached 63.12 in 2013 but experienced a substantial drop to 43.21 in 2015, marking the lowest value in the dataset and indicating extreme vegetation stress. After 2015, the VHI gradually recovered, reaching 55.12 in 2016 and further improving to 60.60 by 2019. The most notable rise occurred between 2020 and 2021, where the VHI jumped from 63.29 to 68.07, the highest recorded value in the 21-year period.

While the VHI values exhibited significant variability across the years, the linear trend line indicates a mild increasing trend in the overall health of vegetation. This suggests an improvement in vegetation health over the study period, especially towards the end of the period in 2021. Despite this upward trend, the fluctuations highlight the impact of environmental factors, such as drought, which have led to both sharp declines and subsequent recoveries in vegetation health.

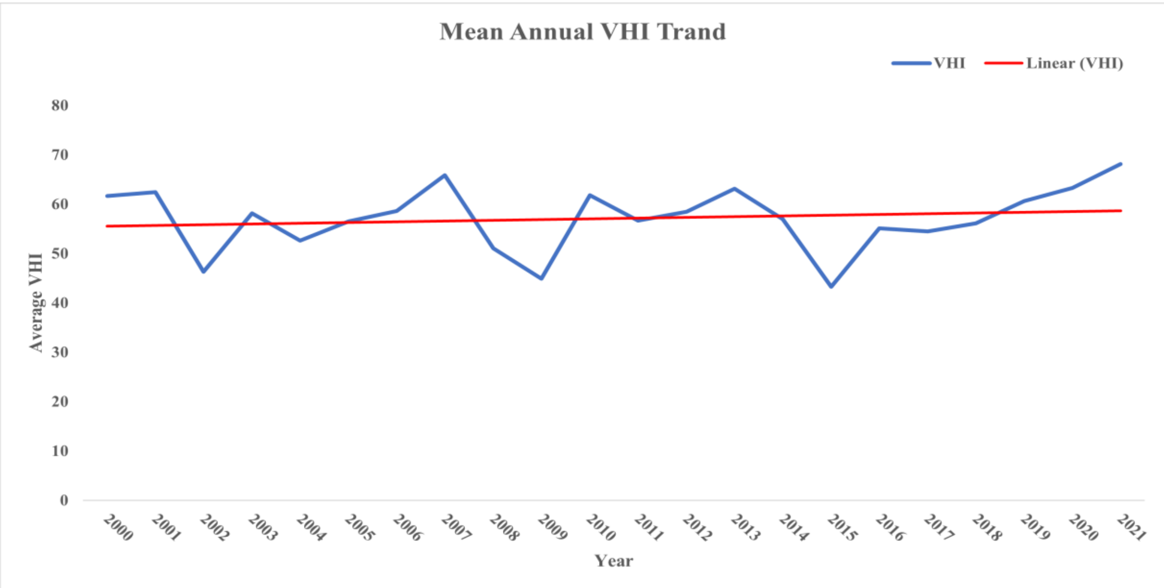

Figure 4-14 Trend of Mean Annual VHI from 2000 to 2021

4.3.3. Frequency of Drought Based on VHI

The frequency of drought conditions based on the VHI for July, August, and September shows notable variations in severity (Figure 4-15). No Extreme or Severe Droughts were recorded, indicating relatively favorable vegetation conditions. In August, Mild Drought was predominant, occurring 26 times, alongside 18 instances of No Drought. No Moderate, Severe, or Extreme Droughts were observed, suggesting mild vegetation stress.

July exhibited more variation, with Mild Drought occurring 28 times and Moderate Drought 13 times; No Drought was recorded just 3 times. As in August, there were no Severe or Extreme Droughts. September had a mix of conditions, with Mild Drought occurring 23 times and Moderate Drought 21 times, and No Drought conditions absent, indicating greater stress compared to the earlier months. Overall, Mild Drought was the most frequent condition, particularly in July and September, while the absence of Severe and Extreme Droughts suggests that drought levels remained manageable during this period.

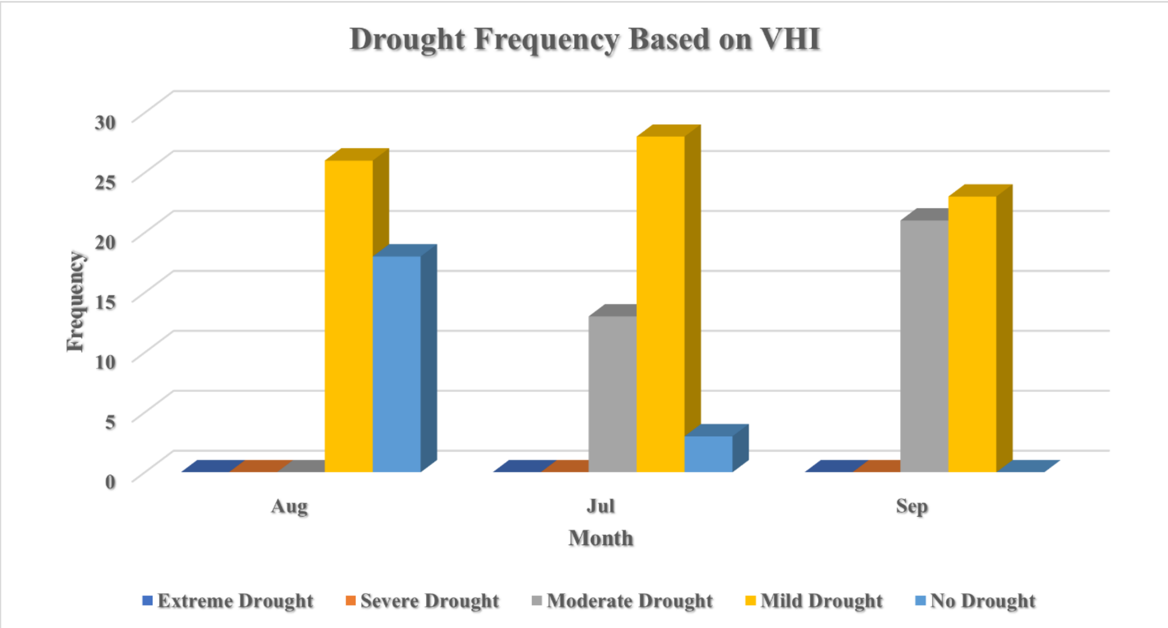

Figure 4-15 Frequency of drought based on VHI

4.4. In-situ Based Drought Monitoring

4.4.1. Drought Analysis Using the Standardized Precipitation Index (SPI)

The SPI3 data from various stations in the Awash River Basin between 2000 and 2021 reveals substantial variability in both drought and wet conditions across the Upper, Middle, and Lower Basins. In the Upper Awash River Basin (Figure 4.16), several extreme droughts were recorded. Notably, Ejersa Lele faced severe drought in 2009 (-1.56) and extreme drought in September 2009 (-2.11). Similarly, Hombole experienced extreme droughts in September 2009 (-2.04) and again in September 2015 (-2.12), making it one of the most affected stations in the Upper Basin. AA Bole and Akaki also recorded severe droughts in 2009, highlighting the Upper Basin's vulnerability, especially in that year. However, 2006 was the wettest year for the Upper Basin, with Akaki recording an SPI of 1.28 in July, and Mojo experiencing significantly wetter-than-normal conditions throughout the year.

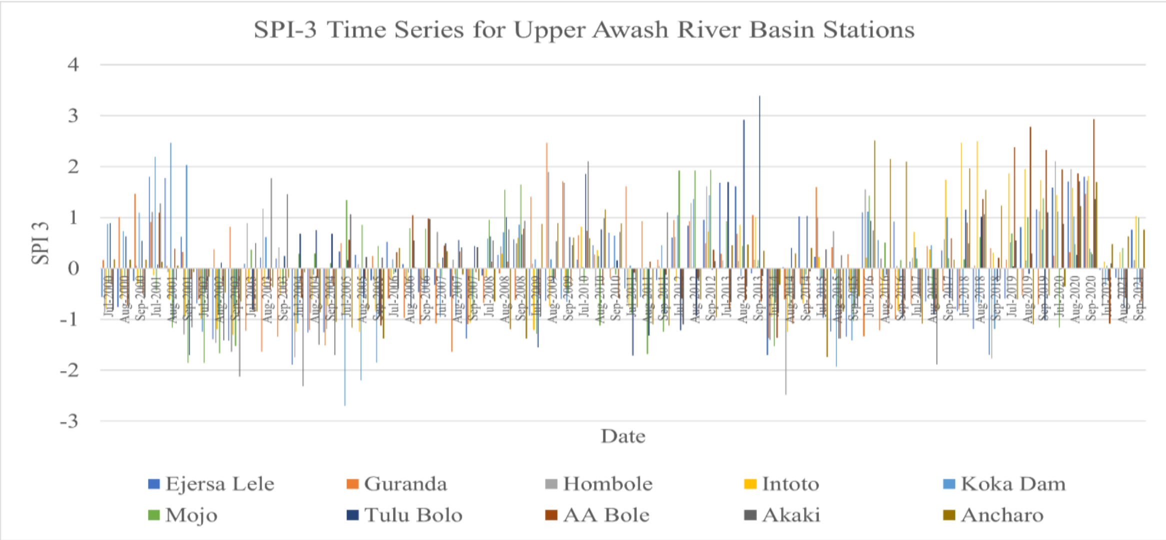

Figure 4-16 SPI-3 Time series for July to September from 2000 to 2021 in the Upper Awash River Basin

In the Middle Awash River Basin (Figure 4-17), which includes Adama, Awash 7 Kilo, Debre Sina, Etheya, Huruta, and Melka Sedi, drought conditions were generally milder compared to the Upper and Lower Basins. Adama experienced mild drought in July 2000 (-0.31) and moderate drought in August 2015 (-0.71), but avoided extreme droughts throughout the analysis period.

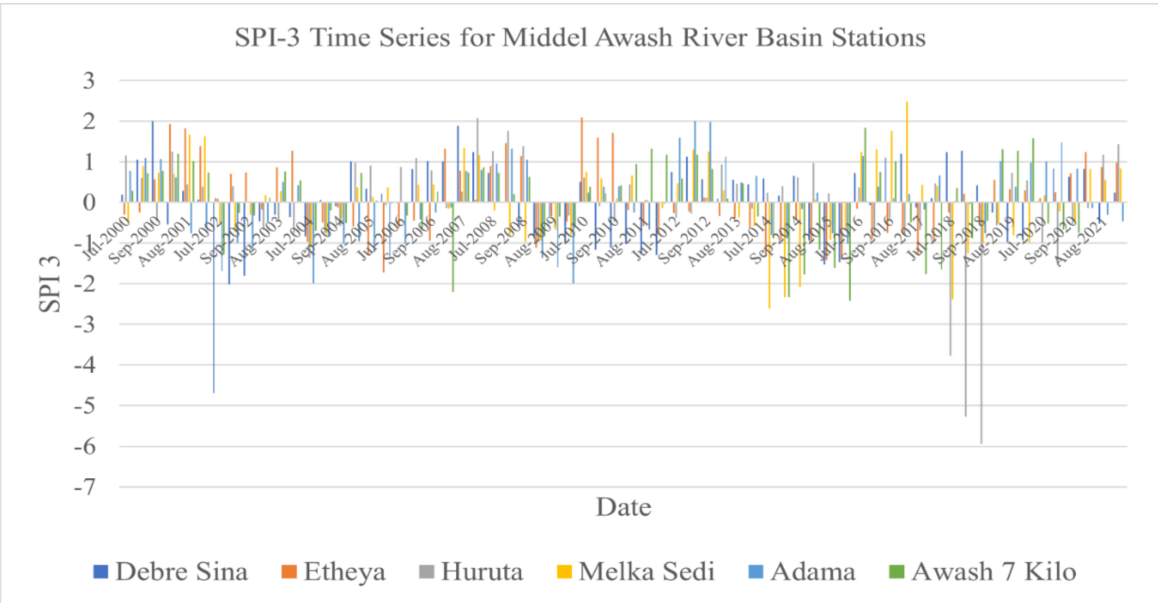

Figure 4-17 SPI-3 Time series for July to September from 2000 to 2021 in the Middle Awash River Basin

Melka Sedi showed resilience, with no severe droughts recorded, while Huruta faced severe drought only in September 2009 (-1.85). Like the Upper Basin, the wettest year for the Middle Basin was also 2006, with Adama recording an SPI of 1.09 in August, and Debre Sina experiencing a particularly wet year with an SPI of 1.05 in August.

The Lower Awash River Basin (Figure 4.18), which includes Asebe Teferi, Bati, Combolcha, Dengego, Dubity, Gewane, and Ruga, saw some of the most severe droughts during the analysis period. Dengego experienced extreme droughts in September 2009 (-1.70) and August 2020 (-1.89). Dubity recorded extreme drought in September 2015 (-2.02), and Ruga faced extreme drought in September 2009 (-2.05). Gewane also saw severe drought in September 2009 (-1.82), making 2009 a particularly challenging year for the Lower Basin. In contrast, the wettest year for the Lower Basin was 2010, with Combolcha recording an SPI of 1.45 in September, and stations like Dubity and Gewane benefiting from above-normal rainfall.

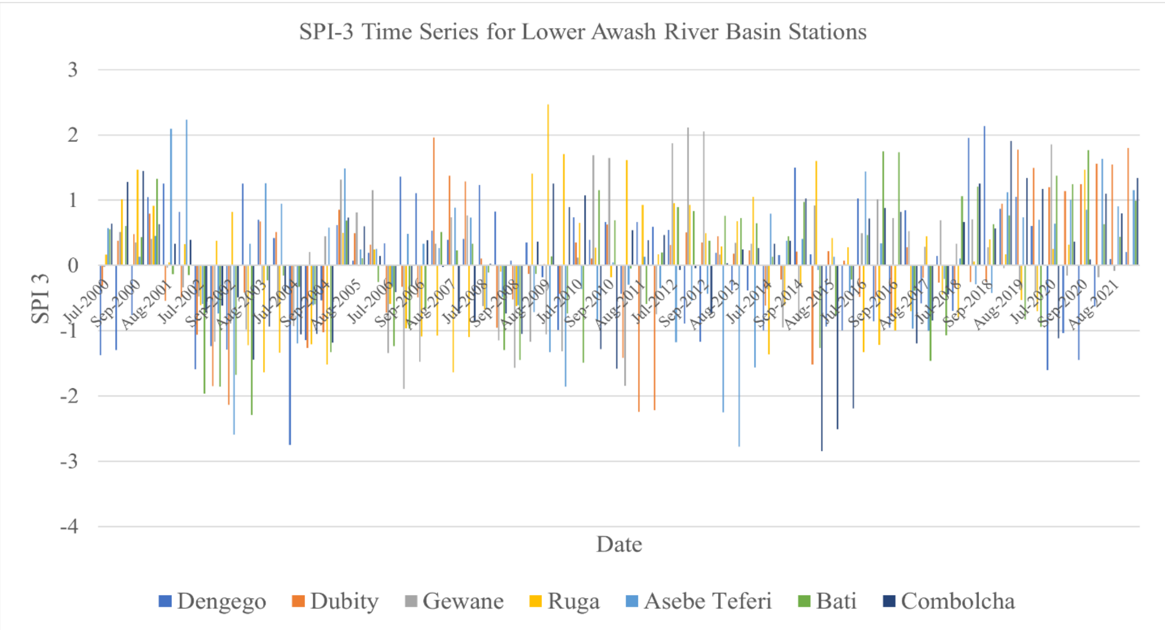

Figure 4-18 SPI-3 Time series for July to September from 2000 to 2021 in the Lower Awash River Basin

Overall, the Upper and Lower Awash River Basins experienced more frequent and severe droughts, with 2009 and 2015 standing out as the most drought-affected years. The highest drought recorded during the analysis period occurred at Hombole in the Upper Awash River Basin in September 2015, with an SPI value of -2.12. This was closely followed by extreme drought events at Ejersa Lele in September 2009 (-2.11) and Ruga in September 2009 (-

2.05). Meanwhile, the Middle Awash River Basin showed more resilience, with fewer and less intense drought events, especially in stations like Adama and Melka Sedi.

The wettest year across the entire Awash River Basin was 2006, with many stations in both the Upper and Middle Basins recording significantly positive SPI values. The Lower Basin, however, had its wettest year in 2010, reflecting the dynamic and cyclical nature of climate conditions in the Awash Basin. The variability between the wettest and driest years underscores the need for region-specific drought mitigation strategies, as well as preparedness for both drought and periods of intense wet conditions.

4.5. Pearson Correlation Test

4.5.1. Correlation Matrix of VCI, TCI, and VHI

The correlation matrix analysis for VCI, TCI, and VHI in Figure 4-19 reveals several important insights. The correlation between VCI and TCI is moderately positive, with a value of 0.53, indicating that improvements in vegetation conditions (VCI) are often associated with better TCI, though the relationship is not exceptionally strong. This suggests that other factors, besides temperature, may also influence vegetation conditions. VCI is primarily focused on vegetation health and growth, while TCI relates to temperature effects on vegetation. Given their different focuses, a moderate correlation is expected. Supporting these findings, Bekele and Tesfaye (2021) conducted a study on drought monitoring in the Upper Awash Basin, Ethiopia, and reported a similar moderate correlation between VCI and TCI. They emphasized that while temperature plays a role, vegetation health is also influenced by other factors such as rainfall and soil moisture, which aligns with the observation in this analysis.

Additionally, the correlation between VCI and VHI is quite strong, with a value of 0.92, as expected. Since VHI is a composite index incorporating VCI, this strong correlation highlights the close connection between vegetation condition and overall vegetation health. This finding is supported by the work of Abebe et al. (2020), who studied drought dynamics in Ethiopia's Rift Valley and observed a strong correlation between VCI and VHI, with values ranging from 0.85 to 0.93. Their research confirmed that VHI's integration of VCI is a significant factor contributing to the strong association, and they noted that temperature, represented by TCI, had a supportive but secondary role in overall vegetation health.

The correlation between TCI and VHI is also positive, with a value of 0.67, indicating that temperature plays a significant role in vegetation health, though its impact is less pronounced compared to VCI. This observation aligns with findings from Li et al. (2019), who analyzed drought indicators in semi-arid regions of China and reported a similar correlation between VCI and TCI, around 0.5. Their study also emphasized the importance of considering additional factors such as precipitation, evapotranspiration, and land management practices in understanding vegetation health.

The analysis shows a strong interrelationship between vegetation condition and health, with temperature exerting a supportive but less dominant influence. These insights, supported by studies from Ethiopia and globally, are valuable for understanding the factors that affect vegetation health and for improving drought monitoring and vegetation assessment efforts.

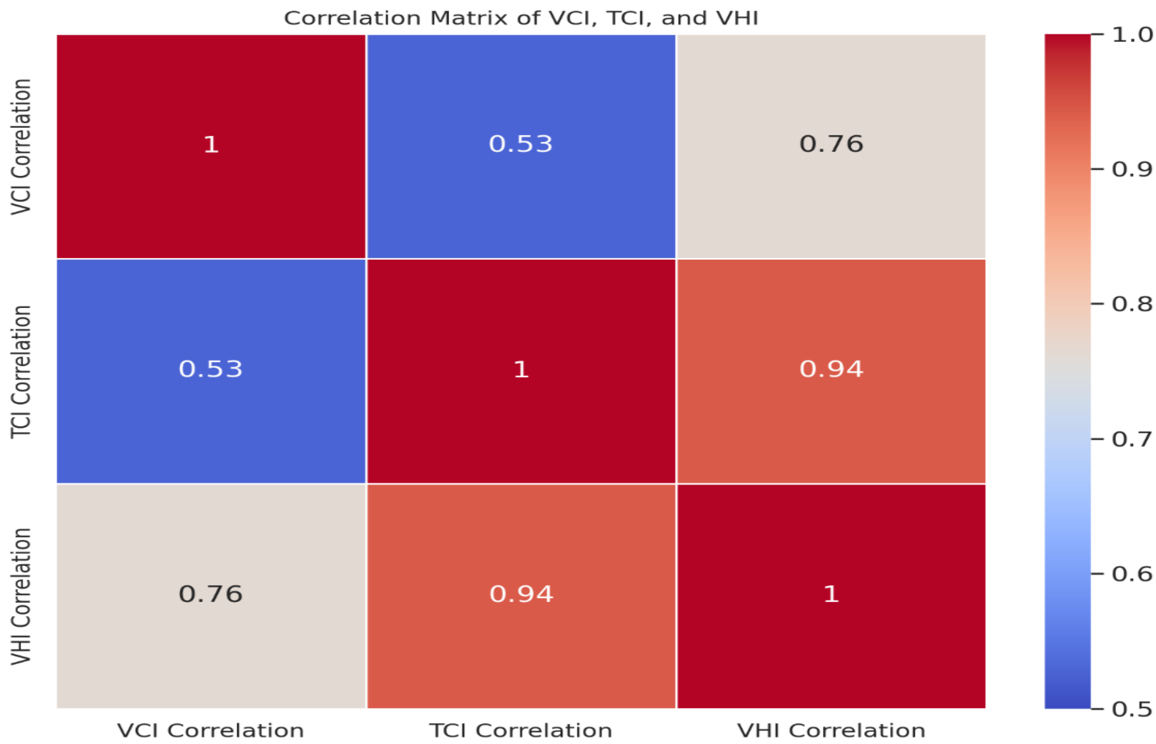

Figure 4-19 Correlation Matrix of VCI, TCI, and VHI

4.5.2. Correlation Analysis Between the VCI, TCI, and VHI With SPI3

The Pearson correlation analysis between the VCI, TCI, and VHI with SPI3 for various stations in the Awash River Basin elucidates several significant findings. The VCI correlation heatmap depicted in Figure 4-20 (next page) demonstrates moderate to strong positive correlations in the majority of stations, with values ranging from -0.21 to 0.57. Stations such as Asebe Teferi exhibited the highest correlation (0.57), whereas Melka Sedi displayed the lowest (-0.21), indicating a weak or inverse relationship between vegetation condition and SPI3. These results suggest that in most stations, an improvement in vegetation conditions corresponds to a decrease in drought severity.

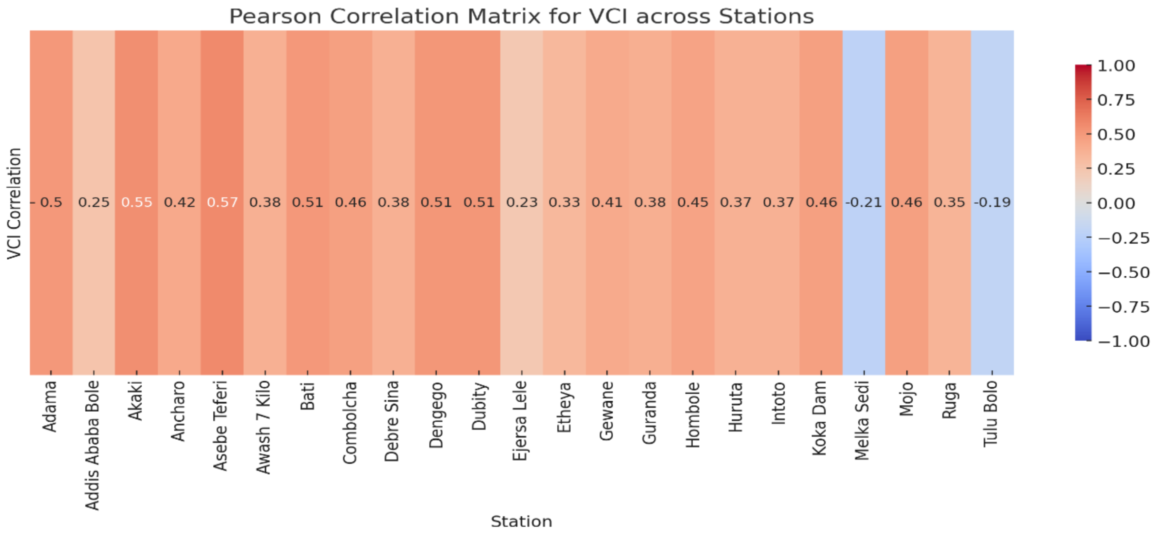

Figure 4-20 Correlation Matrix of VCI with SPI3

Figure 4-21 illustrates the TCI correlation heatmap, revealing a diverse range of correlations spanning from -0.26 to 0.53. The most pronounced correlation (0.53) was observed at Addis Ababa Bole, signifying a moderate association between temperature conditions and SPI3. Conversely, Melka Sedi displayed the weakest correlation (-0.26). These results indicate that temperature conditions exert a more varied influence on drought severity across the monitored stations compared to vegetation factors.

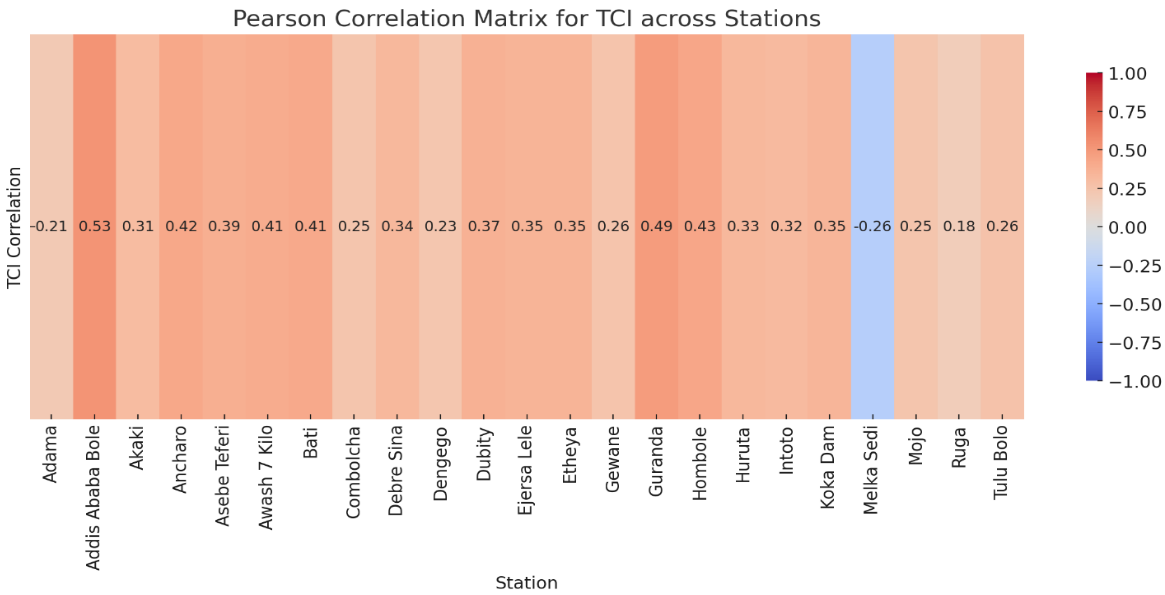

Figure 4-21 Correlation Matrix of TCI with SPI3

The VHI correlation heatmap shown in blow Figure 4-22, which combines both VCI and TCI, showed a similar but generally stronger pattern than VCI, with the highest correlation observed again in Asebe Teferi (0.63) and the lowest in Melka Sedi (-0.30).

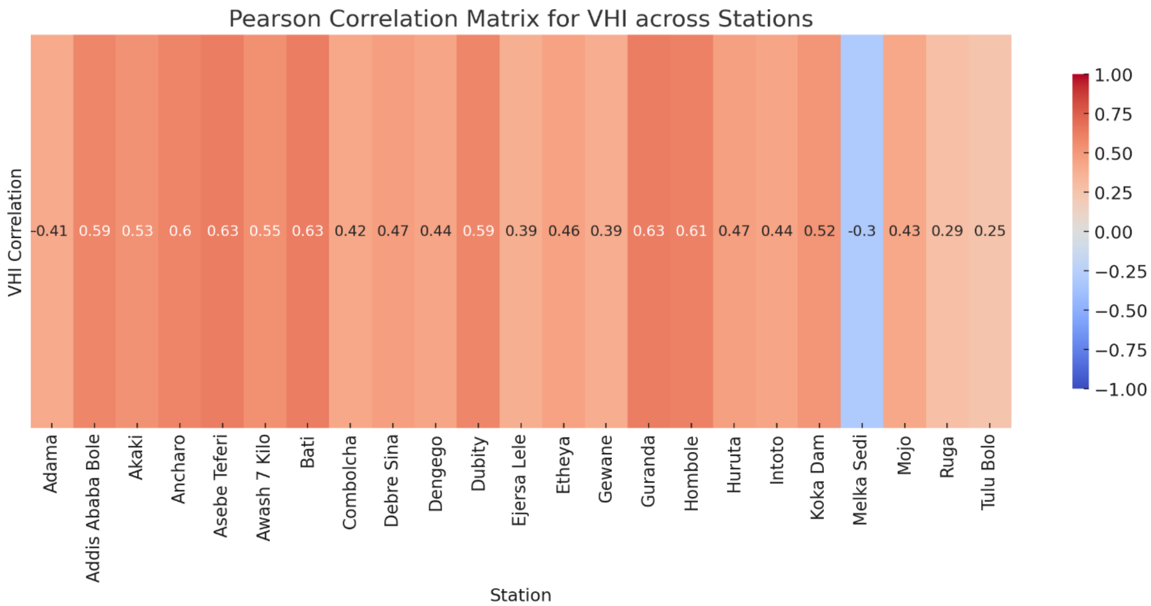

Figure 4-22 Correlation Matrix of VHI with SPI3

The negative correlation between vegetation condition (VCI) and SPI3 at Melka Sedi could be attributed to a combination of unique microclimatic conditions and temperature-induced stress. Melka Sedi may experience distinct environmental conditions that affect how vegetation responds to rainfall. According to Gebremeskel Haile et al., (2019), regions with semi-arid to arid climates often show non-linear vegetation responses to precipitation due to other stressors, including high temperatures and water retention capacity. High temperatures in Melka Sedi can lead to increased evapotranspiration rates, reducing the water available for vegetation even when rainfall levels are adequate. Ebrahimi-Khusfi et al., (2020) highlighted that temperature stress significantly impacts vegetation in arid and semi-arid regions, leading to an inverse or weak relationship between vegetation condition and SPI3. This indicates that while most stations show an improvement in vegetation conditions as drought severity decreases, Melka Sedi's vegetation may not follow this pattern due to the combined influence of temperature and unique climatic factors.

The results indicate that VCI and VHI tend to have stronger correlations with SPI3 compared to TCI, with stations like Asebe Teferi, Akaki, and Bati showing strong relationships, making them important locations for monitoring drought based on vegetation indices. In contrast, stations like Melka Sedi showed weaker or negative correlations, suggesting the presence of other influencing factors on drought patterns in these areas. Overall, this analysis highlights the spatial variability of drought impacts across the basin and underscores the usefulness of vegetation-based indices in monitoring drought conditions.

4.6. Discussion

Accurate drought monitoring is essential for effective water resource management, particularly in regions like the Awash River Basin, where agriculture and livelihoods are highly sensitive to climatic fluctuations. In this study, the VCI, TCI, and VHI were employed to assess drought severity across the basin from 2000 to 2021. The findings indicate both spatial and temporal variability in drought conditions, with mild and moderate droughts being the most frequent, while severe and extreme droughts were less common but highly impactful when they occurred. Additionally, by leveraging GEE's extensive geospatial datasets and cloud computing power, researchers can overcome limitations in traditional data collection methods; this innovative approach can unlock the potential for more accurate and efficient flood hazard and risk assessments in data-scarce regions. Consequently, it has the potential to significantly improve drought monitoring and management practices in Ethiopia and other countries facing similar data constraints.

The VCI results showed that mild droughts dominate the region, affecting over 50% of the area during many years. Severe and extreme droughts, although rare, were observed during certain years, such as 2009 and 2017. These findings align with previous studies that highlight the sensitivity of vegetation health to water stress during growing seasons (Kogan, 1995; Bento et al., 2020). The consistency of VCI as an indicator of vegetation health and drought stress is evident, with the index accurately capturing agricultural drought conditions, especially during critical growing months from July to September. The results show that the middle and lower basin regions are particularly vulnerable to drought, confirming earlier findings on regional agricultural risks under climate stress (Quiring & Ganesh, 2010).

Furthermore, TCI results provided insights into temperature-induced drought stress, highlighting the significant role that temperature plays in exacerbating drought impacts on vegetation. Notably, years like 2010 and 2017 exhibited extreme temperature conditions, contributing to more severe drought stress and revealing spatial variations in temperature-related stress across the basin, with northern regions often experiencing milder conditions compared to the central and southern areas. The VHI, being a composite index of VCI and TCI, offered a comprehensive view of drought conditions, reflecting both vegetation health and temperature stress, and revealed that moderate droughts were most prevalent, particularly during 2009 and 2017.

The trend analysis of VCI, TCI, and VHI over the study period showed no consistent long-term trend in vegetation health, indicating that drought conditions remain variable; however, years like 2009, 2010, and 2020 stood out, showing peaks in drought intensity. This variability highlights the complexity of drought impacts driven by both climatic and environmental factors. The frequency analysis further demonstrated that July was the most drought-affected month, while severe droughts were more frequent during this period, suggesting that temperature and water stress decline towards the end of the dry season.

The results of this study showed strong correlations between VCI, TCI, VHI, and the SPI3, indicating that drought conditions reflected by vegetation indices align well with precipitation-based assessments. However, the correlation between TCI and SPI3 was weaker, likely due to the independent impact of temperature on vegetation health. This spatial variability in correlations highlights the need for a multi-index approach to capture the full scope of drought impacts.

As with any remote sensing-based study, there are limitations; while VCI, TCI, and VHI provide valuable insights into drought conditions, they rely on satellite-derived data, which can sometimes misclassify land cover types or underestimate drought severity in areas with complex topography. Future studies could benefit from integrating higher-resolution datasets or ground-based observations to improve the accuracy of drought assessments, especially in areas where satellite data may be less reliable.

The findings of this study have important implications for addressing several Sustainable Development Goals (SDGs) related to agriculture, water management, climate resilience, and ecosystem health. The first SDG that is related to this topic is SDG 2: Zero Hunger highlights the threat of droughts to agricultural productivity, making the use of VCI crucial for monitoring agricultural droughts and identifying areas under severe water stress. By monitoring vegetation health and predicting drought impacts on crops, policymakers and farmers can implement adaptive strategies to mitigate yield losses, improve food security, and build resilience to climate shocks (Kumari & Shukla, 2023).

Another SDG that is related to this topic is SDG 6: Clean Water and Sanitation emphasizes the importance of drought impacts on water availability, and integrating VCI, TCI, and VHI provides valuable data for monitoring drought effects on agricultural land and water resources. The analysis of temperature-induced drought stress underscores the relationship between climatic extremes and water scarcity, supporting the development of water-saving strategies (Andres et al., 2018).

The next SDG that is related to this topic is SDG 13: Climate Action highlights the exacerbation of drought frequency and intensity due to climate change, as seen in years like 2009 and 2017. The monitoring approaches utilized in this study align with the urgent call for action against climate change, demonstrating how remote sensing tools can enhance understanding of climate-driven drought patterns (Curl et al., 2014). Finally, SDG 15: Life on Land addresses the profound impacts of drought on terrestrial ecosystems, and the findings related to VHI reveal vegetation stress and land degradation, supporting sustainable land management practices (López-Carr et al., 2023).

In conclusion, the findings of this study contribute to the achievement of multiple SDGs by providing actionable insights into drought monitoring and its broader implications. By integrating advanced remote sensing techniques with drought indices, this research demonstrates how innovative solutions can be leveraged to address critical global challenges such as food security, water scarcity, and climate change adaptation.

5. CONCLUSION AND RECOMMENDATIONS

5.1. Conclusion

Drought poses a significant threat to agricultural productivity and water availability, particularly in regions like the Awash River Basin, where livelihoods heavily depend on climatic stability. This study employed VCI, TCI, and VHI to assess drought severity from 2000 to 2021. The integration of these indices with GEE facilitated detailed assessments of drought impacts across different parts of the basin.

The analysis showed that mild drought was the most frequent condition, affecting over 50% of the area in many years. For instance, 2001, 2010, 2011, and 2021 saw mild drought affecting more than 70% of the basin. Moderate drought also accounted for a substantial portion of the affected area, especially in years like 2008, 2009, and 2016, where it surpassed 50%. Severe and extreme droughts, though less frequent, occurred in key years such as 2009 and 2017, which had the highest recorded impacts, especially in the middle and lower parts of the basin. The extreme drought events, while rare, had localized effects, particularly in 2009, 2012, and 2017, where drought severity exceeded 1%.

The temporal analysis revealed significant fluctuations in the drought conditions across the 22-year period. The mean annual VCI trend showed variability, with years like 2001, 2007, and 2020 showing improved vegetation health, while 2002 and 2015 stood out as particularly drought-stressed years. The TCI results highlighted the role of temperature stress in exacerbating drought impacts, with 2009 and 2017 experiencing severe temperature-induced droughts, especially in the northern and central parts of the basin. The VHI analysis combined the effects of both VCI and TCI, confirming that moderate droughts were the most frequent and extensive, affecting large portions of the basin during the study period.

The analysis using SPI3 data further reinforced the findings from VCI, TCI, and VHI. Stations in the upper and middle parts of the basin, like Ejersa Lele and Hombole, recorded extreme drought conditions, particularly in 2009 and 2015, reflecting the basin's vulnerability to both precipitation deficits and temperature extremes. In contrast, the lower parts of the basin, such as Adama and Melka Sedi, exhibited less severe drought impacts, with fewer extreme drought events.

Overall, this study demonstrates the effectiveness of GEE for large-scale drought monitoring in data-scarce regions. The average annual correlation between VCI and SPI3 was found to be moderate to strong in most stations, highlighting the reliability of using vegetation-based indices for drought assessments. The integration of satellite-based indices with in-situ data provides a more comprehensive understanding of drought impacts, especially for agriculture, and underscores the need for adaptive drought management strategies.

The findings from this study contribute to addressing SDGs, including SDG 2 (Zero Hunger), by identifying areas most affected by agricultural drought, and SDG 6 (Clean Water and Sanitation), by highlighting the impact of drought on water resources. Furthermore, this research aligns with SDG 13 (Climate Action), demonstrating the critical need for climate-resilient water and agricultural management in response to increased drought frequency and intensity.

5.2. Recommendations

- It is recommended that researchers and policymakers to utilize GEE for real-time and large-scale drought monitoring. GEE's ability to handle vast amounts of satellite data and its cloud-based processing platform make it an invaluable tool for regions with limited ground-based observations. This will enhance the efficiency and accuracy of drought assessments, especially in data sparse areas.

- It is encouraged to use multiple indices for a comprehensive drought analysis, as this approach combines the effects of vegetation health and temperature stress, providing a deeper understanding of drought impacts. By adopting a multi-index strategy, more accurate and insightful drought monitoring can be achieved across diverse climatic regions.

- Utilizing the code and methodology developed for this study, which will be shared on GitHub, is recommended to facilitate broader usage of GEE for drought monitoring. This approach will enable other researchers, practitioners, and policymakers to replicate and expand the study, fostering collaborative efforts in drought monitoring and contributing to a more informed response to climate variability.

- While satellite data is crucial, it is recommended to complement remote sensing analysis with multiple ground-based observations to enhance the accuracy of drought severity assessments. This hybrid approach can effectively address limitations in satellite data, particularly in areas with complex topography or land cover.

- Based on the findings of this study, it is recommended that drought mitigation efforts focus on the most vulnerable regions, particularly the middle and lower parts of the Awash River Basin, which experience frequent and severe droughts. Tailored interventions in these areas, such as water-saving technologies and sustainable agricultural practices, will help mitigate the impacts of drought on agriculture and livelihoods.

REFERENCES

Abera Tareke, K., & Gebeyehu Awoke, A. (2022). Hydrological and Meteorological Drought Monitoring and Trend Analysis in Abbay River Basin, Ethiopia. *Advances in Meteorology*, *2022*, e2048077. https://doi.org/10.1155/2022/2048077

Aksoy, S., Gorucu, O., & Sertel, E. (2019). Drought Monitoring using MODIS derived indices and Google Earth Engine Platform. *2019 8th International Conference on Agro-Geoinformatics (Agro-Geoinformatics)*, 1–6. https://doi.org/10.1109/Agro-Geoinformatics.2019.8820209

Alasow, A. A., Hamed, M. M., Rady, M., Arab, M. A., Muhammad, M. K. I., & Shahid, S. (2024). Spatiotemporal analysis of soil moisture drought in the Horn of Africa. *Theoretical and Applied Climatology*, *155*(8), 7165–7176. https://doi.org/10.1007/s00704-024-05052-z

Amani, M., Ghorbanian, A., Ahmadi, S. A., Kakooei, M., Moghimi, A., Mirmazloumi, S. M., Moghaddam, S. H. A., Mahdavi, S., Ghahremanloo, M., Parsian, S., Wu, Q., & Brisco, B. (2020). Google Earth Engine Cloud Computing Platform for Remote Sensing Big Data Applications: A Comprehensive Review. *IEEE Journal of Selected Topics in Applied Earth Observations and Remote Sensing*, *13*, 5326–5350. IEEE Journal of Selected Topics in Applied Earth Observations and Remote Sensing. https://doi.org/10.1109/JSTARS.2020.3021052

Andres, L., Boateng, K., Borja-Vega, C., & Thomas, E. (2018). A Review of In-Situ and Remote Sensing Technologies to Monitor Water and Sanitation Interventions. *Water*, *10*(6), Article 6. https://doi.org/10.3390/w10060756

Babaousmail, H., Ayugi, B. O., Hammad, Z., Alupot, D., Posset, K. R., Mumo, R., & Rajasekar, A. (2024). Quantifying Drought Impacts Based on the Reliability–Resiliency–Vulnerability Framework over East Africa. *Climate*, *12*(7), 92.

Baser, Q. A., Vahid, I., Gordana, K., & Zabihullah, N. (2022). Spatiotemporal and multi-sensor analysis of surface temperature, NDVI, and precipitation using google earth engine cloud computing platform. *Russian Journal of Earth Sciences*, *22*(6), 1–12. https://doi.org/10.2205/2022ES000812

Benedict, T. D., Brown, J. F., Boyte, S. P., Howard, D. M., Fuchs, B. A., Wardlow, B. D., Tadesse, T., & Evenson, K. A. (2021). Exploring VIIRS Continuity with MODIS in an Expedited Capability for Monitoring Drought-Related Vegetation Conditions. *Remote Sensing*, *13*(6), Article 6. https://doi.org/10.3390/rs13061210

Bojer, A. K., Biru, B. H., Al-Quraishi, A. M. F., Debelee, T. G., Negera, W. G., Woldesillasie, F. F., & Esubalew, S. Z. (2024). Machine learning and remote sensing based time series analysis for drought risk prediction in Borena Zone, Southwest Ethiopia. *Journal of Arid Environments*, *222*, 105160. https://doi.org/10.1016/j.jaridenv.2024.105160

Buishand, T. A. (1982). Some methods for testing the homogeneity of rainfall records. *Journal of Hydrology*, *58*(1), 11–27. https://doi.org/10.1016/0022-1694(82)90066-X

Chapman, D., Simon, T. A., Nguyen, P., & Halem, M. (2013). A Data Intensive Statistical Aggregation Engine: A Case Study for Gridded Climate Records. *2013 IEEE International Symposium on Parallel & Distributed Processing, Workshops and Phd Forum*, 2157–2164. https://doi.org/10.1109/IPDPSW.2013.87

Conversi, S., Carrion, D., Norcini, A., & Riva, M. (2023). INTEGRATING OPTICAL AND RADAR IMAGERY TO ENHANCE RIVER DROUGHT MONITORING. *The International Archives of the Photogrammetry, Remote Sensing and Spatial Information Sciences*, *XLVIII-1/W2-2023*, 1363–1371. https://doi.org/10.5194/isprs-archives-XLVIII-1-W2-2023-1363-2023

Curl, K., Neri, C., & Scott, C. (2014). Drought and water scarcity: Discourses and competing water demands in the context of climate change in arid Sonora, Mexico. In *Adaptation to Climate Change through Water Resources Management*. Routledge.

Daba, M. H., & You, S. (2022). Quantitatively Assessing the Future Land-Use/Land-Cover Changes and Their Driving Factors in the Upper Stream of the Awash River Based on the CA–Markov Model and Their Implications for Water Resources Management. *Sustainability*, *14*(3), Article 3. https://doi.org/10.3390/su14031538

Dai, A. (2011). Drought under global warming: A review. *WIREs Climate Change*, *2*(1), 45–65. https://doi.org/10.1002/wcc.81

Dale, V. H., Joyce, L. A., McNulty, S., Neilson, R. P., Ayres, M. P., Flannigan, M. D., Hanson, P. J., Irland, L. C., Lugo, A. E., Peterson, C. J., Simberloff, D., Swanson, F. J., Stocks, B. J., & Wotton, B. M. (2001). Climate Change and Forest Disturbances: Climate change can affect forests by altering the frequency, intensity, duration, and timing of fire, drought, introduced species, insect and pathogen outbreaks, hurricanes, windstorms, ice storms, or landslides. *BioScience*, *51*(9), 723–734. https://doi.org/10.1641/0006-3568(2001)051[0723:CCAFD]2.0.CO;2

Dutta, D., Kundu, A., & Patel, N. R. (2013). Predicting agricultural drought in eastern Rajasthan of India using NDVI and standardized precipitation index. *Geocarto International*, *28*(3), 192–209. https://doi.org/10.1080/10106049.2012.679975

Dutta, D., Kundu, A., Patel, N. R., Saha, S. K., & Siddiqui, A. R. (2015). Assessment of agricultural drought in Rajasthan (India) using remote sensing derived Vegetation Condition Index (VCI) and Standardized Precipitation Index (SPI). *The Egyptian Journal of Remote Sensing and Space Science*, *18*(1), 53–63. https://doi.org/10.1016/j.ejrs.2015.03.006

Ebrahimi-Khusfi, Z., Mirakbari, M., & Khosroshahi, M. (2020). Vegetation response to changes in temperature, rainfall, and dust in arid environments. *Environmental Monitoring and Assessment*, *192*(11), 691. https://doi.org/10.1007/s10661-020-08644-0

Edossa, D. C., Babel, M. S., & Das Gupta, A. (2010). Drought Analysis in the Awash River Basin, Ethiopia. *Water Resources Management*, *24*(7), 1441–1460. https://doi.org/10.1007/s11269-009-9508-0

Ejaz, N., Bahrawi, J., Alghamdi, K. M., Rahman, K. U., & Shang, S. (2023). Drought Monitoring Using Landsat Derived Indices and Google Earth Engine Platform: A Case Study from Al-Lith Watershed, Kingdom of Saudi Arabia. *Remote Sensing*, *15*(4), Article 4. https://doi.org/10.3390/rs15040984

Ettehadi Osgouei, P., Kaya, S., Sertel, E., & Alganci, U. (2019). Separating Built-Up Areas from Bare Land in Mediterranean Cities Using Sentinel-2A Imagery. *Remote Sensing*, *11*(3), 345. https://doi.org/10.3390/rs11030345

Fentaw, A. E., Yimer, A. A., & Zeleke, G. A. (2023). Monitoring spatio-temporal drought dynamics using multiple indices in the dry land of the upper Tekeze Basin, Ethiopia. *Environmental Challenges*, *13*, 100781. https://doi.org/10.1016/j.envc.2023.100781

Gao, Y., Merz, C., Lischeid, G., & Schneider, M. (2018). A review on missing hydrological data processing. *Environmental Earth Sciences*, *77*(2), 47. https://doi.org/10.1007/s12665-018-7228-6

Gebrehiwot, T., van der Veen, A., & Maathuis, B. (2011). Spatial and temporal assessment of drought in the Northern highlands of Ethiopia. *International Journal of Applied Earth Observation and Geoinformation*, *13*(3), 309–321. https://doi.org/10.1016/j.jag.2010.12.002

Gebremeskel Haile, G., Tang, Q., Sun, S., Huang, Z., Zhang, X., & Liu, X. (2019). Droughts in East Africa: Causes, impacts and resilience. *Earth-Science Reviews*, *193*, 146–161. https://doi.org/10.1016/j.earscirev.2019.04.015

Gebreyesus, M., Chernet, A., Molla, M., Ashine, T., & Kelem, G. (2020). Drought Characterization Using Reconnaissance Drought Index (RDI): In the case of Awash River Basin, Ethiopia. *Int J Environ Sci Nat Res*, *26*(3), 70–77.

Gorelick, N., Hancher, M., Dixon, M., Ilyushchenko, S., Thau, D., & Moore, R. (2017). Google Earth Engine: Planetary-scale geospatial analysis for everyone. *Remote Sensing of Environment*, *202*, 18–27. https://doi.org/10.1016/j.rse.2017.06.031

Gottfriedsen, J., Berrendorf, M., Gentine, P., Reichstein, M., Weigel, K., Hassler, B., & Eyring, V. (2021). *On the Generalization of Agricultural Drought Classification from Climate Data* (arXiv:2111.15452). arXiv. http://arxiv.org/abs/2111.15452

Hashemzadeh Ghalhari, M., Vafakhah, M., & Damavandi, A. A. (2022). Agricultural drought assessment using vegetation indices derived from MODIS time series in Tehran Province. *Arabian Journal of Geosciences*, *15*(5), 412. https://doi.org/10.1007/s12517-022-09741-9

Hazaymeh, K., & Hassan, Q. K. (2016). Remote sensing of agricultural drought monitoring: A state of art review. *AIMS Environmental Science*, *3*(4), 604–630.

Hazaymeh, K. M. A., & Zeitoun, M. (2024). Google Earth Engine (GEE) for Modeling and Monitoring Hydrometeorological Events Using Remote Sensing Data. In *Modeling and Monitoring Extreme Hydrometeorological Events* (pp. 114–134). IGI Global. https://doi.org/10.4018/978-1-6684-8771-6.ch006

Huang, J., Zhuo, W., Li, Y., Huang, R., Sedano, F., Su, W., Dong, J., Tian, L., Huang, Y., Zhu, D., & Zhang, X. (2020). Comparison of three remotely sensed drought indices for assessing the impact of drought on winter wheat yield. *International Journal of Digital Earth*, *13*(4), 504–526. https://doi.org/10.1080/17538947.2018.1542040

Huete, A., Didan, K., Miura, T., Rodriguez, E. P., Gao, X., & Ferreira, L. G. (2002). Overview of the radiometric and biophysical performance of the MODIS vegetation indices. *Remote Sensing of Environment*, *83*(1–2), 195–213. https://doi.org/10.1016/S0034-4257(02)00096-2

Hunt, E. R., & Rock, B. N. (1989). Detection of changes in leaf water content using Near- and Middle-Infrared reflectances. *Remote Sensing of Environment*, *30*(1), 43–54. https://doi.org/10.1016/0034-4257(89)90046-1

Jain, V. K., Pandey, R. P., Jain, M. K., & Byun, H.-R. (2015). Comparison of drought indices for appraisal of drought characteristics in the Ken River Basin. *Weather and Climate Extremes*, *8*, 1–11. https://doi.org/10.1016/j.wace.2015.05.002

Karnieli, A., Bayasgalan, M., Bayarjargal, Y., Agam, N., Khudulmur, S., & Tucker, C. J. (2006). Comments on the use of the Vegetation Health Index over Mongolia. *International Journal of Remote Sensing*, *27*(10), 2017–2024. https://doi.org/10.1080/01431160500121727

Kogan, F. N. (1990). Remote sensing of weather impacts on vegetation in non-homogeneous areas. *International Journal of Remote Sensing*, *11*(8), 1405–1419. https://doi.org/10.1080/01431169008955102

Kogan, F. N. (1995). Application of vegetation index and brightness temperature for drought detection. *Advances in Space Research*, *15*(11), 91–100. https://doi.org/10.1016/0273-1177(95)00079-T

Kogan, F. N. (1997). Global drought watch from space. *Bulletin of the American Meteorological Society*, *78*(4), 621–636.

Kovács, F. (2018). NDVI/EVI monitoring in forest areas to assessment the climate change effects in Hungarian Great Plain from 2000. *Remote Sensing for Agriculture, Ecosystems, and Hydrology XX*, *10783*, 362–370. https://doi.org/10.1117/12.2325647

Kumari, C., & Shukla, R. (2023). *Nature Based Solutions (NBS) to achieve food security and SDGs in drought prone subtropical area* (EGU23-10930). EGU23. Copernicus Meetings. https://doi.org/10.5194/egusphere-egu23-10930

Lambin, E. F., & Ehrlich, D. (1996). The surface temperature-vegetation index space for land cover and land-cover change analysis. *International Journal of Remote Sensing*, *17*(3), 463–487. https://doi.org/10.1080/01431169608949021

Lei, Z., Jianjun, W., & Jie, Z. (2015). Remote sensing-based drought monitoring approach and research progress. *Scientia Geographica Sinica*, *35*(5), 630–636.

Li, Y., Huang, B., Tan, C., Zhang, X., Cherubini, F., & Rust, H. W. (2024). Investigating the global and regional response of drought to idealized deforestation using multiple global climate models. *EGUsphere*, 1–40. https://doi.org/10.5194/egusphere-2024-1270

Liang, L., Qiu, S., Yan, J., Shi, Y., & Geng, D. (2021). VCI-Based Analysis on Spatiotemporal Variations of Spring Drought in China. *International Journal of Environmental Research and Public Health*, *18*(15), Article 15. https://doi.org/10.3390/ijerph18157967

Liou, Y.-A., & Mulualem, G. M. (2019). Spatio–temporal Assessment of Drought in Ethiopia and the Impact of Recent Intense Droughts. *Remote Sensing*, *11*(15), Article 15. https://doi.org/10.3390/rs11151828

LIU, W. T., & KOGAN, F. N. (1996). Monitoring regional drought using the Vegetation Condition Index. *International Journal of Remote Sensing*, *17*(14), 2761–2782. https://doi.org/10.1080/01431169608949106

Liu, X., Zhu, X., Pan, Y., Li, S., Liu, Y., & Ma, Y. (2016). Agricultural drought monitoring: Progress, challenges, and prospects. *Journal of Geographical Sciences*, *26*, 750–767.

López-Carr, D., Pricope, N. G., Mwenda, K. M., Daldegan, G. A., & Zvoleff, A. (2023). A Conceptual Approach towards Improving Monitoring of Living Conditions for Populations Affected by Desertification, Land Degradation, and Drought. *Sustainability*, *15*(12), Article 12. https://doi.org/10.3390/su15129400

Lyu, Z.-Z., Gao, H., Gao, R., & Ding, T. (2023). Extreme characteristics and causes of the drought event in the whole Yangtze River Basin in the midsummer of 2022. *Advances in Climate Change Research*, *14*(5), 642–650. https://doi.org/10.1016/j.accre.2023.09.007

Machiwal, D., Meena, H. M., & Singh, D. V. (2022). Chapter 34—Overview of trend and homogeneity tests and their application to rainfall time series. In M. Zakwan, A. Wahid, M. Niazkar, & U. Chatterjee (Eds.), *Current Directions in Water Scarcity Research* (Vol. 7, pp. 599–620). Elsevier. https://doi.org/10.1016/B978-0-323-91910-4.00034-0

Malede, D. A., Andualem, T. G., Yibeltal, M., Alamirew, T., kassie, A. E., Demeke, G. G., & Mekonnen, Y. G. (2024). Climate change impacts on hydroclimatic variables over Awash basin, Ethiopia: A systematic review. *Discover Applied Sciences*, *6*(1), 27. https://doi.org/10.1007/s42452-024-05640-8

McKee, T. B., Doesken, N. J., & Kleist, J. (1993). The relationship of drought frequency and duration to time scales. *Proceedings of the 8th Conference on Applied Climatology*, *17*(22), 179–183.

Menegbo, E. M. (2024). Assessment of vegetation health index (VHI) using Modis data in rivers state, Nigeria. *International Journal of Advanced Geosciences*, *12*(2), Article 2. https://doi.org/10.14419/1w1pqg42

Mera, G. A. (2018). Drought and its impacts in Ethiopia. *Weather and Climate Extremes*, *22*, 24–35. https://doi.org/10.1016/j.wace.2018.10.002

Meskelu, E., Ayana, M., & Birhanu, D. (2024). Analysis of long-term rainfall trend, variability, and drought in the Awash River Basin, Ethiopia. *Theoretical and Applied Climatology*, *155*(9), 9029–9050. https://doi.org/10.1007/s00704-024-05170-8

Mokhtari, R., & Akhoondzadeh, M. (2021). Data fusion and machine learning algorithms for drought forecasting using satellite data. *Journal of the Earth and Space Physics*, *46*(4), 231–246.

Molla, S. D., Zeleke, M. T., & Tamiru, S. M. (2024). Rural Household Perception of Drought Occurrence and Its Influence on Livelihood Strategy in Northeast Ethiopia. *Advances in Agriculture*, *2024*(1), 8860956. https://doi.org/10.1155/2024/8860956

Mukhawana, M. B., Kanyerere, T., & Kahler, D. (2023). Review of In-Situ and Remote Sensing-Based Indices and Their Applicability for Integrated Drought Monitoring in South Africa. *Water*, *15*(2), Article 2. https://doi.org/10.3390/w15020240

Nagarajan, R. (2010). *Drought Assessment*. Springer Science & Business Media.

Narasimhan, B., & Srinivasan, R. (2005). Development and evaluation of Soil Moisture Deficit Index (SMDI) and Evapotranspiration Deficit Index (ETDI) for agricultural drought monitoring. *Agricultural and Forest Meteorology*, *133*(1), 69–88. https://doi.org/10.1016/j.agrformet.2005.07.012

Ngoc Hanh, L., Hoang Son, N., Phuc Chi Lang, L., Thi An, T., Van An, N., & Phuoc Minh, T. (2024). Spatial-Temporal Assessment of Drought in Hoa Vang district, Da Nang City, Vietnam Using Remote Sensing and Google Earth Engine. *IOP Conference*

Series: Earth and Environmental Science, *1345*(1), 012013. https://doi.org/10.1088/1755-1315/1345/1/012013

Nones, M. (2024). Satellite-Based Monitoring of Drought at the Watershed Scale. In M. B. Kalinowska, M. M. Mrokowska, & P. M. Rowiński (Eds.), *Advances in Hydraulic Research* (pp. 281–291). Springer Nature Switzerland. https://doi.org/10.1007/978-3-031-56093-4_22

Ozelkan, E., Chen, G., & Ustundag, B. B. (2016). Multiscale object-based drought monitoring and comparison in rainfed and irrigated agriculture from Landsat 8 OLI imagery. *International Journal of Applied Earth Observation and Geoinformation*, *44*, 159–170. https://doi.org/10.1016/j.jag.2015.08.003

Pachauri, R. K., Allen, M. R., Barros, V. R., Broome, J., Cramer, W., Christ, R., Church, J. A., Clarke, L., Dahe, Q., & Dasgupta, P. (2014). *Climate change 2014: Synthesis report. Contribution of Working Groups I, II and III to the fifth assessment report of the Intergovernmental Panel on Climate Change*. Ipcc.

Paez-Trujilo, A., Cañon, J., Hernandez, B., Corzo, G., & Solomatine, D. (2023). Multivariate regression trees as an "explainable machine learning" approach to explore relationships between hydroclimatic characteristics and agricultural and hydrological drought severity: Case of study Cesar River basin. *Natural Hazards and Earth System Sciences*, *23*(12), 3863–3883. https://doi.org/10.5194/nhess-23-3863-2023

Pirnia, A., Golshan, M., Darabi, H., Adamowski, J., & Rozbeh, S. (2018). Using the Mann–Kendall test and double mass curve method to explore stream flow changes in response to climate and human activities. *Journal of Water and Climate Change*, *10*(4), 725–742. https://doi.org/10.2166/wcc.2018.162

Priya, M. V., Kalpana, R., Pazhanivelan, S., Kumaraperumal, R., Ragunath, K. P., Vanitha, G., Nihar, A., Prajesh, P. J., & V, V. (2023). Monitoring vegetation dynamics using multi-temporal Normalized Difference Vegetation Index (NDVI) and Enhanced Vegetation Index (EVI) images of Tamil Nadu. *Journal of Applied and Natural Science*, *15*(3), Article 3. https://doi.org/10.31018/jans.v15i3.4803

Qamer, F. M., Krupnik, T. J., Pandey, P. R., & Ahmad, B. (2019). *Resource book: Earth observation and climate data analysis for agricultural drought monitoring in South Asia*. South Asian Association for Regional Cooperation (SAARC) Agriculture Centre ….

Qian, X., Liang, L., Shen, Q., Sun, Q., Zhang, L., Liu, Z., Zhao, S., & Qin, Z. (2016). Drought trends based on the VCI and its correlation with climate factors in the agricultural areas of China from 1982 to 2010. *Environmental Monitoring and Assessment*, *188*(11), 639. https://doi.org/10.1007/s10661-016-5657-9

Qiu, M., Ratledge, N., Azevedo, I. M. L., Diffenbaugh, N. S., & Burke, M. (2023). Drought impacts on the electricity system, emissions, and air quality in the western United States. *Proceedings of the National Academy of Sciences*, *120*(28), e2300395120. https://doi.org/10.1073/pnas.2300395120

Sazib, N., Mladenova, I., & Bolten, J. (2018). Leveraging the Google Earth Engine for Drought Assessment Using Global Soil Moisture Data. *Remote Sensing*, *10*(8), Article 8. https://doi.org/10.3390/rs10081265

Scanlon, B. R., Faunt, C. C., Longuevergne, L., Reedy, R. C., Alley, W. M., McGuire, V. L., & McMahon, P. B. (2012). Groundwater depletion and sustainability of irrigation in the US High Plains and Central Valley. *Proceedings of the National Academy of Sciences*, *109*(24), 9320–9325.

Senay, G. B., Velpuri, N. M., Bohms, S., Budde, M., Young, C., Rowland, J., & Verdin, J. P. (2015). Drought monitoring and assessment: Remote sensing and modeling approaches for the famine early warning systems network. In *Hydro-meteorological hazards, risks and disasters* (pp. 233–262). Elsevier.

Sime, C. H., & Dibaba, W. T. (2023). Evaluation of CMIP6 model performance and extreme precipitation prediction in the Awash basin. *Heliyon*, *9*(11). https://doi.org/10.1016/j.heliyon.2023.e21578

Sivakumar, M. V., Wilhite, D. A., Svoboda, M. D., Hayes, M., & Motha, R. (2011). Drought risk and meteorological droughts. *Background Paper Prepared for The*.

Sun, X., Wang, M., Li, G., & Wang, Y. (2020). Regional-scale drought monitor using synthesized index based on remote sensing in northeast China. *Open Geosciences*, *12*(1), 163–173.

Teshome, A., & Zhang, J. (2019). Increase of Extreme Drought over Ethiopia under Climate Warming. *Advances in Meteorology*, *2019*, 5235429. https://doi.org/10.1155/2019/5235429

Thenkabail, P. S., & Rhee, J. (2017). GIScience and remote sensing (TGRS) special issue on advances in remote sensing and GIS-based drought monitoring. In *GIScience & Remote Sensing* (Vol. 54, Issue 2, pp. 141–143). Taylor & Francis.

Thilagaraj, P., Masilamani, P., Venkatesh, R., & Killivalavan, J. (2021). GOOGLE EARTH ENGINE BASED AGRICULTURAL DROUGHT MONITORING IN KODAVANAR WATERSHED, PART OF AMARAVATHI BASIN, TAMIL NADU, INDIA. *The International Archives of the Photogrammetry, Remote Sensing and Spatial Information Sciences*, *XLIII-B5-2021*, 43–49. XXIV ISPRS Congress <q>Imaging today, foreseeing tomorrow</q>, Commission V and Youth Forum - 2021 edition, 5–9 July 2021. https://doi.org/10.5194/isprs-archives-XLIII-B5-2021-43-2021

Tofu, D. A. (2024). Evaluating the impacts of climate-induced east Africa’s recent disastrous drought on the pastoral livelihoods. *Scientific African*, *24*, e02219. https://doi.org/10.1016/j.sciaf.2024.e02219

Tucker, C. J. (1979). Red and photographic infrared linear combinations for monitoring vegetation. *Remote Sensing of Environment*, *8*(2), 127–150. https://doi.org/10.1016/0034-4257(79)90013-0

Tucker, C. J., & Choudhury, B. J. (1987). Satellite remote sensing of drought conditions. *Remote Sensing of Environment*, *23*(2), 243–251. https://doi.org/10.1016/0034-4257(87)90040-X

Van Loon, A. F. (2015). Hydrological drought explained. *Wiley Interdisciplinary Reviews: Water*, *2*(4), 359–392.

Vicente-Serrano, S. M., Beguería, S., & López-Moreno, J. I. (2010). A Multiscalar Drought Index Sensitive to Global Warming: The Standardized Precipitation Evapotranspiration Index. *Journal of Climate*, *23*(7), 1696–1718. https://doi.org/10.1175/2009JCLI2909.1

Wang, F., Wang, Z., Yang, H., Di, D., Zhao, Y., Liang, Q., & Hussain, Z. (2020). Comprehensive evaluation of hydrological drought and its relationships with meteorological drought in the Yellow River basin, China. *Journal of Hydrology*, 124751. https://doi.org/10.1016/j.jhydrol.2020.124751

Wang, P., Asare, E., Pitzer, V., Dubrow, R., & Chen, K. (2022). Long-term Drought and Diarrhea among Children under Five and the Role of Water, Sanitation, and Hygiene Practices. *ISEE Conference Abstracts*, *2022*(1). https://doi.org/10.1289/isee.2022.O-OP-265

Wei, Z., & Fang, W. (2024). UV-NDVI for real-time crop health monitoring in vertical farms. *Smart Agricultural Technology*, *8*, 100462. https://doi.org/10.1016/j.atech.2024.100462

West, H., Quinn, N., & Horswell, M. (2019). Remote sensing for drought monitoring & impact assessment: Progress, past challenges and future opportunities. *Remote Sensing of Environment*, *232*, 111291. https://doi.org/10.1016/j.rse.2019.111291

Wilhite, D. A. (2000). *Drought as a natural hazard: Concepts and definitions*.

Xie, F., & Fan, H. (2021). Deriving drought indices from MODIS vegetation indices (NDVI/EVI) and Land Surface Temperature (LST): Is data reconstruction necessary? *International Journal of Applied Earth Observation and Geoinformation*, *101*, 102352. https://doi.org/10.1016/j.jag.2021.102352

Zeng, J., Zhang, R., Qu, Y., Bento, V. A., Zhou, T., Lin, Y., Wu, X., Qi, J., Shui, W., & Wang, Q. (2022). Improving the drought monitoring capability of VHI at the global scale via ensemble indices for various vegetation types from 2001 to 2018. *Weather and Climate Extremes*, *35*, 100412. https://doi.org/10.1016/j.wace.2022.100412

Zhang, A., & Jia, G. (2013). Monitoring meteorological drought in semiarid regions using multi-sensor microwave remote sensing data. *Remote Sensing of Environment*, *134*, 12–23. https://doi.org/10.1016/j.rse.2013.02.023

Zhang, D., Ying, C., Wu, L., Meng, Z., Wang, X., & Ma, Y. (2023). Using Time Series Sentinel Images for Object-Oriented Crop Extraction of Planting Structure in the Google Earth Engine. *Agronomy*, *13*(9), Article 9. https://doi.org/10.3390/agronomy13092350

Zhang, L., Jiao, W., Zhang, H., Huang, C., & Tong, Q. (2017). Studying drought phenomena in the Continental United States in 2011 and 2012 using various drought indices. *Remote Sensing of Environment*, *190*, 96–106.

Zhou, J., Fan, Y., Guan, Q., & Feng, G. (2024). Research on Drought Monitoring Based on Deep Learning: A Case Study of the Huang-Huai-Hai Region in China. *Land*, *13*(5), Article 5. https://doi.org/10.3390/land13050615

Zhou, X., & Wei, X. (2024). Feature Aggregation Network for Building Extraction from High-Resolution Remote Sensing Images. In F. Liu, A. A. Sadanandan, D. N. Pham, P. Mursanto, & D. Lukose (Eds.), *PRICAI 2023: Trends in Artificial Intelligence* (Vol. 14327, pp. 105–116). Springer Nature Singapore. https://doi.org/10.1007/978-981-99-7025-4_9

APPENDICES

Appendix A

Appendix A.1 Available Meteorological Stations used for Awash River Basin

St.No	Stations Name	Latitude	Longitude	Elevation	Record length		
					From	To	Total yr
1	Adama	8.55	39.28	1622	2000	2021	22
2	Addis Ababa Bole	8.98	38.8	2354	2000	2021	22
3	Akaki	8.87	38.79	2057	2000	2021	22
4	Ancharo	11.05	39.63	2000	2000	2021	22
5	Asebe Teferi	9.07	40.87	1792	2000	2021	22
6	Awash 7 Kilo	8.98	40.15	923	2000	2021	22
7	Bati	11.2	40.02	1660	2000	2021	22
8	Combolcha	11.08	39.72	1857	2000	2021	22
9	Debre Sina	9.87	39.75	2800	2000	2021	22
10	Dengego	9.45	41.92	2078	2000	2021	22
11	Dubity	11.72	41.01	376	2000	2021	22
12	Ejersa Lele	8.24	38.69	1797	2000	2021	22
13	Etheya	8.13	39.33	2129	2000	2021	22
14	Gewane	10.15	40.63	568	2000	2021	22
15	Guranda	8.91	38.59	2187	2000	2021	22
16	Hombole	8.37	38.77	1743	2000	2021	22
17	Huruta	8.14	39.34	2044	2000	2021	22
18	Intoto	9.08	38.73	2903	2000	2021	22
19	Koka Dam	8.47	39.15	1618	2000	2021	22
20	Logya	11.65	41	393	2000	2021	22
21	Melka Sedi	9.24	40.17	749	2000	2021	22
22	Mojo	8.61	39.11	1763	2000	2021	22
23	Tulu Bolo	8.65	38.21	2190	2000	2021	22

Appendix B

Appendix B.1 VCI Drought Areas and Percentages (2000-2021)

Year	VCI Extreme Drought	VCI Mild Drought	VCI Moderate Drought	VCI No Drought	VCI Severe Drought	Total Area	VCI Extreme Drought %	VCI Mild Drought %	VCI Moderate Drought %	VCI No Drought %	VCI Severe Drought %
2000	9.45	64506.62	47672.49	4054.26	1529.18	117772.0	0.01	54.77	40.48	3.44	1.3
2001	60.07	72892.29	37882.06	6141.95	795.63	117772.0	0.05	61.89	32.17	5.21	0.68
2002	35.53	68499.25	41226.15	5329.25	2681.82	117772.0	0.03	58.16	35.0	4.52	2.28
2003	2.57	67081.48	45018.51	4784.23	885.21	117772.0	0.0	56.96	38.23	4.06	0.75
2004	11.1	64516.18	46329.04	4742.19	2173.49	117772.0	0.01	54.78	39.34	4.03	1.85
2005	23.31	70268.83	40818.79	5270.02	1391.05	117772.0	0.02	59.67	34.66	4.47	1.18
2006	2.08	63239.97	45647.88	7434.64	1447.43	117772.0	0.0	53.7	38.76	6.31	1.23
2007	17.68	67902.04	43502.46	4887.06	1462.76	117772.0	0.02	57.66	36.94	4.15	1.24
2008	26.12	60094.8	51874.69	3334.53	2441.86	117772.0	0.02	51.03	44.05	2.83	2.07
2009	9.93	57878.48	54458.16	2778.82	2646.61	117772.0	0.01	49.14	46.24	2.36	2.25
2010	12.07	74609.33	34092.54	8386.83	671.23	117772.0	0.01	63.35	28.95	7.12	0.57
2011	25.94	78306.32	34971.09	3951.55	517.1	117772.0	0.02	66.49	29.69	3.36	0.44

2012	4.77	59076.13	51721.62	4216.55	2752.93	117772.0	0.0	50.16	43.92	3.58	2.34
2013	2.62	68972.28	42700.86	5401.76	694.48	117772.0	0.0	58.56	36.26	4.59	0.59
2014	7.07	73311.89	37687.57	5608.24	1157.23	117772.0	0.01	62.25	32.0	4.76	0.98
2015	2.14	47228.91	66483.53	1660.39	2397.03	117772.0	0.0	40.1	56.45	1.41	2.04
2016	45.5	57924.0	54247.18	3895.32	1660.0	117772.0	0.04	49.18	46.06	3.31	1.41
2017	7.08	47715.73	66991.38	1607.33	1450.48	117772.0	0.01	40.52	56.88	1.37	1.23
2018	22.76	64309.66	48363.17	3563.11	1513.3	117772.0	0.02	54.61	41.07	3.02	1.28
2019	63.52	69296.52	39384.3	7581.41	1446.25	117772.0	0.05	58.84	33.44	6.44	1.23
2020	44.55	73882.99	33256.41	10105.78	482.27	117772.0	0.04	62.73	28.24	8.58	0.41
2021	24.73	75769.5	28406.45	12896.21	675.11	117772.0	0.02	64.34	24.12	10.95	0.57

Appendix B.2 TCI Drought Areas and Percentages (2000-2021)

Year	TCI Extreme Drought	TCI Mild Drought	TCI Moderate Drought	TCI No Drought	TCI Severe Drought	Total Area	TCI Extreme Drought %	TCI Mild Drought %	TCI Moderate Drought %	TCI No Drought %	TCI Severe Drought %
2000	2.05	52614.43	62083.72	1843.76	1228.04	117772.0	0.0	44.67	52.71	1.57	1.04
2001	1.44	71714.74	42382.4	3275.25	398.18	117772.0	0.0	60.89	35.99	2.78	0.34
2002	0.83	76890.87	31572.14	9034.7	273.46	117772.0	0.0	65.29	26.81	7.67	0.23
2003	1.35	78597.98	32982.61	5208.44	981.63	117772.0	0.0	66.74	28.01	4.42	0.83

2004	4.93	56483.99	57688.64	2750.78	843.67	117772.0	0.0	47.96	48.98	2.34	0.72
2005	3.28	87295.26	25747.52	3994.9	731.05	117772.0	0.0	74.12	21.86	3.39	0.62
2006	9.66	72716.18	40367.66	3276.05	1402.46	117772.0	0.01	61.74	34.28	2.78	1.19
2007	3.74	76869.44	33522.6	6445.53	930.7	117772.0	0.0	65.27	28.46	5.47	0.79
2008	3.33	92695.23	20355.09	4469.86	248.5	117772.0	0.0	78.71	17.28	3.8	0.21
2009	4.21	75908.21	35378.59	5835.78	645.23	117772.0	0.0	64.45	30.04	4.96	0.55
2010	2.3	73526.0	35042.78	8343.13	857.8	117772.0	0.0	62.43	29.75	7.08	0.73
2011	1.38	79297.57	33152.84	4803.87	516.35	117772.0	0.0	67.33	28.15	4.08	0.44
2012	5.89	98830.54	14145.55	4588.38	201.65	117772.0	0.01	83.92	12.01	3.9	0.17
2013	3.52	79678.71	33241.93	3877.51	970.33	117772.0	0.0	67.65	28.23	3.29	0.82
2014	0	75571.7	25340.69	16342.77	517.15	117772.0	0.0	64.17	21.52	13.88	0.44
2015	2.51	58554.53	54963.9	2569.16	1681.91	117772.0	0.0	49.72	46.67	2.18	1.43
2016	19.92	67491.75	47018.72	1600.32	1641.31	117772.0	0.02	57.31	39.92	1.36	1.39
2017	5.1	60982.52	52706.31	2159.09	1918.98	117772.0	0.0	51.78	44.75	1.83	1.63
2018	1.68	80953.28	33580.79	2465.69	770.57	117772.0	0.0	68.74	28.51	2.09	0.65
2019	14.15	58329.08	54020.2	3254.92	2153.66	117772.0	0.01	49.53	45.87	2.76	1.83
2020	5.96	73430.81	39825.05	3207.69	1302.49	117772.0	0.01	62.35	33.82	2.72	1.11
2021	3.34	66138.35	47004.33	2884.22	1741.78	117772.0	0.0	56.16	39.91	2.45	1.48

Appendix B.3 VHI Drought Areas and Percentages (2000-2021)

Year	VHI Extreme Drought	VHI Mild Drought	VHI Moderate Drought	VHI No Drought	VHI Severe Drought	Total Area	VHI Extreme Drought %	VHI Severe Drought %	VHI Moderate Drought %	VHI Mild Drought %	VHI No Drought %

2000	2.22	62071.59	52330.68	3279.54	87.99	117772.0	0.0	0.07	44.43	52.7	2.78
2001	7.62	89597.75	21032.21	7069.18	65.22	117772.0	0.0	0.05	17.86	76.08	6.0
2002	1.74	82850.78	20990.32	13922.32	6.82	117772.0	0.0	0.01	17.82	70.35	11.82
2003	1.05	71191.75	45501.57	853.63	224.02	117772.0	0.0	0.19	38.64	60.45	0.72
2004	0.46	66553.25	47667.62	3509.74	40.94	117772.0	0.0	0.03	40.47	56.51	2.98
2005	1.31	84737.43	30208.45	2736.68	88.11	117772.0	0.0	0.07	25.65	71.95	2.32
2006	1.93	83109.28	30533.01	4000.49	127.31	117772.0	0.0	0.11	25.93	70.57	3.4
2007	5.78	80063.2	34405.63	3054.48	242.92	117772.0	0.0	0.21	29.21	67.98	2.59
2008	2.58	70822.8	43447.7	3410.3	88.63	117772.0	0.0	0.08	36.89	60.14	2.9
2009	2.85	47742.76	69181.58	405.13	439.7	117772.0	0.0	0.37	58.74	40.54	0.34
2010	6.81	87962.87	19464.8	10265.7	71.82	117772.0	0.01	0.06	16.53	74.69	8.72
2011	0.12	96236.41	13431.5	8095.23	8.73	117772.0	0.0	0.01	11.4	81.71	6.87
2012	0.16	77836.74	39161.01	746.48	27.63	117772.0	0.0	0.02	33.25	66.09	0.63
2013	1.32	86925.97	27027.58	3775.85	41.28	117772.0	0.0	0.04	22.95	73.81	3.21
2014	1.96	88510.99	22207.49	6915.37	136.17	117772.0	0.0	0.12	18.86	75.15	5.87
2015	0.89	63129.9	53054.72	1481.03	105.46	117772.0	0.0	0.09	45.05	53.6	1.26

2016	4.28	61352.66	54942.92	1294.13	178.0	117772.0	0.0	0.15	46.65	52.09	1.1
2017	20.34	40776.45	74497.98	453.75	2023.49	117772.0	0.02	1.72	63.26	34.62	0.38
2018	14.18	65987.03	50897.13	646.21	227.44	117772.0	0.01	0.19	43.22	56.03	0.55
2019	4.87	73796.71	38244.5	5551.94	173.96	117772.0	0.0	0.15	32.47	62.66	4.71
2020	11.61	84079.72	29373.45	4239.82	67.38	117772.0	0.01	0.06	24.94	71.39	3.6
2021	7.43	78213.14	30527.44	8918.7	105.27	117772.0	0.0	0.09	25.92	66.41	7.57

Appendix B.4 Code Used to calculate Pearson Correlation

```
# Load necessary libraries
library(dplyr)
library(ggplot2)
library(reshape2)

# Sample data import ("replace with actual file paths")
spi_data <- read.csv("path/to/spi_data.csv")
vci_data <- read.csv("path/to/vci_data.csv")
tci_data <- read.csv("path/to/tci_data.csv")
vhi_data <- read.csv("path/to/vhi_data.csv")

# Ensure data frames have common columns for merging, such as Date and Station ID
merged_data <- spi_data %>%
  inner_join(vci_data, by = c("Date", "Station_ID")) %>%
  inner_join(tci_data, by = c("Date", "Station_ID")) %>%
  inner_join(vhi_data, by = c("Date", "Station_ID"))

# Calculate Pearson correlation for each station
```

```
stations <- unique(merged_data$Station_ID)
correlation_results <- data.frame(Station_ID = character(), VCI_SPI = numeric(),
TCI_SPI = numeric(), VHI_SPI = numeric(), stringsAsFactors = FALSE)

for (station in stations) {
  station_data <- merged_data %>% filter(Station_ID == station)
    vci_spi_cor <- cor(station_data$SPI, station_data$VCI, method = "pearson")
  tci_spi_cor <- cor(station_data$SPI, station_data$TCI, method = "pearson")
  vhi_spi_cor <- cor(station_data$SPI, station_data$VHI, method = "pearson")
    correlation_results <- rbind(correlation_results, data.frame(Station_ID = station,
VCI_SPI = vci_spi_cor, TCI_SPI = tci_spi_cor, VHI_SPI = vhi_spi_cor))
}
# Print correlation results
print(correlation_results)

# Save results to a CSV file
write.csv(correlation_results, "correlation_results.csv", row.names = FALSE)

# Plot heatmap of the correlation results
correlation_melted <- melt(correlation_results, id.vars = "Station_ID")
ggplot(correlation_melted, aes(x = Station_ID, y = variable, fill = value)) +
  geom_tile() +
  scale_fill_gradient2(low = "blue", mid = "white", high = "red", midpoint = 0, limits =
c(-1, 1)) +
  theme_minimal() +
  theme(axis.text.x = element_text(angle = 90, hjust = 1)) +
  labs(title = "Pearson Correlation Between SPI and VCI, TCI, VHI", x = "Station ID", y
= "Index", fill = "Correlation")
plot_heatmap(data, "TCI Correlation", "Pearson Correlation Matrix for TCI across
Stations")
# Plotting VHI Correlation Heatmap
plot_heatmap(data, "VHI Correlation", "Pearson Correlation Matrix for VHI across
Stations")
```